PDR

NUREG/CR-2111

Bubble Behavior in LMFBR Core Disruptive Accidents

Annual Report
October 1979 - September 1980

Prepared by A. B. Reynolds, C. A. Erdman, R. C. Anderson, D. R. Bradley, K. Chen, M. R. Gold, R. R. Humphris, M. Pilch

Department of Nuclear Engineering and Engineering Physics
University of Virginia

Prepared for
U.S. Nuclear Regulatory
Commission

Available from

GPO Sales Program
Division of Technical Information and Document Control
U. S. Nuclear Regulatory Commission
Washington, D. C. 20555

Printed copy price: $5.50

and

National Technical Information Service
Springfield, Virginia 22161

NUREG/CR-2111
R7

Bubble Behavior in LMFBR Core Disruptive Accidents

Annual Report
October 1979 - September 1980

Manuscript Completed: December 1980
Date Published: July 1981

Prepared by
A. B. Reynolds, C. A. Erdman, R.C. Anderson, D. R. Bradley,
K. Chen, M. R. Gold, R.R. Humphris, M. Pilch

Department of Nuclear Engineering and Engineering Physics
University of Virginia
Charlottesville, VA 22901

Prepared for
Division of Accident Evaluation
Office of Nuclear Regulatory Research
U.S. Nuclear Regulatory Commission
Washington, D.C. 20555
NRC FIN B5616

ABSTRACT

Research performed at the University of Virginia during FY 80 for the Advanced Reactor Safety Research Division of the U.S. Nuclear Regulatory Commission is reported. The research is part of the Aerosol Release and Transport Program. Four principal areas were investigated: (1) bubble dynamics and heat transfer, (2) measurement of particle sizes and flashing, (3) acceleration-induced fragmentation of liquid drops, and (4) particle-size distributions from condensation. In the first area, the UVABUBL computer model for the analysis of bubble expansion in ORNL FAST tests is described. In the second, development of an experiment to flash high temperature water and measure droplet sizes from flashing is described. In the third area, results of an extensive literature analysis of acceleration-induced fragmentation of liquid drops, together with model improvements over the entire range from bag to catastrophic breakup, are summarized. In the last area, computer analysis of the measured particle-size distributions from ORNL CDV tests in argon indicates that the particles were formed by homogeneous nucleation and condensation growth.

EXECUTIVE SUMMARY

Bubble Dynamics and Heat Transfer

Analysis of the ORNL FAST tests under water was continued. A computer code, UVABUBL, was developed to analyze bubble motion following capacitor discharge to UO_2 pellets under water and sodium in the FAST facility.

An early version of the code showed a strong sensitivity to the radiation emissivity of the two-phase UO_2 bubble. While the measured magnitude of the pressure response could be reproduced with the UVABUBL model, the calculated period of the bubble oscillation was too small and the calculated radius was too large. Several modifications of the code are being made to try to explain the differences in period and radius. It appears that vaporization of water by the UO_2 and subsequent condensation of the water vapor are playing a major role in the behavior of the bubble.

Sodium properties were developed in a form suitable for use in the UVABUBL code, and analysis of FAST tests under sodium was initiated.

Measurement of Particle Sizes from Flashing

Flashing, i.e. rapid boiling due to sudden depressurization that produces a superheated liquid, produces small liquid droplets which can influence both aerosol transport and subsequent heat transfer in an HCDA. Significant progress was made on the development of an experiment to measure the primary particle size distribution from flashing. A system for flashing superheated water to the atmosphere was assembled, and pressure integrity of the system under experiment conditions was established. Study of flashing of low superheat was initiated.

Six flashing tests have been run, with depressurization from ~0.9 MPa to atmospheric pressure occuring in ~0.5 ms. Movies at ~5000 frames per second are being taken to observe the flashing process.

Development of the method for opening the door to the flashing chamber was completed. To accomplish rapid opening of the door, a falling lever arm couples to the door via a steel cable. This produces door opening times as low as 1.64 milliseconds.

Feasibility of the method for measuring particle size distributions was demonstrated. Water solutions containing $CoCl_2 \cdot 6\ H_2O$ in solution were sprayed onto white blotter paper, producing blue spots found to be proportional in diameter to the two-thirds power of original drop diameter. The quantity of $CoCl_2$ in each spot, and hence original drop size, was determined by neutron activation analysis. Preliminary investigations with droplets produced by atomizers indicate that it may be possible to determine initial drop size as small as 1 μm diameter.

Acceleration-Induced Fragmentation of Liquid Drops

A critical study of the literature on acceleration-induced fragmentation was concluded, and several new models were developed. A detailed plot of droplet breakup time versus Weber number was developed. Liquid liquid data were shown to be consistent with gas-liquid data. Available fragmentation size data were summarized.

A detailed bag breakup model was reported in the previous annual report.

Examination of models reported in the literature for sheet stripping and catastrophic breakup modes showed these models to be inadequate, especially the classic boundary layer stipping and Rayleigh-Taylor models. It was shown, however, that Rayleigh-Taylor instabilities do play a major role in all modes of breakup, from bag and bag-and-stamen breakup (low Weber

number range) to stripping and catastrophic breakup (high Weber range). A two-stage model was developed to illustrate how Rayleigh-Taylor instabilities affect catastrophic breakup--a linear, small amplitude stage followed by a nonlinear, constant-penetration velocity stage.

Finally, the distribution of drop diameters from breakup was considered. Fragments can acquire Weber numbers less than the "critical" Weber number by two processes: breakup and drop acceleration. The conventional maximum stable diameter calculation neglects drop acceleration effects; inclusion of these effects can explain why final drop sizes much larger than those predicted by the conventional calculation are observed experimentally.

Particle-Size Distribution from Condensation in the ORNL CDV Tests in Argon

Analysis of particle-size distributions for the ORNL FAST tests in argon was completed. Particle-size distributions were calculated with the computer code CIVE which match closely the measured particle-size distributions, except possibly for the largest particles observed. Both calculated and measured particle-size distributions were close to log normal.

In the computer model, it was assumed that condensation was produced by homogeneous nucleation in an expanding sphere of UO_2 vapor, followed by condensation growth of the droplets. The expansion hydrodynamics was analyzed by a spherical shock-tube type model; the supersaturation required for nucleation was caused by a rarefaction wave propagating through the expanding UO_2 vapor. The expansion was calculated by means of the WONDY computer code, developed by Sandia National Laboratories.

The close agreement between theory and experiment tends to confirm the hypothesis that the very small particles (in the 0.003 μm to 0.1 μm range) result from homogeneous nucleation in the expanding rarefaction wave of the UO_2 vapor followed by condensation growth on the droplets.

TABLE OF CONTENTS

LIST OF FIGURES

LIST OF FIGURES (Continued)

LIST OF FIGURES (Continued)

LIST OF TABLES

I. INTRODUCTION

The University of Virginia is a particpant in the Aerosol Release and Transport Program of the Reactor Safety Research Division of the U. S. Nuclear Regulatory Commission. Work performed in FY 80 is reported here. Work completed prior to FY 80 was described in previous annual reports[1-3] and associated papers[4-15]. References 16-18 cover work performed during FY 80.

Major areas of investigation this past year were the following:

- Bubble dynamics and heat transfer
- Measurement of particle sizes from flashing
- Acceleration-induced fragmentation of liquid drops
- Particle-size distributions from condensation in the ORNL CDV tests in argon.

In addition a review paper on the source term in LMFBR core disruptive accidents was prepared by A. B. Reynolds, together with T. R. Kress of ORNL, for presentation at the CSNI Specialists Meeting on Nuclear Aerosols in Reactor Safety.

The first of the four major areas of investigation is described in Section 2. Analysis of bubble expansion in the ORNL CDV tests is continuing with the use of UVABUBL code. The computer model and current results are described in this report.

In Section 3 is described an experiment underway to measure droplet sizes from flashing. High temperature saturated water is suddenly exposed to the atmosphere. The apparatus has been developed and preliminary tests have been run. Methods for droplet collection and for droplet diameter measurement by a neutron activation technique are still being developed.

An extensive study of models reported in the literature for acceleration-induced fragmentation of liquid drops was concluded, and some of the important results are summarized in Section 4. Deficiencies in reported models are noted and improvements developed in the present investigation are described. A particularly useful result is a new consistent graph of droplet breakup time as a function of Weber number which includes most of the reported experimental data.

The final section describes a calculation of the particle-size distribution measured in the ORNL CDV tests in argon. Calculated results are in substantial agreement with the experimental data, which tends to confirm the hypothesis that the small particles result from homogeneous nucleation followed by condensation growth. The model represents a significant improvement beyond the earlier model developed by Kennedy, et. al., in this same project.

REFERENCES--Work Performed under this Program

1. A. B. Reynolds, C. A. Erdman, P. L. Garner, M. F. Kennedy, S. P. Rao, and J. G. Refling, "Bubble Behavior in LMFBR Core Disruptive Accidents, Annual Report, June 1, 1975 - June 30, 1976," NUREG-0114, University of Virginia for USNRC (September 1976).*

2. C. A. Erdman, A. B. Reynolds, A. E. Walter, P. L. Garner, M. F. Kennedy, and M. Pilch, " Bubble Behavior in LMFBR Core Disruptive Accidents, Annual Report, July 1, 1976 - September 30, 1977," NUREG/CR-0002, University of Virginia for USNRC (February 1978).*

3. C. A. Erdman, A. B. Reynolds, D. R. Bradley, K. Chen, and M. Pilch, "Bubble Behavior in LMFBR Core Disruptive Accidents, Annual Report October 1977 - September 1978," NUREG/CR-0604, University of Virginia for USNRC (March 1979).**

4. A. B. Reynolds, C. A. Erdman, M. Kirbiyik, "Fuel Vapor Generation in LMFBR Core Disruptive Accidents," Nuclear Technology, Vol. 26 (June 1975), pp. 165-71.

5. A. B. Reynolds and S. P. Rao, "Analytical and Planning Assistnace for ORNL Bubble-Behavior Experiments," ORNL-SUB-3980-1, University of Virginia for ORNL (August 1975).

6. M. Kirbiyik, P. L. Garner, J. G. Refling, and A. B. Reynolds, "Hydrodynamics of Post-Disassembly Fuel Expansion," Nucl. Eng. and Des., Vol 35, (December 1975), pp. 441-60.

7. J. G. Refling, R. P. Garner, S. P. Rao, and A. B. Reynolds, "Nonequilibrium Evaporation and Condensation in LMFBR Fuel Expansion Tests," Trans. ANS, Vol. 23 (1976), p. 373.

8. P. L. Garner and C. A. Erdman, " Condensation of Flowing UO_2 Fuel Vapor Onto a Vertical Steel Substrate, " Trans. ANS, Vol. 24 (November 1976), p. 263.

9. J. G. Refling, A. B. Reynolds, P. L. Garner, and S. P. Rao, "Nonequilibrium Evaporation and Condensation in Liquid Metal Fast Breeder Reactor Fuel Expansion," Nuclear Technology, Vol. 33, (May 1977), pp. 275-89.

10. M. F. Kennedy, C. A. Erdman, P. L. Garner, A. B. Reynolds, and A. E. Walter, "A First-Generation Model to Predict Particle-Size Distributions for Condensed UO_2 Vapor," Trans. ANS, Vol. 26 (June 1977), p. 339.

11. P. L. Garner and C. A. Erdman, "The Importance of the Solidification of Fuel Condensate," Trans. ANS, Vol. 26 (June 1977), p. 373.

12. P. L. Garner, "Condensation of Fuel Onto the Above-Core Structure During an LMFBR Core-Disruptive Accident," NUREG-0344, University of Virginia for USNRC (October 1977).*

13. M. F. Kennedy, "Primary Aerosol Particle-Size Distribution from Homogeneous Nuceation Condensation and Particle Growth," NUREG-0391, University of Virginia for USNRC (December 1977).*

14. M. Pilch and C. A. Erdman, "Particle-Size Distributions from Multiple Hydrodynamic Fragmentation Events," Proceedings of the ANS/ENS International Meeting on Fast Reactor Safety Technology, Vol. 1, 239-248 (Seattle, WA; August 1979).

15. A. B. Reynolds and D. R. Bradley, "Axial Motion of Large Two-Phase Bubbles," Proceedings of the ANS/ENS International Meeting on Fast Reactor Safety Technology, Vol. IV, 1838-1847 (Seattle, WA; August 1979).

16. A. B. Reynolds and T. S. Kress, "Aerosol Source Considerations for LMFBR Core Disruptive Accidents," Proceedings of the CSNI Specialists Meeting on Nuclear Aerosols in Reactor Safety, NUREG/CR-1724, ORNL/NUREG/TM-404,CSNI-45, 1-23 (Gatlinburg, TN; April 1980).**

17. K. Chen and A. B. Reynolds, "Particle-Size Distribution from Condensation in ORNL CDV Tests in Argon," NUREG report, to be issued, University of Virginia.

18. M. Pilch and C. A. Erdman, "Accelertion-Induced Fragmentation of Liquid Drops," NUREG report, to be issued, University of Virginia.

*Available for purchase from the National Technical Information Service, Springfield, VA 22161.

**Available for purchase from the NRC/GPO Sales Program, U.S. Nuclear Regulatory Commission, Washington, DC 20555 and/or the National Technical Information Service, Springfield, VA 22161.

2. BUBBLE DYNAMICS AND HEAT TRANSFER

D. R. Bradley, M. R. Gold, and A. B. Reynolds

2.1 Introduction

In the Fuel Aerosol Simulant Test (FAST) experiments being conducted at Oak Ridge National Laboratory (ORNL), two-phase uranium dioxide bubbles are created using the Capacitor Discharge Vaporization (CDV) technique. After capacitor discharge the test assembly enclosing the UO_2 fuel pellets shatters, releasing the hot (>5000 K) two-phase bubble into a partially filled tank of water. By examining the subsequent expansion and collapse of the bubble some insight can be gained into the heat and mass transfer processes occurring as well as fuel aerosol transport during a Hypothetical Core Disruptive Accident in a liquid metal fast breeder reactor. The work presented in this section represents the first attempts at modelling the ORNL experiments and resulted in the development of the UVABUBL computer code.

The experimental data used for comparison in this report was reported previously in Reference 1. The UVABUBL results quoted here are being presented for the first time.

For more information regarding the CDV technique and the FAST tests see references 2, 3.

2.2 Model for Analysis of ORNL FAST Underwater Experiments

In the FAST experiments, a multicomponent mixture of two-phase fuel, coolant, and inert gas expands against a column of water while simultaneously exchanging heat, mass, and momentum with the surroundings. These experiments are more difficult to analyze than earlier experiments

which involved either a single component bubble expansion or a low temperature expansion in which heat and/or mass transfer were negligible. The complexity of the problem will be evident in the following discussion.

2.2.1 Momentum Transfer - Equations of Motion

A discussion of the equations for radial and axial motion was reported earlier[4] and will only be summarized here.

The driving force for the initial radial expansion is the pressure difference, $P_B - P'$, between the internal bubble pressure and the pressure in the surrounding water. During the expansion, momentum is transferred to the surroundings such that the inertia of the water forces the bubble to expand even though the internal pressure drops to less than the ambient. Soon, however, the outward motion stops and the bubble begins to collapse, again being driven by the pressure difference, $P_B - P'$, which in this instance is negative.

The equation governing radial motion is an inertial constraint equation - the Rayleigh equation:

$$\ddot{R} = \frac{P_B - P'}{\rho R} - \frac{3}{2}\frac{\dot{R}^2}{R} \qquad (2\text{-}1)$$

where ρ is the density of the surrounding coolant; P' is the cover gas pressure; P_B is the internal bubble pressure and $\ddot{R}$ and $\dot{R}$ are the radial acceleration and velocity of a bubble of radius R.

Bradley and Reynolds[4] extended Eq. (2-1) to include axial forces and also derived equations for axial motion. Since these effects were not included in the present analysis they will not be reported here.

A general form of Eq. (2-1) can be written for the pressure at any radial location outside of the bubble:

$$P(r) = \rho \left(\frac{R}{r}\right) \left(R\ddot{R} + 2\dot{R}^2\right) + P' \qquad (2\text{-}2)$$

This equation is used when calculating the transducer pressure which can then be compared to the experimental results.

2.2.2 Calculation of Bubble Temperature

In order to determine the bubble pressure, P_B, the bubble temperature, T_B, had to be calculated. Using the First Law of Thermodynamics to relate the internal state of the bubble to the energy exchange processes at its surface, an equation for dT_B/dt was derived.

The form of the First Law applicable to our problem:

$$\frac{dU_T}{dt} = - P_B \frac{dV}{dt} - Q + \dot{m}_c h_{gc} + \dot{m}_f h_f \qquad (2\text{-}3)$$

where Q is the total heat loss from the bubble, $\dot{m}_c$ and $\dot{m}_f$ are mass blow rates of coolant and fuel, and h_{gc} and h_f are the enthalpies of the entering material. The total internal energy, U_T, can be written:

$$U_T = m_f \left(u_{\ell f} + x_f u_{\ell gf}\right) + m_c u_c$$

Following a procedure similar to that found in Ref. 5, the equation for dT_B/dt was derived:

$$\frac{dT_B}{dt} = \frac{- \frac{dV}{dt} \left(\frac{h_{\ell gf}}{v_{\ell gf}} + \frac{R_c T_B}{v_c - b} + P_{gas}\right) - Q + \dot{m}_c u_c^* + \dot{m}_f h_f^*}{m_f \left[\frac{dh_{\ell f}}{dT} + x_f \frac{dh_{\ell gf}}{dT} - \frac{h_{\ell gf}}{v_{\ell gf}} \left(\frac{dv_{\ell f}}{dT} + x_f \frac{dv_{\ell gf}}{dT}\right) - v_f \left(\frac{dP_f}{dT}\right)\right] + m_c c_{vc}} \qquad (2\text{-}4)$$

where $u_c^* = u_{gc} - u_c + a/v_c$ and $h_f^* = h_f - u_{\ell f} + x_f\, u_{\ell gf} + u_{\ell gf}\, v_f/v_{\ell gf}$. Note that the coolant is assumed to be adequately represented by the van der Waals equation of state.

The underlying assumption for this analysis is that the bubble is in thermodynamic equilibrium; that is, there are no temperature or pressure gradients within the bubble, and the fuel liquid and vapor phases can be considered as a homogeneous mixture.

As the bubble expands and heat is transferred, T_B drops rapidly. When the temperature drops to UO_2 liquidus, the liquid fuel in the two-phase mixture begins to solidify and all three phases are present. Thermodynamically, the UO_2 is said to be at the triple state.

The expansion is shown schematically in the p-v diagram of Fig. 2.1. When the triple state line is reached at point 1, the vapor quality is non-zero. As the bubble continues to expand the UO_2 moves along the path between 1 and 2. The temperature cannot decrease further until all of the liquid UO_2 has either solidified or vaporized. When this takes place the state of the UO_2 can move from point 2 into the solid + gas region.

As long as the UO_2 exists at the triple state, its state is completely determined by two properties: the vapor quality, x_f, and the solid mass fraction, y_f. For example, $u_f = u_{\ell f} + x_f\, u_{\ell gf} - y_f\, u_{\ell sf}$.

As above the First Law gives:

$$\frac{dy_f}{dt} = \frac{1}{m_f} \cdot \frac{-\frac{dV}{dt}\left(\frac{h_{\ell gf}}{v_{\ell gf}} + \frac{R_c T}{v_c - b} + P_{gas}\right) - Q + \dot{m}_c\, u_c + \dot{m}_f\, h_f^*}{\frac{1}{v_{\ell gf}}\left(u_{\ell gf}\, v_{\ell gf} - u_{\ell sf}\, v_{\ell gf}\right)} \qquad (2\text{-}5)$$

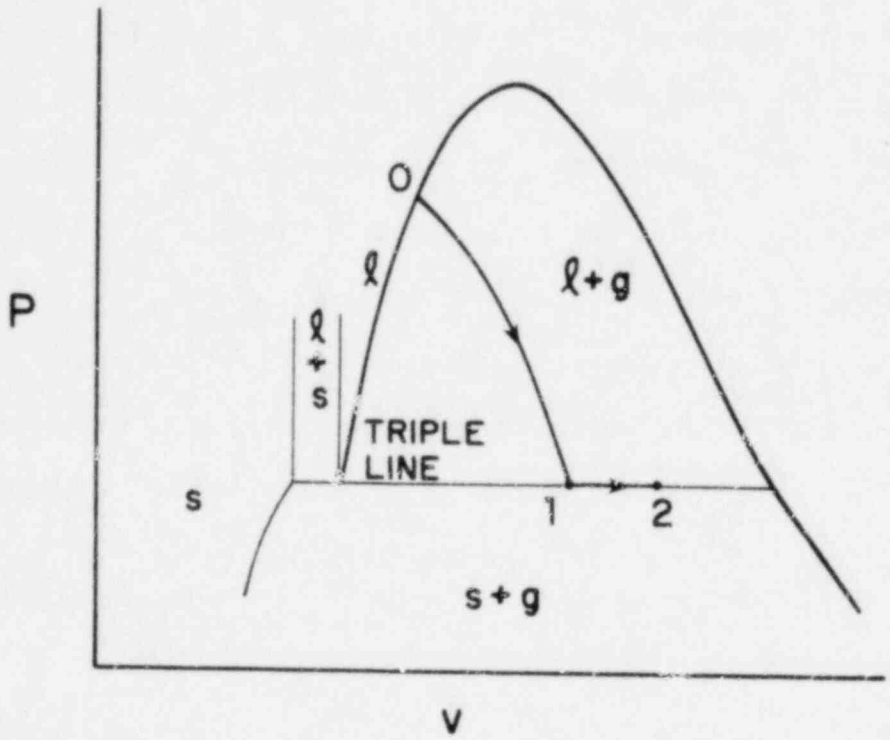

Figure 2.1. Schematic of UO_2 expansion path (0 to 1 to 2) on a fuel P-v diagram, showing the change in path along the triple line.

where h_f^* is now equal to $h_f - u_{\ell f} - x_f u_{\ell g f} + y_f u_{\ell s f}$ and the other terms have the same meaning as in Eq. 2-4.

The above model applies as long as there is liquid at the triple state or until the bubble contracts and reenters the liquid-vapor dome. When the liquid is gone, $x_f + y_f = 1$; and further expansion of the bubble will continue into the solid-vapor region. The equation for T_B during this process is identical to Eq. (2-4) with the s subscript replacing all ℓ subscripts.

The next step in the analysis is the evaluation of the heat and mass transfer mechanisms involved in Q, $\dot{m}_c$, and $\dot{m}_f$.

2.2.3 Heat and Mass Transfer at Surface

Because the contents of the bubble are so hot, radiation heat transfer is the dominant mode of heat loss from the bubble. This heat is radiated to the bubble interface at a rate determined by the following equation:

$$Q_{r,s} = \left(\frac{\varepsilon_s \varepsilon_g}{\varepsilon_s + \varepsilon_g - \varepsilon_s \varepsilon_g}\right) \sigma A_s (T_B^4 - T_s^4) \qquad (2\text{-}6)$$

where ε_s and ε_g are emissivities of the interface and bubble vapor, A_s is bubble surface area, and T_s is the interface temperature.

Though the formulation given by Eq. (2-6) is very simple, there is a hidden pitfall which makes the solution of the radiation heat transfer problem very difficult. The bubble vapor emissivity, ε_g, is a function of total pressure, partial pressures of each component, and bubble size. General trends for these relationships can be extrapolated from the data for other vapors but the magnitude of ε_g for UO_2 is unknown. The vapor emissivity for the multicomponent mixture will therefore be treated as a parameter in the UVABUBL model. The sensitivity of the analysis to ε_g

will be demonstrated in a later section.

The heat radiated to the bubble surface is conducted into the coolant. However, due to the temporal dependence of the bubble temperature, radius, and surface temperature, an exact solution to the conduction equation would require solving a complicated integral equation. If, however, a quadratic temperature profile is assumed in the coolant surrounding the bubble, the problem becomes one of solving two differential equations (which is compatible with solution procedure already outlined).

The form of the temperature is found by applying the following boundary conditions: a) $T(R,t) = T_s$; b) $T(R_1,t) = T_\infty$; c) $\frac{\partial T}{\partial r}(R_1,t) = 0$. The result is:

$$T(r,t) = T_\infty + (T_s - T_\infty)\frac{(R_1 - r)^2}{(R_1 - R)^2} \qquad (2\text{-}7)$$

where R_1 is the radial distance to the outside of the thermal boundary layer (i.e., $R_1 - R = \delta$) and T_∞ is the ambient temperature.

Following a procedure similar to that of Fauske, et. al.,[6] two differential equations for the unknowns, $T_s(t)$ and $R_1(t)$ are derived. These derivations are summarized below. For a graphical representation of the surface heat transfer problem refer to Fig. 2.2.

The energy balance in a volume element within the boundary layer is given by:

$$\rho c_p \left(\frac{\partial T}{\partial t} + u_r \frac{\partial T}{\partial r}\right) = k \frac{1}{r^2}\frac{\partial}{\partial r}\left(r^2 \frac{\partial T}{\partial r}\right) \qquad (2\text{-}8)$$

where k is the thermal conductivity of the coolant and u_r is the velocity component of the coolant in the radial direction. From the

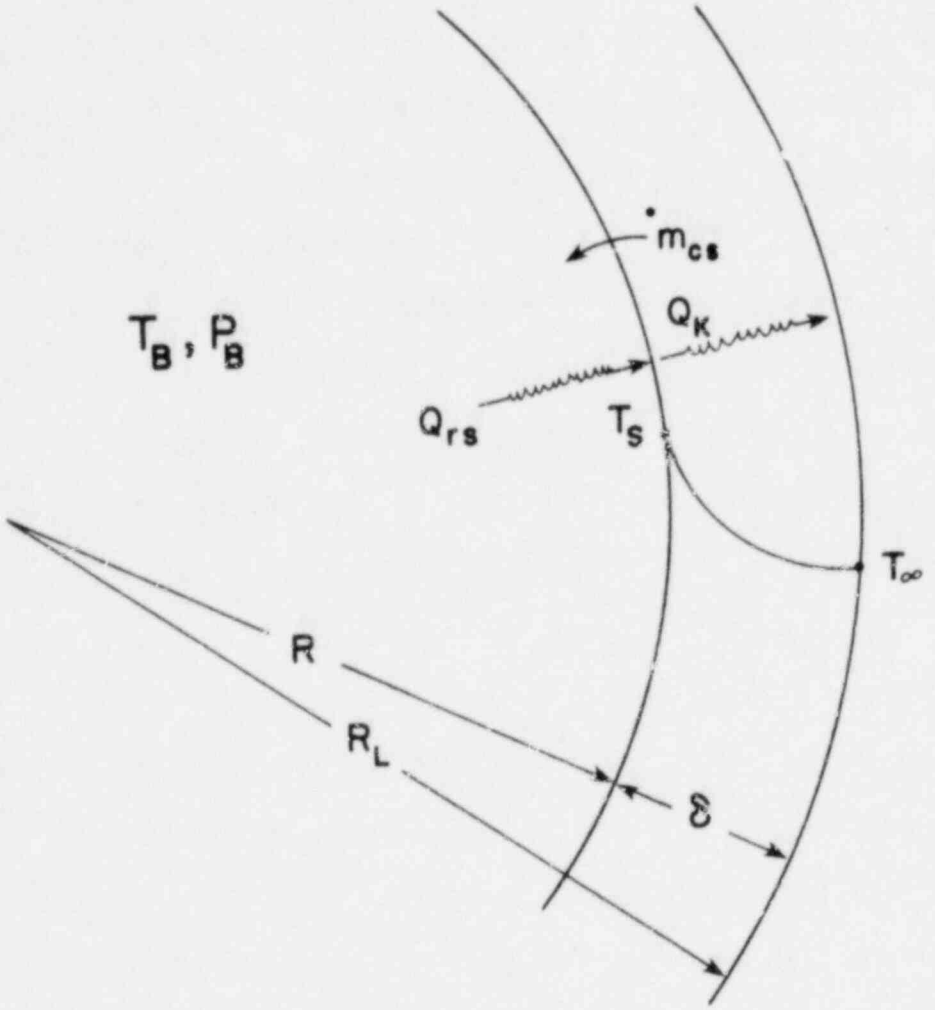

Figure 2.2. Schematic of surface heat transfer problem.

continuity equation, u_r is defined:

$$u_r = \dot{R} \left(\frac{R}{r}\right)^2 - \frac{\dot{m}_{cs}}{4\pi\rho r^2} \tag{2-9}$$

where $\dot{m}_{cs}$ is the rate of evaporation of coolant at the surface.

Substituting Eqs. (2-7) and (2-9) into (2-8) and integrating the result over the volume of the boundary layer, the following equation for dR_1/dt is derived:

$$\frac{dR_1}{dt} = - \frac{\frac{dT_s}{dt}\delta(R_1^2 + 3R_1R + 6R^2) - \dot{R}\theta(2R_1^2 + 6R_1R - 18R^2) + 60\frac{\alpha\theta}{\delta}R^2 - \frac{30\theta\dot{m}_{cs}}{4\pi\rho}}{\theta(3R_1^2 + 4R_1R + 3R^2)} \tag{2-10}$$

where α is the coolant thermal diffusivity, θ is the temperature difference across the boundary layer, $T_s - T_\infty$, and δ is the thermal boundary layer thickness.

The heat flux balance at the surface is given by:

$$\varepsilon_T\sigma (T_B^4 - T_s^4) = -k \left.\frac{\partial T}{\partial r}\right|_{r=R} \tag{2-11}$$

where ε_T is the effective total emissivity shown in Eq. (2-6). After substituting for the derivative and then differentiating both sides with respect to time, the following equation for dT_s/dt is derived:

$$\frac{dT_s}{dt} = \frac{1}{4\varepsilon\sigma T_s^3 + \frac{2k}{\delta}} \left[\frac{2k\theta}{\delta^2}\left(\frac{dR_1}{dt} - \frac{dR}{dt}\right) + 4\varepsilon\sigma T_B^3 \frac{dT_B}{dt}\right] \tag{2-12}$$

Note that in the energy balance, (2-11), the contribution of evaporating coolant was excluded. The reason for this will become evident shortly.

In order to avoid computational difficulties, the boundary layer thickness is assumed to be non-zero at the start of the conduction cal-

culation. In the present version of UVABUBL the value chosen for δ is consistent with an initial surface temperature 1 K higher than ambient. Therefore,

$$\delta\ (t=0) = 2k/\varepsilon_T\sigma\ (T_B^4 - T_s^4) \qquad (2\text{-}13)$$

As the heat transfer calculation continues both the surface temperature and boundary layer thickness increase. The magnitude of T_s, however, is limited by the saturation temperature of the coolant at the bubble pressure. When this temperature is reached, vaporization of coolant at the surface occurs and T_s is no longer defined by (2-12). The appropriate equation is:

$$\frac{dT_s}{dt} = \frac{dT_s}{(\quad)} = \frac{dT_{sat}}{dP_B} \cdot \frac{dP_B}{dt} \qquad (2\text{-}14)$$

One should note that in the previous analysis (2-12) gives the upper limit on dT_s/dt since it leads to a maximum possible value for conduction heat transfer. If (2-14) gives a value which exceeds $(dT_s/dt)max$, the radiation heat transfer to the surface cannot sustain the saturated state, coolant vaporization ceases and T_s drops below T_{sat}. This check must be made for each time step in which surface vaporization takes place.

The coolant vaporization rate, $\dot{m}_{cs}$, is given by:

$$\dot{m}_{cs} = (Q_{rs} - Q_k)/h_{\ell gc} \qquad (2\text{-}15)$$

where Q_{rs} and Q_k are the radiation and conduction heat transfer rates and $h_{\ell gc}$ is the heat of vaporization for the coolant.

2.2.4 Heat and Mass Transfer from Entrained Drops

In the early stages of the bubble expansion the formation of Taylor instabilities has been observed. As classical theory predicts[7],

the instabilities appear to grow rapidly during the first few tenths of a millisecond and then as the radial acceleration becomes negative, the growth phase ends and the bubble surface eventually becomes smooth.

Corradini, et. al.[8] have shown that during the growth phase, the denser material (coolant) is entrained by the less dense material (bubble vapor). The rate of entrainment, according to their analysis, is given by the following expression:

$$\dot{m}_e = K_1 \rho A_s \left(\ddot{R}\lambda_c\right)^{1/2} \tag{2-16}$$

where K_1 is the proportionality constant for entrainment and λ_c is the critical wavelength for Taylor instability formation. The critical wavelength is given by:

$$\lambda_c = 2\pi \left(\frac{\sigma_{st}}{\ddot{R}\,(\rho-\rho_v)}\right)^{1/2} \tag{2-17}$$

where σ_{st} is the surface tension and ρ_v is the density of the bubble vapor.

In the experiments at MIT, Corradini found K_1 to be 4.65; their experiments were, however, very different from the FAST tests. The MIT experiments examined a one-dimensional expansion with little or no heat transfer and phase change at the liquid-vapor interface. Hsieh[9] has proposed that heat and mass transfer at the interface may have a significant effect on Taylor instability formation and growth. The entrainment constant will, therefore, be treated as a parameter in the UVABUBL model.

The droplets enter at the temperature of the surrounding coolant, T_∞, and are heated to the saturation temperature by radiation heat transfer. The time required for this can be approximated by:

$$t_{sat} = \frac{\rho_d c_{pd} D_d \left(T_{sat} - T_\infty\right)}{6\varepsilon_d \sigma T_B^4} \tag{2-18}$$

where d subscripts refer to droplet properties. In the derivation for (2-18) a number of simplifying assumptions were made. The droplet temperature was assumed to be uniform across the droplet. For the 50-100μm droplet typical of those due to entrainment in the FAST test, this is a good assumption. Also T_d^4 was assumed to be negligible compared to T_B^4 which is of course an excellent assumption during the first expansion when T_B is several thousand Kelvins and T_d is on the order of 300-400 K.

After the entrained droplets have been heated to saturation, any further heat transfer results in their vaporization. The rate of vaporization is given by:

$$\dot{m}_{cd} = Q_{rd}/h_{fgc} \tag{2-19}$$

where

$$Q_{rd} = \frac{6m_d}{\rho_d D_d} \varepsilon_d \sigma \left(T_B^4 - T_d^4\right) \tag{2-20}$$

m_d is the mass of droplets remaining, and ρ_d, D_d, ε_d, and T_d refer to the density, diameter, emissivity and temperature of the droplet.

2.2.5 Fuel Mass Transfer

After observing the film of the FAST experiments it becomes readily apparent that the entire 18g of fuel cannot be within the bubble at the start of the expansion. In most cases, the test assembly breaks on one end and therefore the fuel must flow the length of the assembly before entering the bubble. Because the flow geometry is so complex and the nature of the two-phase flow through an orifice is not well understood, only simple parametric models for $\dot{m}_f$ will be proposed at this time. The models will be discussed in a later section.

2.2.6 Solution Technique

The preceeding development results in a system of ten coupled first-order differential equations. This system is solved using a variation of the Runge-Kutta method called the Kutta-Merson technique.

2.3 Comparison of Calculated and Experimental Results

2.3.1 Experimental Results

The experimental results of greatest importance are 1) transducer pressure vs. time, 2) bubble radius vs. time, and 3) period of the bubble oscillation. These results will be used as the basis for comparison between experimental and calculated results.

The transducer pressure is measured experimentally using a transducer mounted nine inches from the test assembly. Looking at the resulting pressure trace, one can also calculate the bubble period from the time between transducer pressure peaks.

The bubble radius can be determined by two methods. First, the radius can be taken directly from the high speed movies of the experiments. Since the bubble is not spherical for most of the expansion and also since only about three quarters of the bubble can be seen through the viewing port, this calculation is only accurate to ± 10%.

The radius can also be approximated from the pressure in the cover gas if an isentropic compression of the cover gas region is assumed. If such is the case, $P'V^{\gamma}$ is constant and the bubble volume can be calculated for each time step, given the cover gas pressure.

A table of experimental results for a variety of test conditions is presented in Table 2.1. The standard deviations quoted provide a measure of the reproducibility of the experiments.

TABLE 2.1

Summary of ORNL Experimental Results

	P'(MPa)	P_x(MPa)	T_∞(K)	P_1(MPa)	a_{max}(cm)	τ(ms)	P_2(MPa)
a)	0.123	0.135	98	1.33±.07		48.5±0.4	0.35±.18
b)	0.123	0.513	298	1.26±.01	10.8±0.7	50.4±1.0	0.22±.06
c)	0.025	0.513	298	1.51±.06		174.5±5.8	0.84±.31
d)	2.02	2.02	298	2.74±.15		5.3±0.5	2.50±.10
e)	0.123	0.513	364	1.28±.09	14.5±1.3	89.6±3.0	0.14±.01

The test conditions which were varied in the FAST test were: argon cover gas pressure, P'; xenon pressure, P_x; and coolant temperature, T_∞. The reasons for examining these test parameters and a discussion of their observed effects follows.

As is evident from (2-1) the cover gas pressure can be expected to have a significant effect on the radial expansion of the bubble. In other words, by changing P' the results for R vs. t and bubble period, τ, should be altered significantly. Qualitatively, an increase in P' would decrease the acceleration at each time step which should result in a smaller bubble size and a shorter period. An approximation for this dependence was given by Herring[10]:

$$\tau = 1.829\, a_{max} \left(\frac{\rho}{P\tau}\right)^{1/2} \qquad (2\text{-}21)$$

Though not in quantitative agreement with (2-21) the results of cases (a)-(d) show that the general behavior of the experiments follow the predictions.

The xenon gas was injected into the test assembly in order to examine the effects of noncondensible gas on the heat transfer processes taking place. It has been shown by many authors that noncondensable gases can have a significant effect on condensation heat transfer. It was anticipated, therefore, that this effect could be observed indirectly by the behavior of the bubble. As shown in Table 1, however, no statistically significant effect was observed when the amount of xenon was increased by a factor of five. This may mean simply that the smaller amount of xenon was enough to produce the anticipated effect and that the additional gas was superfluous. The effect of the xenon gas cannot be evaluated fully until a successful test without the gas is completed.

Increasing the coolant temperature, T_∞, to just below the saturation temperature at the ambient pressure was expected to induce rapid surface boiling which would lead to mass flow of coolant vapor into the bubble. This influx of coolant would tend to "quench" the UO_2 thus decreasing the fuel temperature and pressure. At the same time, it would increase the partial pressure of the coolant in the bubble. The net effect, as observed in the FAST experiments, was an overall increase in the bubble pressure (as evidenced by the higher initial tranducer peaks) and a concomitant increase in the bubble radius and period.

In order to model these results, the UVABUBL model has been proposed. In the following discussion, results from the present version of UVABUBL will be presented and compared to the FAST tests.

2.3.2 UVABUBL Results

UVABUBL results are presented in Table 2-2. The results are divided into two groups depending on the fuel flow model. The two models and the order in which they are considered are, 1) constant fuel mass (no mass flow), and 2) constant mass flow rate.

The constant mass model has been chosen for a parameter study which demonstrate the sensitivity of the UVABUBL model to variations in m_f, ε_g, and K_1. This analysis is presented as cases (a) through (e) of Table 2.2. The FAST experiment modeled in these cases is considered the "base case": cover gas pressure, .123 MPa; xenon pressure, .5 MPa; and ambient temperature, 298 K.

Case (a) represents an adiabatic bubble expansion: there is no coolant entrainment, and no radiation heat transfer to the surface. As

TABLE 2.2

SUMMARY OF UVABUBL CALCULATED RESULTS

Base Case: $P' = 0.123$ MPa $P_x = 0.513$ $T_\infty = 298$ K

	m_f(g)	ε_g	K_1	P_1(MPa)	a_{max}(cm)	τ(ms)	P_2(MPa)	a_{min}(cm)
a)	18	0.0	0.0	1.39	19.2	25.4	1.39	1.5
b)	18	0.2	0.0	1.39	19.3	27.1	0.44	8.5
c)	18	0.2	0.1	1.47	20.2	25.6	0.64	7.0
d)	10	0.2	0.1	1.32	18.5	26.6	0.54	6.4
e)	5	0.2	0.1	1.31	16.7	25.6	0.94	3.1

Additional Cases with: $m_f = 18$ g $\varepsilon_g = 0.2$ $K_1 = 0.1$

	P'(MPa)	P_x(MPa)	T_∞(K)	P_1	a_{max}	τ	P_2	a_{min}
f)	0.025	0.513	298	1.29	24.4	31.7	0.36	9.7
g)	2.02	2.02	298	4.34	8.1	4.2	4.37	2.0
h)	0.123	0.513	364	1.42	20.4	26.4	0.43	11.5

Mass Flow Cases for Base Case with: $m_f = 18$ g $\varepsilon_g = 0.2$ $K_i = 0.1$

i)	$\dot{m}_f = 18$ kg/s	1.28	20.6	25.5	0.59	8.4
j)	$= 1.8$ kg/s	1.29	17.6	30.2	0.25	13.2
k)	$= 0.9$ kg/s	1.29	16.7	26.0	0.20	14.1

expected the transducer pressure peaks are identical, indicating that no energy has been lost from the bubble. Similarly, though it is not shown in Table 2.2, the radius vs. time curve repeats ad infinitum.

Case (b) includes radiation heat transfer to the surface. This not only reduces the overall bubble temperature through radiation heat loss, but it also induces surface vaporization which adds coolant vapor to the bubble. The addition of the water vapor pressurizes the bubble, which results in a slightly larger radius and period. The water also acts as a noncondensable gas, cushioning the bubble collapse and keeping the bubble from contracting to its anticipated minimum.

Case (c) adds entrainment. Vaporization of the entrained droplets is an additional source of coolant vapor. This coolant enters near the start of the expansion and results in a slightly larger initial transducer pressure peak and maximum bubble radius. Somewhat surprisingly, however, the bubble period is shorter than for case (b). This may be caused by the added quenching of this extra vapor source.

Cases (d) and (e) examine the effects of decreased fuel mass. In both cases small reductions in maximum radius and bubble period occur in accordance with what might have been anticipated due to the smaller energy content of the bubble.

As a group, cases (a)-(e) of Table 2.2 can be compared to the experimental result, case (b) of Table 2.1. The large difference in bubble radius and period demonstrates the need for further modifications of the UVABUBL model. A number of possible changes are discussed in the final section of this report.

Cases (f), (g), and (h) of Table 2.2 correspond to FAST test cases (c), (d), and (e) from Table 2.1. Again, though the trends exhibited by the experimental results are also found in the UVABUBL results, large differences exist for maximum radius and period.

The final three cases in Table 2.2 demonstrate the effects of fuel mass flow rate on the UVABUBL results. In each of these cases the flow of fuel continued until the entire 18g of UO_2 had entered the bubble.

In these cases the bubble begins as saturated vapor which fills the available test assembly volume. After the assembly breaks, the bubble expands and the remaining fuel begins to flow into the bubble. The mass flow rate given in cases (i), (g), and (k) correspond to times of 1ms, 10ms, and 20 ms for completion of the feeding process.

As might be expected, when the entire fuel mass enters during the first milliscond of the expansion, the results differ very little from the constant mass case. For the 10ms and 20 ms flow times, the maximum radius is decreased and the period is increased as required, but an additional problem appears in the results. In both cases the bubble collapses only slightly before the second expansion begins. In fact as the flow times get longer, the bubble approaches a stable radius. Unfortunately these results are not representative of what actually occurs in the experiments.

Though this simplified fuel flow model does not significantly increase the accuracy of the UVABUBL code, a mass flow model should be included for an accurate representation of the FAST experiments.

2.4 Future Improvements in UVABUBL for Underwater Experiments

Though the present UVABUBL model is able to predict the general trends demonstrated by the FAST experiments, substantial differences exist between calculated and experimental values for period and radius. In order to alleviate this problem several modifications to UVABUBL are proposed.

As shown in Table 2.2 the inclusion of a parametric model for the fuel feeding rate reduced a_{max} and increased τ, though not by the magnitudes required. It is possible that a more mechanistic model may lead to even greater improvement in the analytical results.

The bubble vapor emissivity used in the UVABUBL calculations was assumed to be constant throughout the expansion. It it known, however, that the emissivity is a strong function of bubble pressure, size, and temperature. In order to approximate the effect of variable emmisivity, this functional dependence can be assumed to be identical to that of known vapors (water, for example). Though the magnitude of the emissivity may not be correct, the behavior of the analytical solution should be closer to reality than for the present method.

In the present model even though the coolant vapor within the bubble is at high pressure and temperature relative to the bubble surface, no mechanism for coolant condensation is included. According to the kinetic theory of gases and liquids, as the pressure of the coolant vapor increases an increasingly large amount of condensation should also be taking place. In fact for larger pressures, the net mass transfer may be out of the bubble. The UVABUBL code is presently being modified to account for the

effects of kinetic theory mass transfer.

Finally, nonequilibrium effects during the early part of the expansion are being considered, and these effects may be the principal source of difference between the experiments and the calculations presented here. Continuing analysis seems to indicate that the present UVABUBL model overestimates the bubble pressure during the early phase of the expansion. Phenomena such as bubble growth and choked flow of vapor or two-phase UO_2 between the flashing UO_2 in the sample and the bubble are probably responsible for lower bubble pressure during the early phase of the bubble expansion than those predicted in the present version of UVABUBL.

2.5 Modification of Analytical Model for FAST Sodium Experiments

The UVABUBL model will also be used for the analysis of the ORNL FAST sodium tests. The model is adapted to the under sodium tests by substituting the thermodynamic properties of sodium for those of water.

Representation of the properties needed, generally as functions of temperature or pressure, are now incorporated into the UVABUBL program. The equations were based on those reported by Fink and Leibowitz[11], Thermophysical Properties of Sodium, though some were modified for use in UVABUBL. The following is a discussion of the equations and the necessary modifications. Also included is a brief discussion of some preliminary results of the analysis based on the initial sodium runs.

2.5.1 Sodium Properties

Constants

Certain properties of liquid sodium are taken to be constant as initial conditions and/or can be assumed to remain constant throughout the

calculation. Since it is anticipated that the first sodium tests will be run with the sodium at 800 K, these initial properties were obtained for that temperature. Values are listed in Table 2.3

TABLE 2.3

SODIUM PROPERTIES AT 800 K THAT REMAIN CONSTANT IN THE CALCULATIONS

Property	Value
Thermal conductivity, k	66.8 W/m·K
Thermal diffusivity, α	6.40×10^{-5} m^2/s
Specific heat at constant pressure, c_p	1263.6 J/kg·K
Density of the saturated liquid, ρ_ℓ	825.8 kg/m^3
Viscosity, μ	2.29×10^{-4} Pa·s
Speed of sound, c_o	2301.5 m/s
Gas constant, R	361.65 J/kg·K
Surface Tension, σ	0.154 N/m

These values were taken directly from Fink and Leivowitz after conversion to standard SI units using the atomic weight of sodium of 22.9898.

T_{sat} vs. P_{sat}

The next task was to define the saturation temperature, T_{sat}, as a function of the saturation pressure, P_{sat}. This was needed because in the UVABUBL code pressure is generally the known quantity and the accompanying temperature is the unknown. An equation for P_{sat} as a function of T_{sat} was found in Reference 11. Data from this equation were curve-fit to an equation for T_{sat} as a function of P_{sat}. In order to get good results, two equations were required, one for the region where

$\ell n\ P_{sat} \leq 1.407$, and one for the region where $\ell n\ P_{sat} > 1.407$, where P_{sat} is in MPa. These equations are:

$$\ell n\ P_{sat} \leq 1.407 \quad T_{sat} = (6.703 \times 10^{-4} - 8.086 \times 10^{-5}\ \ell n\ P_{sat})^{-1} \quad (2\text{-}22)$$

$$\ell n\ P_{sat} > 1.407 \quad T_{sat} = 1387\ (P_{sat})^{.1808} \quad (2\text{-}23)$$

These equations resulted in a fit that had an absolute error of no more than 12 K or relative error 1% at any point on the curve. There was a small discontinuity of 8 K at $\ell nP = 1.407$, T = 1800 K where the equations changed. This discontinuity introduced an error that was smaller than the maximum relative error, thus it was of little consequence.

Saturated Enthalpy And Density As A Function of Temperature

The next set of properties needed were the enthalpies at saturation, that is h_ℓ, h_g, and $h_{\ell g}$. The saturation temperature was used to compute the enthalpy values. Equations for h(T) were found in Fink and Leibowitz and were used directly after converting units from J/mol to J/kg. There were two sets of equations, one for $T_{sat} > 1644$ K and one for $T_{sat} < 1644$ K. This division occurred because the data used by Fink and Leibowitz for $T_{sat} < 1644$ K are well known, quite accurate, and are based on past work by Padilla. The equations above 1644 K came from a compilation of different data sources made by Fink and Leibowitz and represent what they consider the "best" fit to the available data. The equations for $T_{sat} < 1644$ K and $T_{sat} > 1644$ K are presented below, with the standard deviation shown in parentheses, where T_{crit} is the critical temperature and equals 2509.46 K, and h is in J/kg.

For T_{sat} < 1644 K:

$$h_{\ell g}(T_{sat}) = 43.497\ [3.3305 \times 10^4\ (1-T_{sat}/T_{crit}) + 8.01112 \times 10^4\ (1-T_{sat}/T_{crit})^{0.2}]\ (\pm 12\%) \quad (2\text{-}24)$$

$$h_{\ell}\ (T_{sat}) = 43.497\ [-7.1393 \times 10^3 + 35.206\ (T_{sat})^2 + 2.5711 \times 10^{-6}\ (T_{sat})^3 - 1.2428 \times 10^5/T_{sat}]\ (\pm .14\%) \quad (2\text{-}25)$$

$$h_g\ (T_{sat}) = h_{\ell} + h_{\ell g} \quad (2\text{-}26)$$

For T_{sat} > 1644 K:

$$h_{\ell g}\ (T_{sat}) = 43.497\ [T_{crit}(43.402)(1 - T_{sat}/T_{crit})^{0.32227}](\pm 12\%) \quad (2\text{-}27)$$

$$h_{\ell}\ (T_{sat}) = 43.497\ [81678 + 18.525\ (T_{sat} - 1644.26)] - 0.5h_{\ell g}(\pm 2\%) \quad (2\text{-}28)$$

$$h_g\ (T_{sat}) = h_{\ell g} + h_{\ell} \quad (2\text{-}29)$$

The density of the saturated liquid was presented in much the same manner as the saturated enthalpy. The equation in Fink and Leibowitz for $\rho(T_{sat})$ was used directly in UVABUBL. Again there was a division of the equations into one for T_{sat} < 1644 K and one for T_{sat} > 1644 K for the same reason cited previously. The units are kg/m^3.

For T_{sat} <1644 K:

$$\rho(T_{sat}) = 1011.8 - 0.22054\ (T_{sat}) - 1.9226 \times 10^{-5}\ (T_{sat})^2 + 5.6371 \times 10^{-9}\ (T_{sat})^3 \quad (2\text{-}30)$$

For T_{sat} > 1644 K:

$$\rho(T_{sat}) = 214.1\ [1.\ 2.3709\ (1 - T_{sat}/T_{crit})^{0.31645} + 2.8467 \times 10^{-7}\ (T_{crit}-T_{sat})^2 \quad (2\text{-}31)$$

Superheated Enthalpy and Specific Heat

The next properties that needed to be included were the enthalpy and the heat capacity at constant volume (c_v) for superheated sodium vapor. Data

for superheated enthalpy was found in Fink and Leibowitz only up to 1644 . . Since temperatures in the bubble were expected to reach as high as 5000 K, for treating higher temperature vapor. The method chosen was to represent the sodium vapor as a Van der Waals gas for temperatures and pressures not given by Fink and Leibowitz. The region included in the Fink and Leibowitz analysis contained temperatures from 400 K to 1644 K and pressures from 10^{-11} MPa to 1.0 MPa. The enthalpy in this region was computed using a quasi-chemical approach which assumes that deviation from ideal gas behavior occurs due to association reactions and results in the formations of a dimer and a tetramer.

For superheated enthalpy values in the region not covered by Fink and Leibowitz, the deviation from ideal gas behavior was corrected for by using the van der Waals equation. This equation includes the effect of changing pressure as opposed to the ideal gas which does not take this into account.

This division of the superheated vapor region resulted in a discontinuity were avoided in the program because UVABUBL uses a relative enthalpy called HBSAT. This relative enthalpy value is defined as the superheated enthalpy (h_{sup}) minus the saturated vapor enthalpy h_g, or:

$$HBSAT = h_{sup} - h_g \qquad (2\text{-}32)$$

HBSAT was computed by skipping over the discontinuity. This was done by dividing the superheated region into four areas. The first area included all temperatures at all pressures below 10^4 Pa. In this region, HBSAT was computed directly from Eq. (2-32) because the discontinuity becomes increasingly small as the vapor approaches ideal gas behavior. The second region included temperature below 1599 K, between 10^4 and 1.798×10^6 MPa. In this region HBSAT was computed by the relation:

$$HBSAT = [h(T) - h(1600)] + [h(1599) - h_g] \quad (2\text{-}33)$$

This allowed us to skip over the discontinuity marked by the shaded area in Fig. 2.3. The fourth region included temperatures above 1600 K at pressures greater than 1.798×10^6 Pa. HBSAT was computed again by Eq. (2-32), where in the fourth region h_g was a value determined by the van der Waals equation rather than the quasi-chemical method. This h_g was inconsistent with h_g for $T > 1644$ K as computed by equation (2-28). However, this was not important because this van der Waals h_g was used only when computing HBSAT. To have used the quasi-chemical h_g for the fourth region would have resulted in values for HBSAT that were consistently too large. This was due to the large discontinuity between the van der Waals and the quasi-chemical methods at high temperatures (>1600 K) and pressures ($>1.798 \times 10^6$ Pa).

Values for c_v were computed from enthalpy data by the relation:

$$c_v = \left(\frac{\partial u}{\partial T}\right)_v = [h_{sup}(T) - RT] - [h_{sup}(T + 1) - R(T + 1)] \quad (2\text{-}34)$$

Thus only the enthalpy needed to be determined directly.

Specific Volume of the Saturated Vapor

The specific volume of the saturated vapor was the next property needed for UVABUBL. This was calculated using the Clapeyron equation as presented in Fink and Leibowitz. The units are m^3/kg.

$$v_g = [h_{\ell g}/T \left(\frac{\partial P}{\partial T}\right)_{sat} + 1/\rho_\ell] \quad (2\text{-}35)$$

Where $h_{\ell g}$ is the heat of vaporization and is given by Equations (2-24) and (2-27),

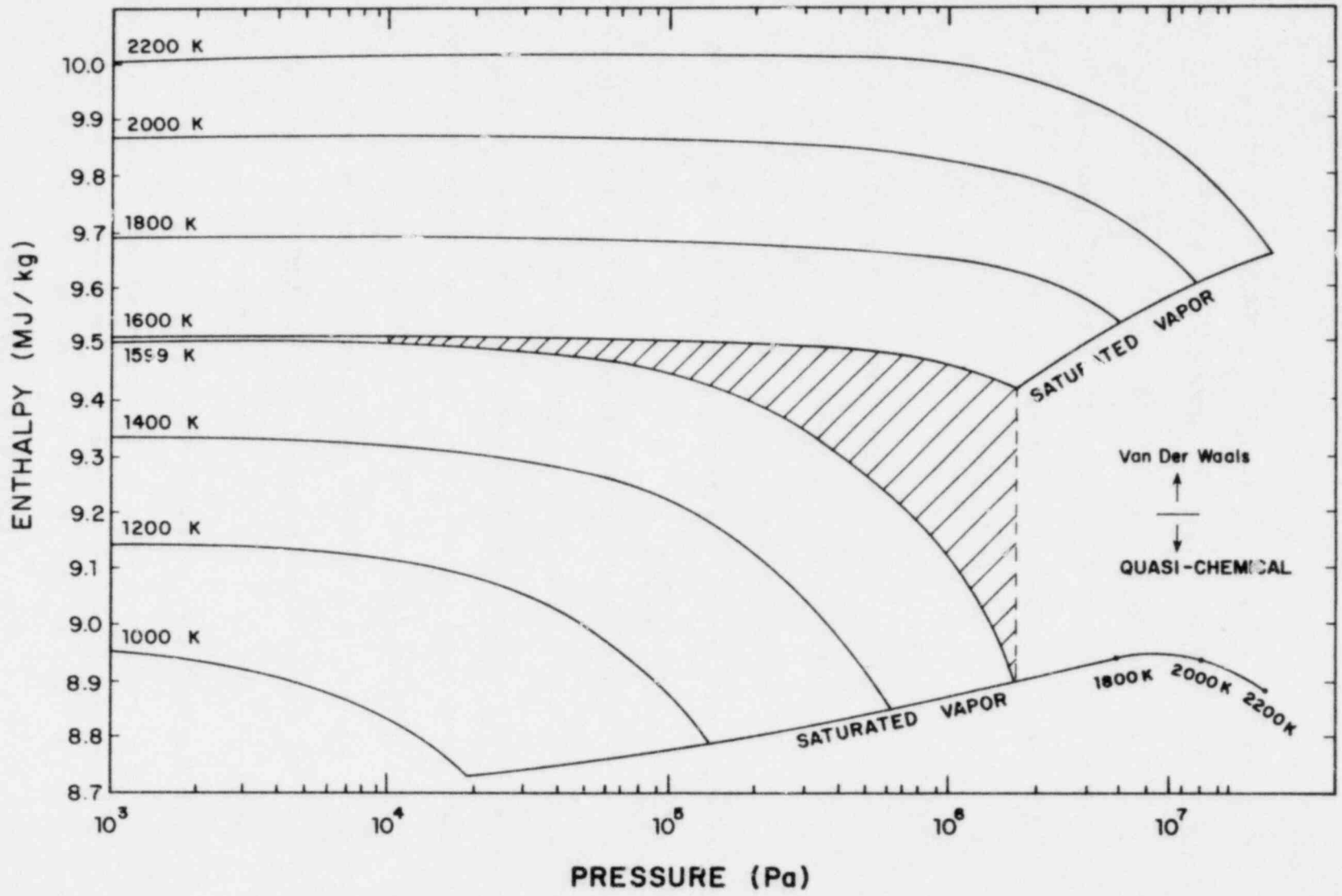

Figure 2.3. Enthalpy of sodium vapor as a function of pressure and temperature.

and

$$(\partial P/\partial T)_{sat} = 101325\ [13113/T^2 - 1.09478/T + 1.9777 \times 10^{-4}$$
$$\times\ [\exp\ (18.832 - 13113/T - 1.0948\ \ln(T) + 1.9777 \times 10^{-4} T] \qquad (2\text{-}36)$$

also ρ_f is given by Eqs. (2-30) and (2-31). For $T < 1644$ K the estimated error was 2%; for 1644 K<T<2000 K the estimated error was 12%; for 2000 K<T<2400 K the estimated error was 20%; and for 2400 K<T<2500 K the estimated error was 50%.

Derivatives

Also required for the adaptation to sodium properties were the derivatives with respect to temperature of v_ℓ, v_g, h_ℓ, h_g, and P_{sat}. $(\frac{\partial P}{\partial T})_{sat}$ was already given as Eq. (2-36). The remaining four derivatives were computed by straightforward differentiation of the respective functions.

2.5.2 Preliminary Results

Preliminary results were obtained from runs of the UVABUBL program that were made to test the sodium properties. That is, several runs were completed to ascertain that the properties were correctly added to the program and did not cause logical errors that in turn would have interrupted the program. Thus, these runs were made with only one set of parameters that may or may not be a valid representation of what the actual conditions are.

One favorable preliminary result was that the sodium properties, as presented above, did fit into the program and they seemed to work quite well. However, there were some problems, either in the model itself or only with the parameters, that still need to be worked out. One of these was that after

about 50 millisec., at the beginning of the second oscillation the bubble volume consisted of approximately 2/3 entrained droplets. This, in turn, caused the bubble pressure and temperature to exceed the critical points. This was probably not an accurate prediction of what actually occurs. More work is needed in this area.

Another important preliminary result, that was most interesting, was that there was no vaporization of sodium from the bubble surface. The surface temperature remained well below the saturation value. In addition, the thermal boundary layer became quite thick compared to the water results. All of these effects were due to the high conductivity of the liquid metal, 66.8 W/m·K opposed to 0.604 W/m·K for water.

REFERENCES

1. A.L. Wright, T.S. Kress, and A.M. Smith, "Preliminary Assesment of the FAST Under-Water Test Results," to be published, Oak Ridge National Laboratory.

2. A.L. Wright, H.W. Bertini, T.S. Kress, M.L. Tobias, M.J. Kelly, L.F. Parsley, and J.S. White, "Effect of Energy Density on Aerosol Yield and Primary Particle Sizes Produced by the Capacitor Discharge Vaporization of UO_2," NUREG/CR-0120, ORNL/NUREG/TM-163, Oak Ridge National Laboratory (October 1978).*

3. A.L. Wright and A.M. Smith, "Updated Work Plan for the FAST/CRI-III Fuel Vaporization and Transport Experiments," NUREG/CR-0084, ORNL/NUREG/TM-326, Oak Ridge National Laboratory, (October 1979).*

4. C.A. Erdman, A.B. Reynolds, D.R. Bradley, K. Chen, and M. Pilch, "Bubble Behavior in LMFBR Core Disruptive Accidents, Annual Report, October 1977-September 1978," NUREG/CR-0604, University of Virginia (March 1979).*

5. A.B. Reynolds and G. Berthoud, "Expansion and Collapse of Large Two-Phase Bubbles: II. Analysis, "Advances in Heat and Mass Transfer at Air-Water Interfaces, The American Society of Mechanical Engineers, pp. 41-54 (December 1978).

6. T. Theofanous, L. Biasi, H.S. Isbin, and H. Fauske, "A Theoretical Study on Bubble Growth in Constant and Time Dependent Pressure Fields," Chemical Engineering Science, Vol. 24, pp. 885-897 (1969).

7. G.I Taylor, "The Instability of Liquid Surfaces When Accelerated in a Direction Perpendicular to their Planes. I, "Proceedings of the Royal Society of London, Vol. 202 (1950).

8. M. Corradini, W.M. Rohsenow, and N.E. Todreas, "Effects of Sodium Entrainment and Heat Transfer with UO_2 Vapor During an HCDA, "Transactions of the American Nuclear Society, Vol. 30, pp. 456-457 (November 1978).

9. D.Y. Hsieh, "Effects of Heat and Mass Transfer on Rayleigh-Taylor Instability," Transactions of the ASME, p. 156-162 (March 1972).

10. C. Herring, "Theory of the Pulsations of the Gas Bubble Produced by an Underwater Explosion," Underwater Explosion Research--a compendium of British and American Reports, Vol. III, The Gas Globe, pp. 35-130, Office of Naval Research, Dept. of the Navy (1950). (Orginial work performed in 1941).

11. J.K. Fink and L. Leibowitz, "Thermophysical Properties of Sodium," ANL-CEN-RSD-79-1, Argonne National Laboratory (May 1979).

*Available for purchase from the NRC/GPO Sales Program, U.S. Nuclear Regulatory Commission, Washington, DC 20555, and/or the National Technical Information Service, Springfield, VA 22161.

3. MEASUREMENT OF PARTICLE SIZES FROM FLASHING

R.C. Anderson, C.A. Erdman, R.R. Humphris, and A.B. Reynolds

3.1 Introduction

As a part of the fast reactor safety program sponsored by the Nuclear Regulatory Commission, droplet formation during a hypothetical core disruptive accident (HCDA) has come under examination for two reasons. The first is a radiological consideration: very small droplets can remain airborne for longer periods of time and thus have a higher probability of escaping the multiple containments and reaching the environment. The second reason is that accurate thermal-hydraulic modeling requires a particle size distribution.

The University of Virginia Nuclear Engineering Department has begun work to examine the phenomenon of droplet formation and obtain size distributions due to static flashing.* An apparatus which will boil a volume of water by bulk depressurization below the vapor pressure has been designed and fabricated. Work has begun on installation of the apparatus, and various components have been tested and modified to improve system performance. The theory of hydrodynamic fragmentation will also be examined and developed further as needed.

3.2 Experiment Description

Chamber Design

To generate droplets by means of rapid bulk boiling, a small volume quick-opening chamber was designed and fabricated with the capability to

---

*The breakup of superheated jets has been correlated,[1] but no prior work has been done to obtain the sizes of droplets formed by flashing due to bulk depressurization.

heat the contained liquid to 200°C at pressures up to 1.48 MPa. The chamber is shown in Figure 3.1. It is machined from a cast aluminum block, with holes bored in it for: the chamber cavity itself, 45 mm deep, volume 16,400 mm^3 (17,300 mm^3 when the volume of the injection line to the first isolation valve is included); quartz windows on each side for visual and photographic observation; the liquid injection/pressurization line; heater elements (which heat the aluminum block but do not penetrate the cavity itself); and pressure and temperature instrumentation. The chamber is bolted directly to a wall-mounted frame to provide rigid support during the experiments.

A stainless steel faceplate, machined with O-ring grooves on each side, provides an effective seal between the chamber and the door. Two retainer plates, bolted to the chamber through the faceplate, hold the door in place until blowdown and act as guides for the door during its opening. The door seals the chamber; its quick removal begins rapid chamber depressurization. Both the door and the retainer plates are also stainless steel.

Door-Opening Mechanism

Bulk depressurization-induced boiling requires opening the door on a time scale which is short compared to the flashing phenomena. Several different opening devices were examined and the best was found[2] to be a weighted rod, accelerated by gravity, which while falling catches a wire attached to the door and initiates the door opening (see Figure 3.2). Once free of the chamber, another wire guides the door into a foam cushion.

This technique resulted in a total door opening time of 64 millisec, which is considered satisfactory for the flashing experiment.

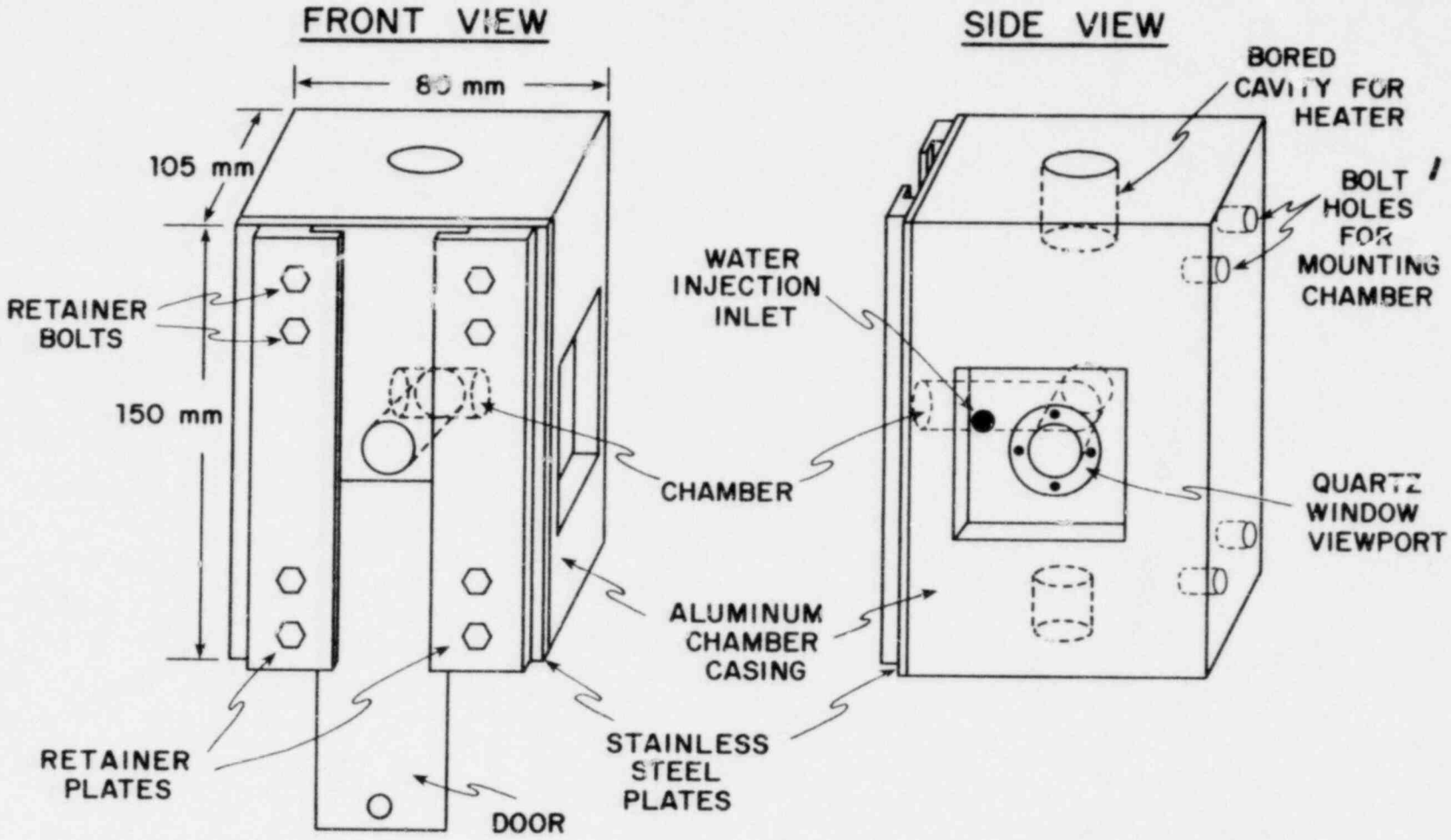

Figure 3.1. Flashing chamber.

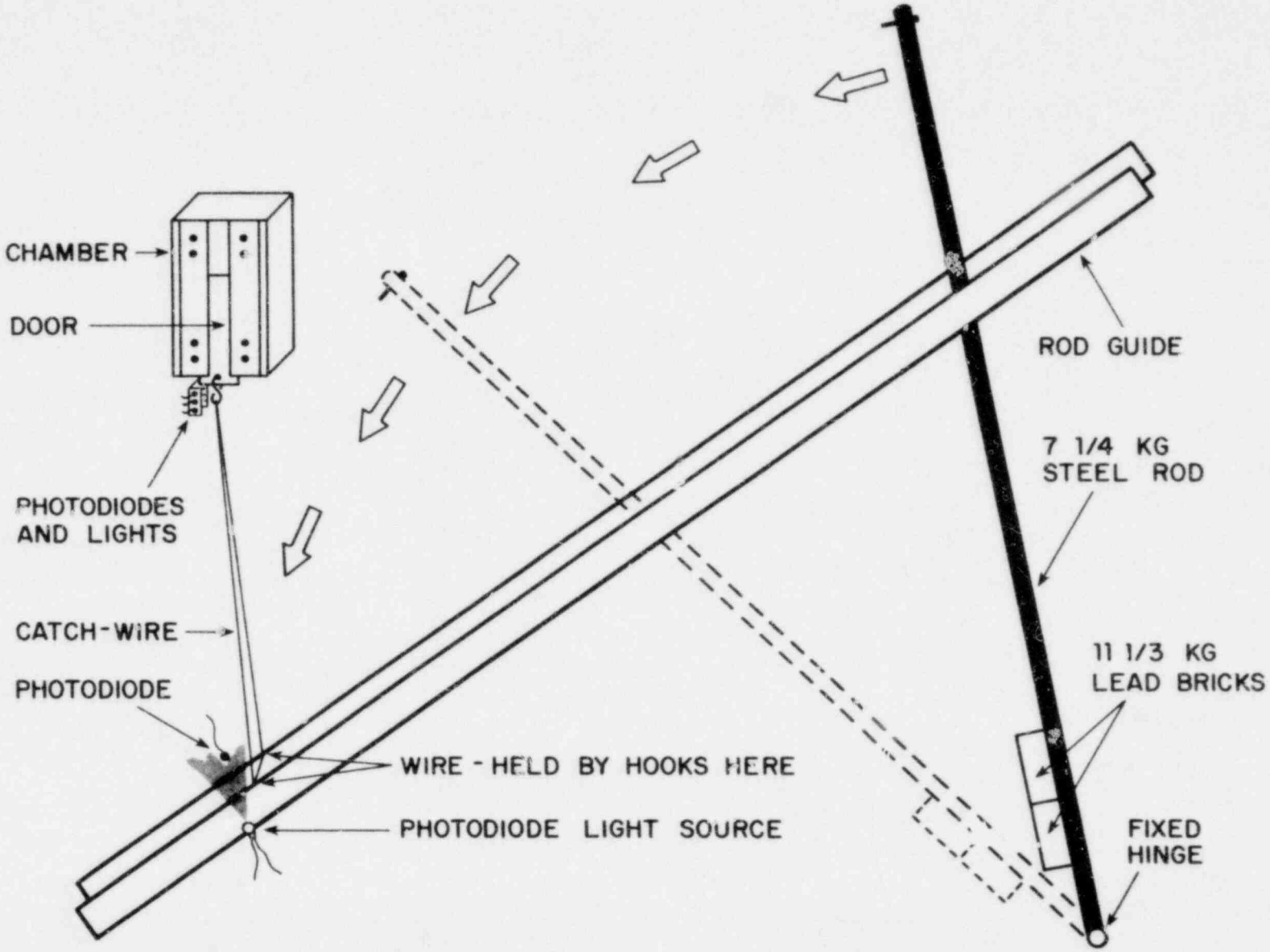

Figure 3.2. Door-opening mechanism.

The rod used to open the door is a 7.25 kg steel bar 1.83 m long. It is attached to a fixed hinge from which it may swing freely, Two lead bricks, each 11.5 kg, are attached with hose clamps to the rod at a position selected to give the rod maximum velocity. Velocities were predicted with a simple dynamics calculation and verified with a photodiode placed near the point where the rod catches the wire. A rod guide, made from two pieces of slotted angle steel, restricts the lateral motion of the rod while having a negligible effect upon its vertical motion. This insures that the force applied to the door is in the plane of the door only; in early experiments without a rod guide, lateral forces bent the door.

The wire, a double loop of 3.2 mm stainless steel, is attached to the door with an S-hook and held in place on the rod guide in the path of the falling rod by two down-turned wire hooks. This fixes the opening force vertically in the plane of the door. A protruding bolt in the tip of the rod insures that the wire will not slip off the end.

Three additional photodiodes are placed directly beneath the door to record its motion as the cavity is uncovered. The photodiodes signal the times at which door-opening begins, and ends, as well as providing time intervals for several average-velocity calculations. In an unexpected yet favorable development, the door velocity was found to exceed the rod velocity by a factor of a third, with typical rates of 9.1 m/sec for the rod and 12.1 m/sec for the door. This phenomenon is attributed to the elastic properties of the rod and the catch-wire.

Door velocities were measured with the photodiode signals for various torques on the retainer plate bolts, system pressures, rod masses and rod mass configurations. Optimum bolt torques and rod assembly configuration were determined which give the quickest opening time, with no dependence upon

chamber pressure. With only one lead brick attached to the rod, opening time increased with increasing pressure. Calculations indicated that only a very small velocity increase could be attained by adding more bricks to the rod, while actually doing so is very difficult. As such, the present door-opening time interval is considered satisfactory and no further modifications are expected at this time.

Instrumentation

In addition to droplet collection for size measurement, fluid conditions and a time reference are also recorded. Figure 3.3 illustrates the locations of the instruments. One fast-(few millisecond) and two slow-response thermocouples penetrate the chamber cavity at various distances from the cavity opening. Thermocouples may also be attached to the chamber exterior to monitor temperatures there. On the opposite side, a PCB pressure transducer (for following fast transients) is placed in a hole bored in the chamber wall. A Validyne differential pressure transducer samples the fluid pressure relative to atmospheric in the chamber injection line. This transducer is located downstream of the last isolation valve and about 170 mm from the cavity.

Positioned directly below the door to record its location and velocity without impeding its motion are three photodiodes. They are placed so that the moving door begins to block off the light beam on the first photodiode just as the cavity begins to be uncovered. Similarly, beginning of interruption of the second light beam coincides with the completion of the chamber's opening. The cavity diameter and the time interval between the interruption of the light beams on these two photodiodes provide an average door velocity. An additional photodiode provides an estimate of the rod velocity near the point where the rod first pulls on the catch-wire.

Hydraulic Design

The system must have the capability to inject and pressurize high-purity water. The piping diagram is shown in Figure 3.4. A vacuum pump is connected

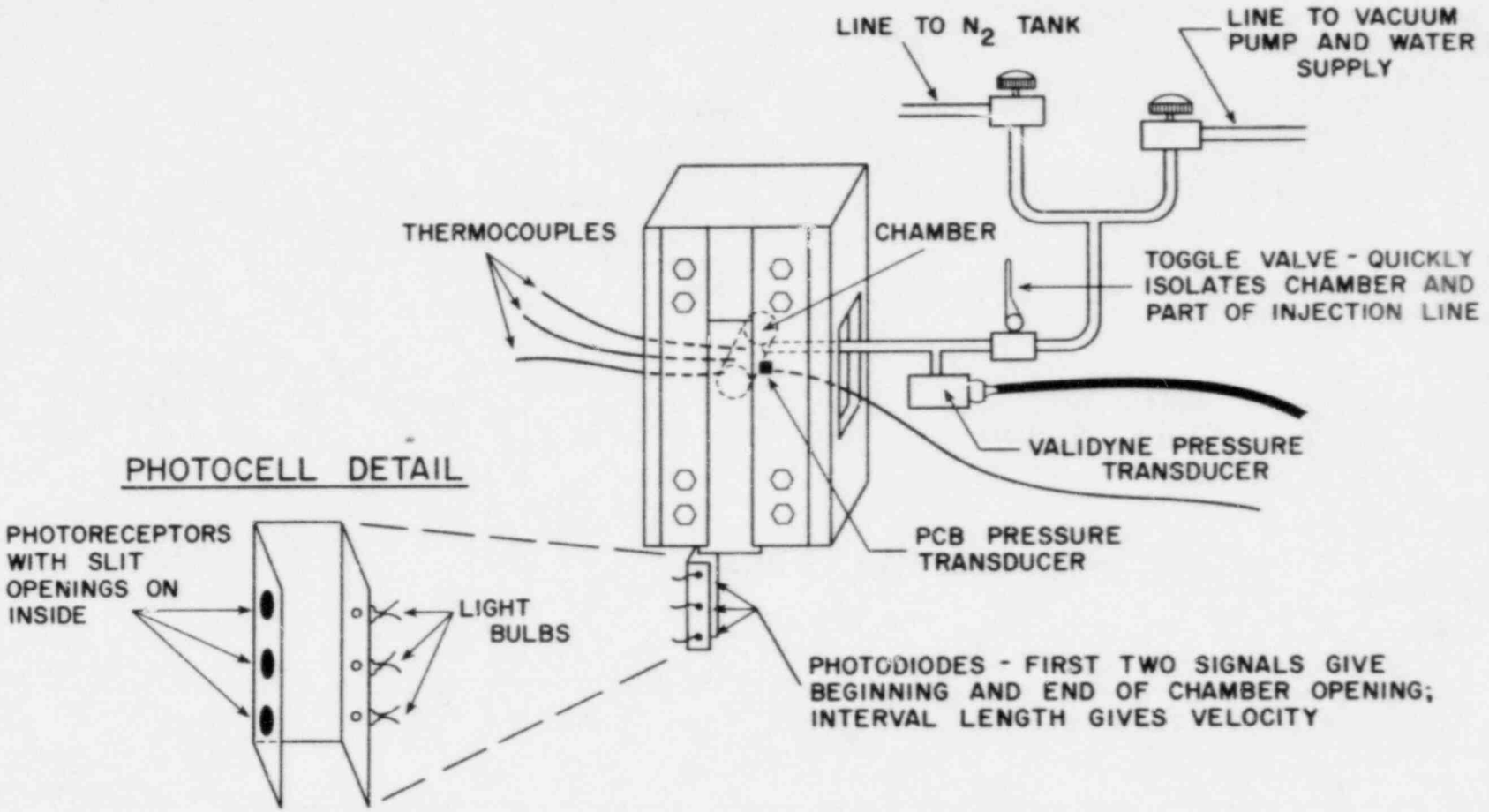

Figure 3.3. Instrumentation.

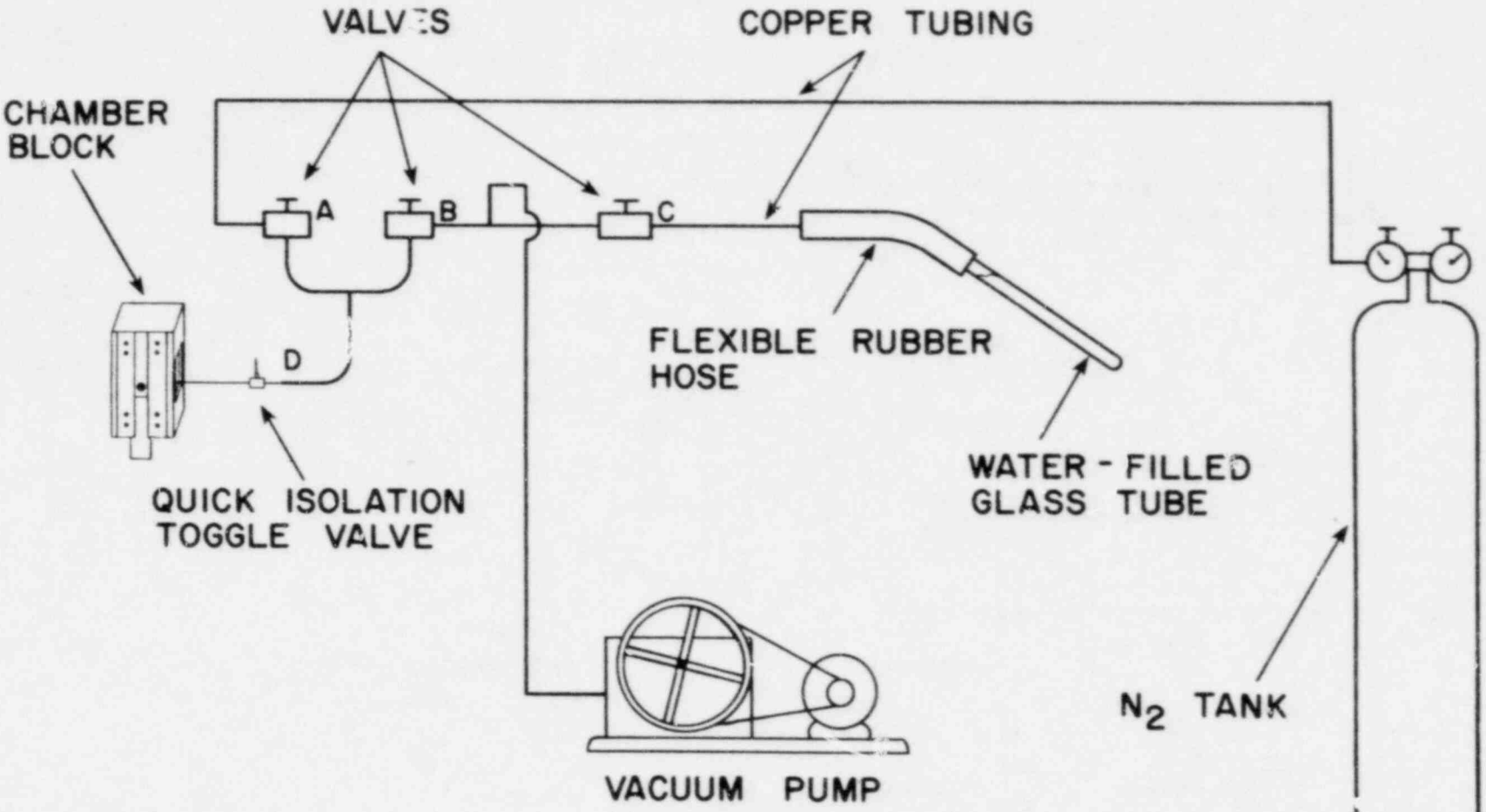

Fig. 3.4. Piping layout

to the system to evacuate the chamber prior to filling it with water. This eliminates most of the air which would otherwise be trapped in the critical water volume, or prevent filling of the chamber cavity through the narrow copper tubing (3 mm ID). After closing the line to the chamber and opening the line to the glass tube, the apparatus also pumps on the water volume before injection into the chamber, thereby removing any dissolved air from the distilled water. Once the chamber is filled, the water is pressurized by nitrogen gas.

Thermal Design

To heat the water, two resistance heaters are located in holes bored in the top and bottom of the aluminum block. The heaters are made with insulated heater wire wrapped on a 50 mm piece of steel pipe and filled with packed asbestos insulation (see Figure 3.5). The wire is wrapped in threads cut into the outer surface of the pipe and held in place by a high temperature epoxy. When in use, transformer oil is poured around the upper heater to provide an effective heat transfer medium to the aluminum block. The lower heater is wrapped with fiberglass cloth so that is fits snugly into its cavity. Two 110 volt Variacs (variable voltage controls) permit independent regulation of the power dissipated by each heater. The two heaters can generate a total of 280 watts.

Heat is conducted from the heaters to the chamber block, and then it turn from the block to the liquid volume itself. To help keep the chamber temperature uniform, the entire aluminum block is covered with two layers of 15 mm plywood insulation during heatup, with holes or slits cut as needed for the pressure line, heater wires and instrumentation (see Figure 3.6). The plywood is painted with a heat resistant paint. The wooden faceplate may be removed just before blowdown, and form-cut plugs covering the quartz windows may

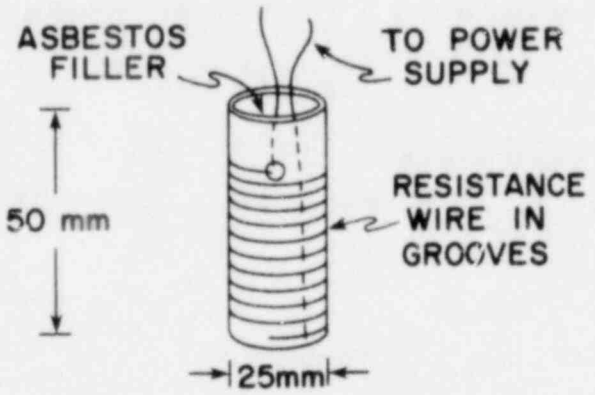

Figure 3.5. Heater design.

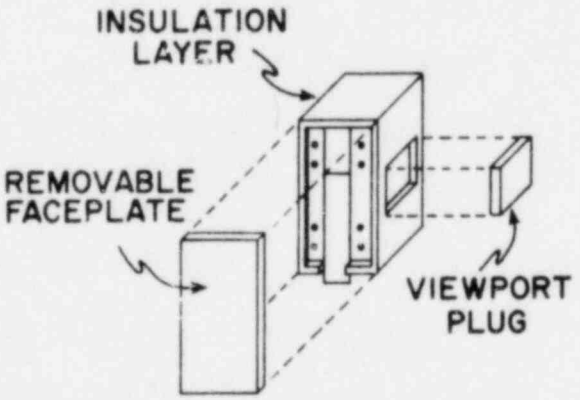

Figure 3.6. Plywood insulation.

also be removed to observe or photograph the chamber's interior. Heat loss to the air via natural convection when these three components are removed is negligible for short periods of time. The chamber water can be heated to more than 150°C in about an hour; a typical plot of temperature versus time is shown in Figure 3.7.

Droplet Collection and Photography

Size measurement requires collection of the droplets after fragmentation. Absorbing paper is attached to a rapidly rotating wheel which catches the the droplets when placed in the path of chamber blowdown. When the cahmber door opens and the depressurized water flashes, the fragmented droplets are propelled outward until they strike and leave an imprint on the blotter paper. A correlation between droplet diameter and imprint size has been developed[3] for water which contains a $Co\ Cl_2 \cdot 6\ (H_2O)$ salt solution. Results for this technique are described in Section 3.3. Variation in water properties will have to be taken into consideration in the theoretical analysis, however. Whether high-speed photography can be used to measure droplet size is yet to be determined.

The collecting paper, as indicated above, is mounted on a bicycle wheel and frame, supported by a portable steel structure which rests on the floor. Hand-driven, the wheel's perimeter velocity is about 10 m/sec, resulting in one revolution every 300 milliseconds. The moving collector paper is less than 45 mm wide, and is supplemented with stationary collector paper to provide a large collector surface area. Early tests have shown that secondary fragmentation does not occur within about the first 200 mm after expulsion from the chamber.

Currently available for high-speed photography is a Wollensak Fastax 9000 frames-per-second camera, which can be used to observe the chamber interior through the quartz windows on either side, or at the chamber opening.

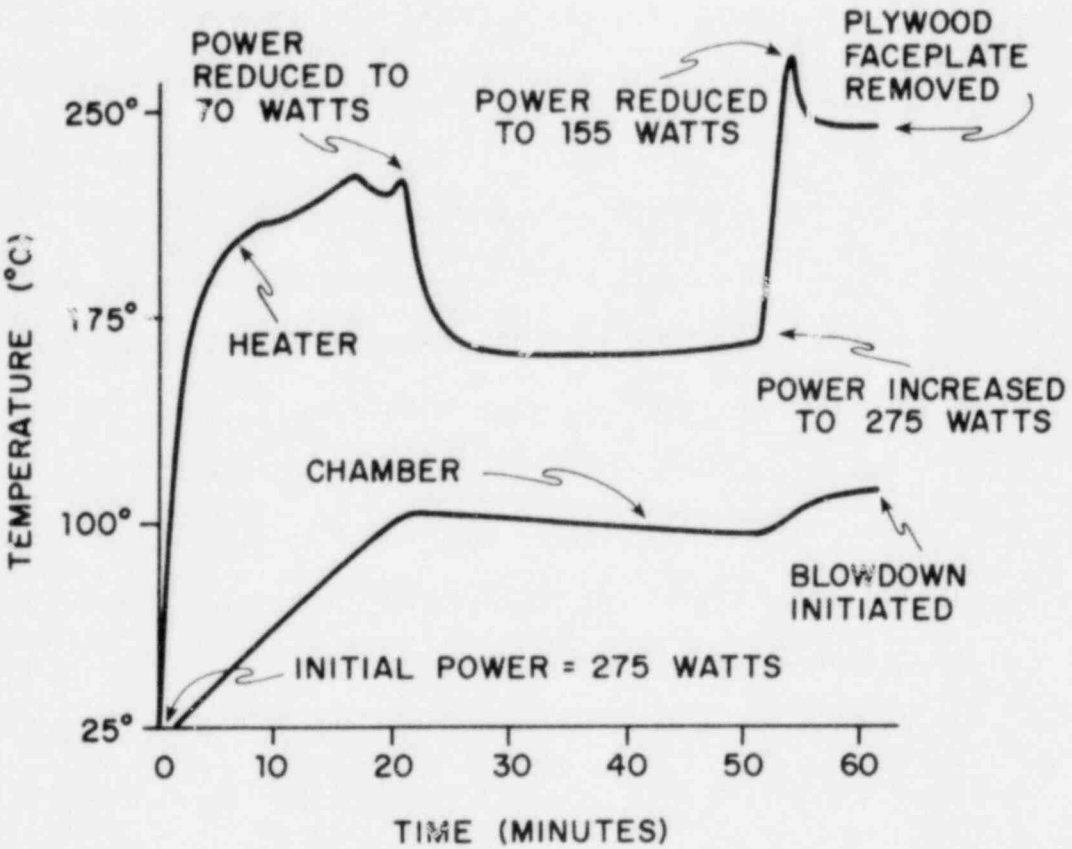

Figure 3.7. Temperature-time traces of upper heater and chamber liquid during heatup of Test F-4.

The camera will be used to obtain qualitative and, if possible, quantitative information about the fragmentation process outside the chamber as well as about bubble formation and growth in the chamber interior.

Test Procedure

Before each test the chamber door, retaining plates and contacting surface are cleaned and freshly lubricated with stopcock grease. Once the door is in place, the door bolts are tightened down to the proper torque, and the vacuum pump begins to evacuate the chamber. Left running overnight, the pump typically lowers the chamber pressure to below 30 μm Hg (less than 4 Pa).

After the chamber pressure is acceptably low, the chamber line is closed (valve B in Figure 3.4) and the line to the water-filled glass tube is opened (valve C). The vapor pressure of water at room temperature is about 20 mm Hg, and the vacuum system pumps at this pressure for an interval of about 40 seconds to remove dissolved air. The vacuum pump is then shut off. The tube is raised so that the water in it runs down to the chamber isolation valve (B). Valve A is also closed. The residual air in the chamber is at 30 μm Hg, whereas the water is at about 20 mm Hg; the combined forces of differential pressure plus gravitational head drive the water into the chamber when its isolation valves are opened, thus flooding it. The residual air, in the chamber dissolves completely when the chamber is pressurized to one atmosphere. With water at 0.1 MPa the air takes up approximately .003% of the total chamber volume; this fraction becomes even smaller at test pressures.

Once filled and pressurized, the chamber is heated. The wooden faceplate is attached during this time. Valves A and D are left open to the pressure

tank during the heating phase because of the volumetric expansion of the water with increasing temperature. Valve B is closed. Both chamber and heater temperature are also monitored.

During the instrumentation check, the weighted rod is lifted to its vertical position. The catch-wire is hung from the door (which protrudes slightly through the plywood insulation) and attached at its lower end to the rod guide. When the desired chamber temperature and pressure have been attained, the chamber faceplate is removed. If necessary, the wooden plugs covering the quartz viewpoint may be removed also. The camera is positioned to take the desired photographs, and the collector wheel and stationary collector paper are placed in front of the chamber in the path of blowdown. Paper is attached to the wheel, and it is accelerated to about 200 rpm. Once the electronic data are being recorded and the camera and wheel are running, the rod can be released to initiate the chamber blowdown. During the transient, chamber temperatures, pressures and timing signals are simultaneously recorded on a multichannel high-speed tape recorder. Later this information can be transcribed at a much slower speed (reduced by a factor of 64) to a strip chart recorder or other suitable device.

3.3 Status and Experimental Results to Date

Six different tests have been performed at various stages of fabrication and installation of the chamber and collector to evaluate component and system performance. The system is leak tight, although the thermocouple penetrations must be periodically inspected and resealed. The quartz windows show no tendency toward failure at 1.72 MPa; normal test pressures are not expected to exceed 1.48 MPa. With the plywood insulation and the heaters now in use, the thermal behavior of the chamber is acceptable, although it is necessary to monitor the heater temperatures during warmup because of their short time constants. The instrumentation is functioning satisfactorily both in monitoring and recording fluid conditions and reference times.

Some typical pressure and temperature traces are shown in Figures 3.8 - 3.10. The picture in Figure 3.8 is of an oscilloscope trace and shows the extremely rapid depressurization rate in the chamber itself (0.93 MPa in 0.56 ms, or 1655 MPa/s) recorded by the PCB transducer. The step function at the top of the picture is the composite signal from the photodiodes, and provides a time reference for the pressure traces. The oscillation of the Validyne trace, occurring on the injection line 170 mm from the chamber, is too slow to be acoustic in nature and is thought to be an inertial effect of blowdown in the long, thin pipe. The overlaid trace of the photodiodes provides a time reference and shows that the pressure increases slightly before the door begins to open; the depressurization is completed well before the chamber is completely uncovered.

Figure 3.9 shows the Validyne pressure traces from tests F-3 and F-4. The slight pressure rise before blowdown is clearly seen in F-4 as well as its oscillation, whereas steam compression in the two-phase mixture of test F-3 both prevented the pre-blowdown pressure spike and severely damped its oscillation.

An overlay of the timing, temperature and both pressure traces is shown in Figure 3.10. Because of recorder pen offset the traces are not aligned in time, but vary by several milliseconds; certain qualitative and quantitative conclusions can nevertheless be drawn. The pressure traces are similar, as expected, with only the Validyne showing any oscillation. Both transducers indicate a pre-blowdown pressure spike of 0.18 MPa. The temperature also drops quickly, but its rate of change is slow relative to the time scale for depressurization. The chamber is seen to uncover completely in about 1.6 millisec, and by adjusting for the marker offset the relative times of door-opening and depressurization may be determined. The rise in the PCB trace after depressurization is due to temperature sensitivity of the detector.

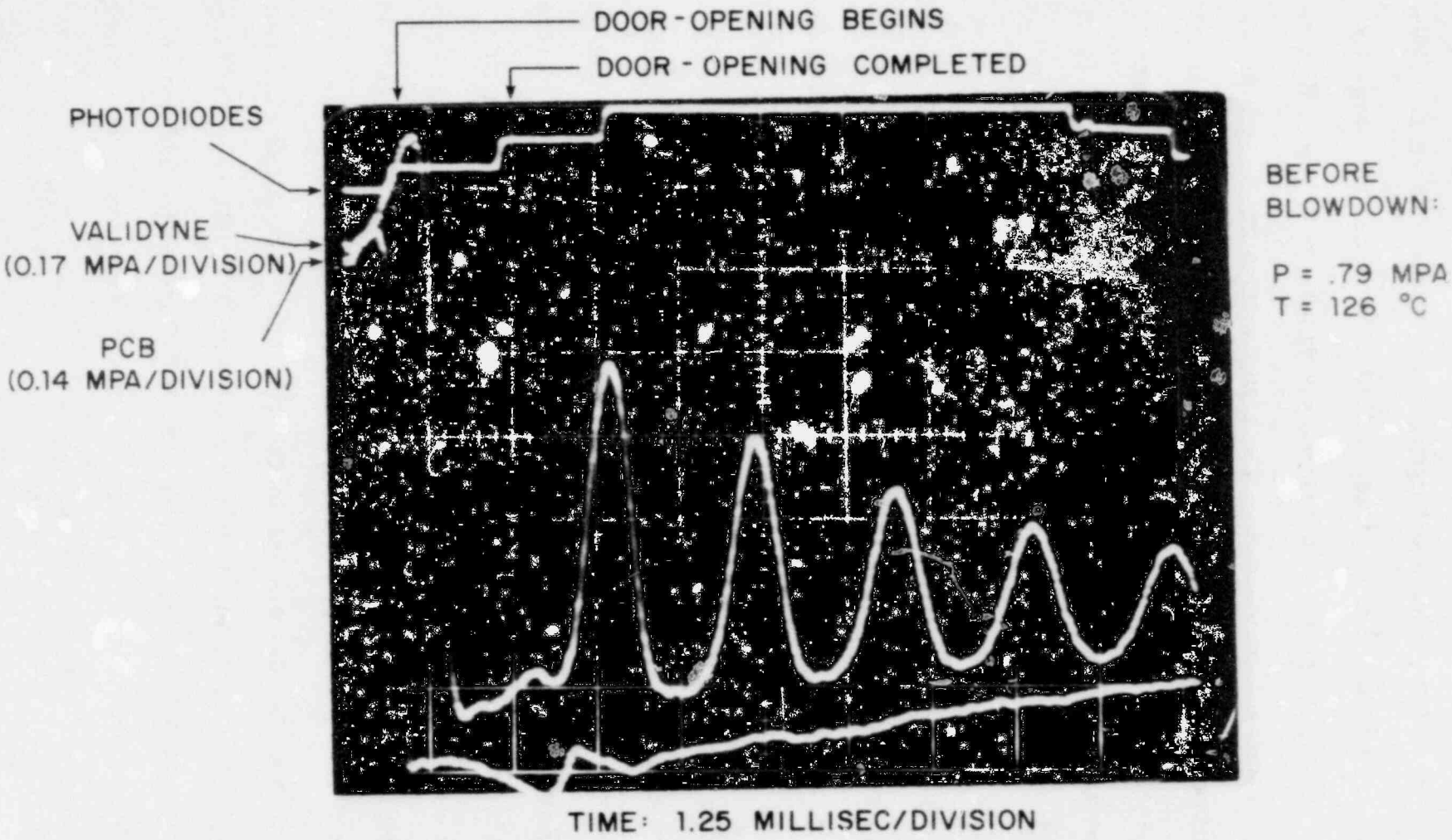

Figure 3.8. Pressure traces of Test F-5

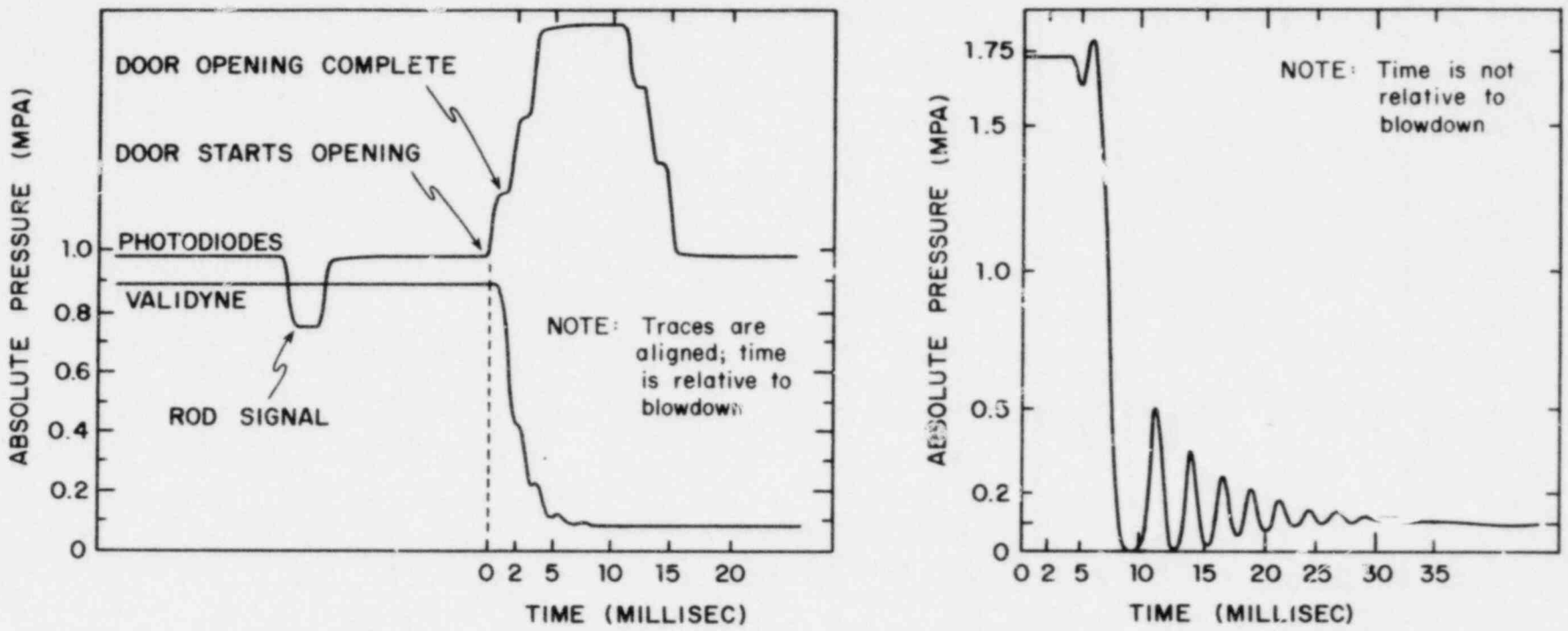

Figure 3.9. Validyne pressure traces from Tests F-3 and F-4.

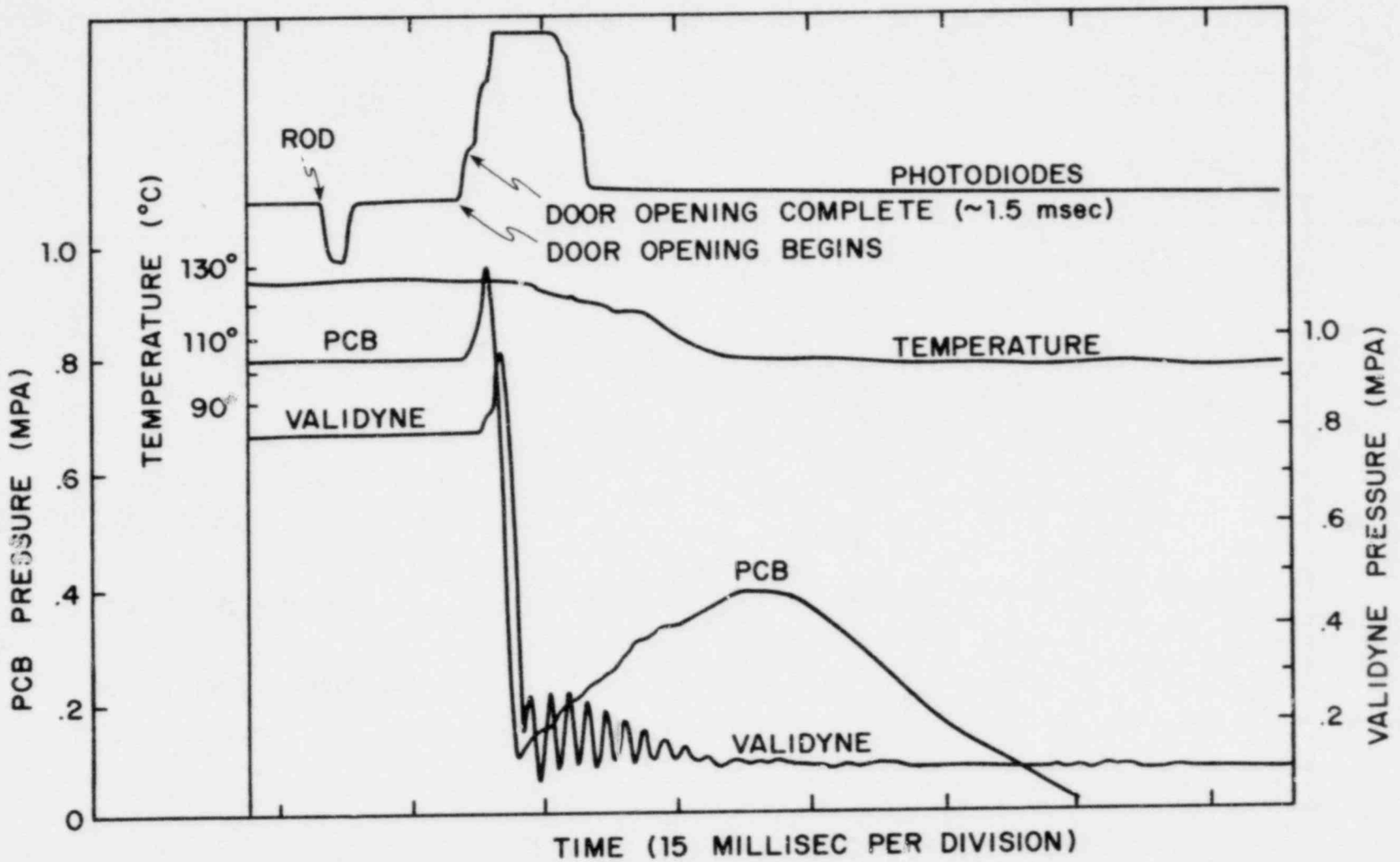

Figure 3.10. Pressure, temperature and timing data from Test F-5 (signals are not aligned on time scale).

Blowdown patterns from collectors placed close to the chamber opening indicate that complete droplet fragmentation and dispersion do not occur immediately upon expulsion from the chamber. Droplet collection must therefore be performed further from the chamber in future tests if final particle size distributions are desired. Both the rotating wheel and stationary collector paper may be used with this intent. Various types of blotter paper are being evaluated for such long-range collection. In addition, the camera is available for size measurement, and a backdrop with divisions for size reference can be easily assembled. The effectiveness of these methods for obtaining an accurate size distribution remains to be seen, however.

Particle Size Measurement by Activation Analysis

Preliminary results for a method to measure particle sizes by neutron activation analysis were obtained[3]. A solute that could by activated by neutron irradiation was dissolved in a solution. This solution was then sprayed on blotter paper by an atomizer, and a correlation between spot size left on the paper and original drop size was developed.

Among several potential solute candidates, $Co\ Cl_2 \cdot 6(H_2O)$ and $Mn\ Cl_2 \cdot 4(H_2O)$ and several silver complexes were first examined on the basis of solubility, coloring and visibility, and usefulness in neutron activation analysis.

The $Co\ Cl_2 \cdot H_2O$ solute was finally selected. The surface tension of a saturated solution was measured to be ~1.2 times that of water. The viscosity was measured to be 1.6 times that of water. These values were judged to be acceptable.

$Co\ Cl_2 \cdot 6\ (H_2O)$ creates a deep purple solution in water which changes to right blue when sprayed on blotter paper and heated. Before heating, the $Co\ Cl_2 \cdot 6\ (H_2O)$ drops on the paper absorbed so much water that they were not sufficiently visible. By heating the paper, however, the excess water was driven off and the drops turned back to a visible blue color that could be photographed and magnified.

It was postulated that the spherical droplet changed roughly in shape to a right circular cylinder when it impinged on the blotter paper. This led to the following prediction of a correlation of drop size with spot diameter on the blotter paper:

$$r_{drop} = C(r_{spot})^{2/3}$$

Experimental measurements by activation analysis led to an approximate correlation with $(r_{spot})^{2/3}$, with C = 1.42. Although the spots were not actually circular, their measured area was approximated by a circle of equal area.

Results for drop radius (r_{drop}) versus spot radius (r_{spot}) are shown in Fig. 3.11. Note that the range of particle sizes measured from this atomizer calibration experiment was 35 μm to 100 μm.

Problems are still encountered with the method, especially in the accuracy of determining the actual spot size on the blotter paper. Work on the technique is continuing.

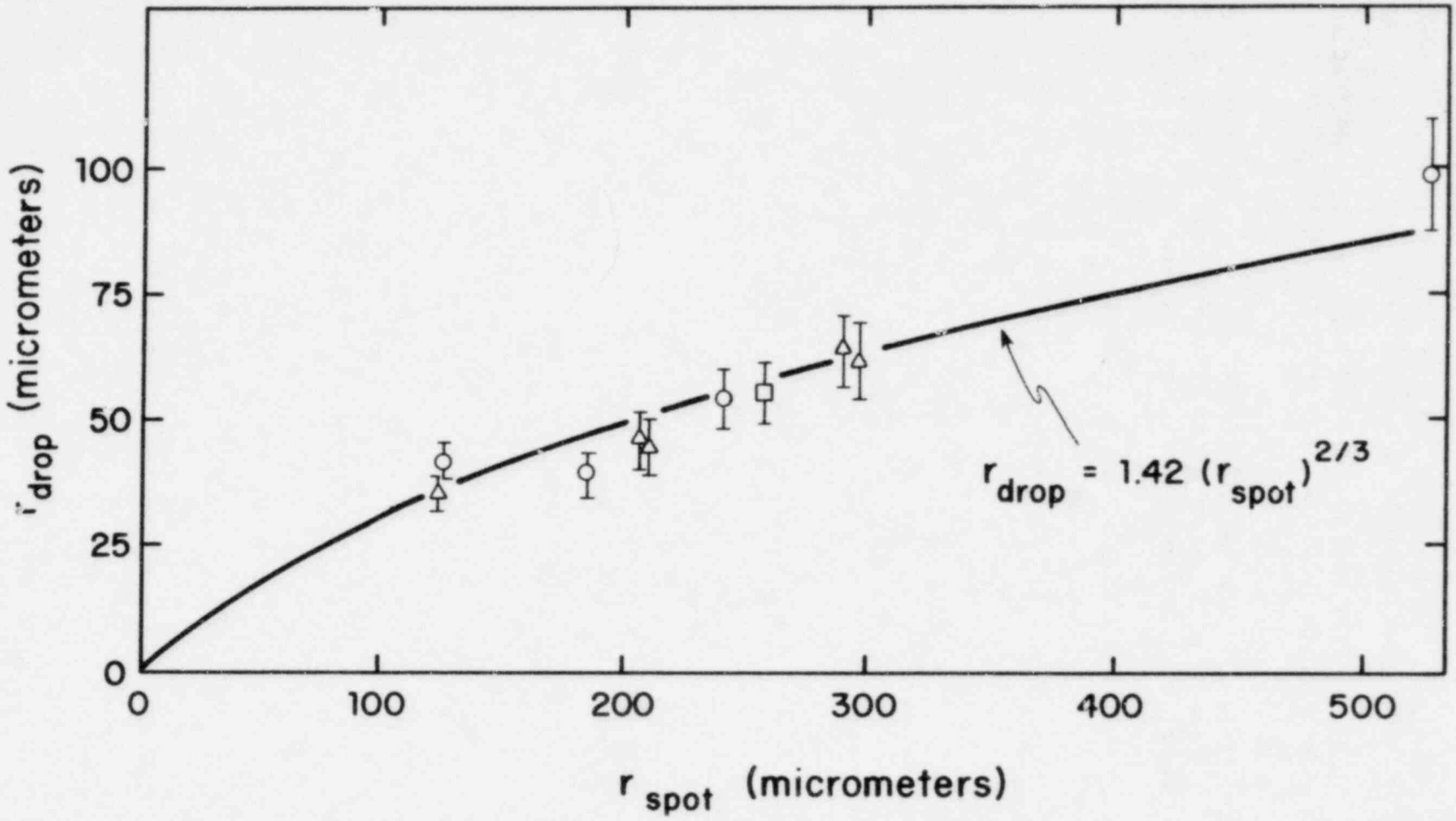

Figure 3.11. Drop radius (r_{drop}) versus spot radius (r_{spot}) on blotter paper.

REFERENCES

1. Brown, R., "Sprays Formed by Flashing Liquid Jets;" Ph.D. dissertation, University of Michigan, Ann Arbor (1961).

2. Gold, M.; "Collecting Empirical Data for Flashing Fragmentation;" undergraduate thesis, unpublished, University of Virginia, Charlottesville (1980).

3. Stiffler, S.; "A Technique for Determining Aerosol Particle Size Distributions Utilizing Activation Analysis;" undergraduate thesis, unpublished, University of Virginia, Charlottesville, (1980).

4. ACCELERATION-INDUCED FRAGMENTATION OF LIQUID DROPS

M. Pilch and C. A. Erdman

4.1. Introduction

The work presented in this section is presented in greater detail, along with related work, in a doctoral dissertation[1] currently in preparation. That dissertation provides a comprehensive literature review of previous work in the field of hydrodynamic or acceleration-induced fragmentation of liquid drops, with emphasis on collection and analysis of breakup time data and particle size data. Previous modeling efforts are also critically discussed.

One significan product of the literature review was the collection of all available breakup time data. The upper curve in Figure 4.1 is the current beat estimate of total breakup time as a function of Weber number based on that data. Times for primary breakup and initiation of breakup are also shown. Indicated on the figure are the approximate Weber number ranges for various breakup modes. References to the shape of this curve and to the different modes of breakup will appear throughout this section.

THe direction of the work discussed in this section has shifted from its original goal[2] of producing a computer model to predict fragment size distributions resulting from drop breakup in a general time-and-space-dependent flow field. That original goal was formulated on the assumption that acceptable models were already in existence to describe the several types or modes of acceleration-induced fragmentation. This assumption proved to be unfounded, and emphasis shifted toward the

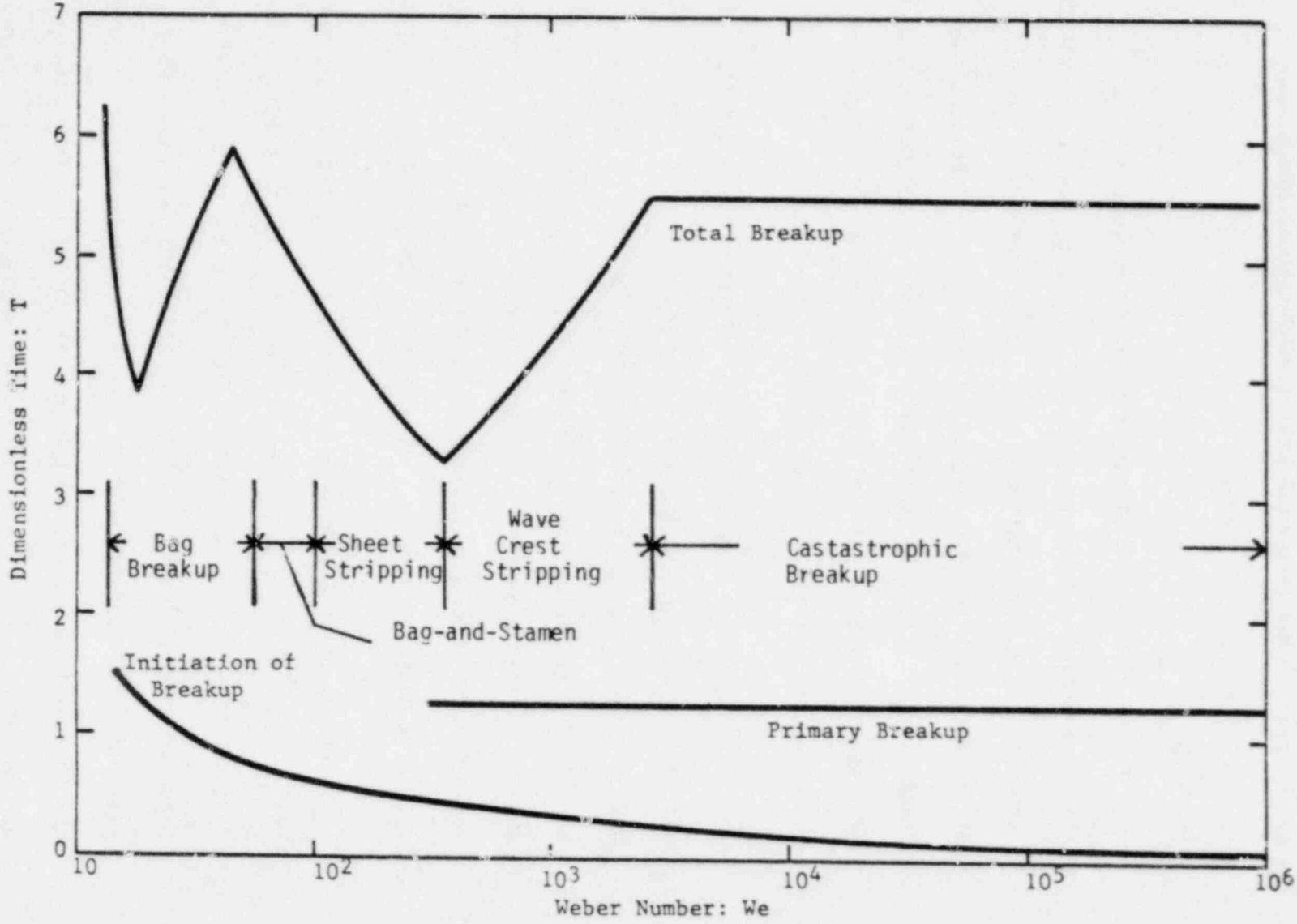

Figure 4.1. Breakup times, gas-liquid systems.

development of models for the various breakup modes, e.g. bag breakup and catastrophic breakup.

A detailed bag breakup model was reported last year.[3] That model was the first to address all four phases of bag breakup: intial deformation, bag formation, bag disintegration, and rim breakup. This detailed modeling of the bag process permits prediction of stagewise breakup times as well as total breakup times and fragment size distributions which are consistent with experiment data.

No further discussion of the bag breakup model or the data compilation and analysis will be given here. In the subsections that follow three topics will be addressed: rejection of previous stripping and Rayleigh-Taylor models for droplet breakup, dominance of Rayleigh-Taylor phenomena in all breakup modes, and a modified maximum stable diameter concept for application to drag-induced fragmentation problems. It will be assumed that the reader is familiar with the basic modes of hydrodynamic fragmentation. References 2 and 4 can provide additional background.

4.2. Previous Stripping and Rayleigh-Taylor Models

Sheet stripping and catastrophic breakup modes have in the past been modeled in rather simplistic ways. On close examination the simple models are found to be inadequate.

Stripping

Classic boundary layer stripping models assume that a viscous boundary layer is pulled off the drop at its periphery, forming a sheet which disintegrates in the wake of the drop. This process continues until the residual drop mass is reduced to zero.

Models such as that of Ranger[5] typically include (1) determination of velocity profiles in the drop and surrounding liquid, and (2) calculation of mass stripping rates based on the velocity profiles. Breakup times (i.e. time to reduce drop mass to zero) can in turn be calculated from the mass removal rates. However, the dimensionless breakup time predicted in this manner using classic boundary layer stripping theory is proportional to the positive one-fourth power of the Weber number (i.e. $We^{1/4}$) while experiment data on total breakup times for sheet stripping show the dimensionless breakup time varying with the negative one-fourth power of the Weber number ($We^{1/4}$). Moreover, predicted breakup times are much longer than the experiment observed breakup times for sheet stripping.

Classic models also do not provide satisfactory estimate of fragment sizes. The standard approach equates fragment sizes to the drop boundary layer thickness at the drop periphery. This suggests that high viscosity liquid droplets would produce larger fragments than would low viscosity liquids in the same flow field. This is directly contradicted by experiment. Also, the Weber number dependence of drop boundary layer thickness is much weaker than the observed dependence of fragment size on the Weber number.

Other objections to use of classic boundary larger stripping theories can be raised. For example, large amplitude waves are observed on the windward side of fragmented drops undergoing sheet stripping. It is difficult to argue for the existence of a laminar boundary layer in the drop under such circumstances.

The modified stripping models which are based on Kelvin-Helmhaltz phenomena avoid some of the problems associated with classic boundary layer stripping models, but again fail to predict the proper Weber number

dependence of fragment size. Also, shear layers such as those existing in real flow situations tend to stabilize the drop/gas interface with regard to Kelvin-Helmholtz disturbances.

In summary, classic boundary layer theories or modified theories based on Kelvin-Helmholtz instabilities do not adequately explain sheet stripping.

Catastrophic Breakup

Catastrophic breakup has been correctly interpreted in the past as being closely related to the classic Rayleigh-Taylor instability. References 6 and 7 provide examples of modeling efforts which explain catastrophic breakup in terms of Rayleigh-Taylor instability.

Small disturbances on the windward side of a drop are subject to Rayleigh-Taylor instability. The classic planar analysis provides good estimates of fastest growing wavelengths and growth rates for very small amplitude disturbances. The theory predicts dimensionless growth rates proportional to the positive one-forth power of the Weber number (i.e. $We^{1/4}$); breakup time data suggest that the dimensionless breakup time, $\bar{T}$, is proportional to $We^{-1/4}$. This has led many observers (e.g. Ref. 6) to conclude that catastrophic breakup is the direct result of the fastest growing Rayleigh-Taylor wave penetrating the drop. There are several serious objections to such a conclusion:

(1) The wave amplitudes necessary to penatrate the drop are much too large for the classic, small-wave-amplitude Rayleigh-Taylor theory to apply.

(2) If objection (1) is ignored and breakup times are calculated based on penetration times of fastest growing Rayleigh-Taylor waves, the corresponding initial amplitude, η_o, of the surface disturbance is found to be

unreasonably small. For an original drop diameter; D_o, the values of η_o/Do required to make classic Rayleigh-Taylor theory consistent with experiment breakup times range from 10^{-4} to 10^{-23}, depending on assumed drop coefficients and on whether experiment data is interpreted as representing primary or total breakup time. A best estimate for η_o/D_o consistent with average measured drag coefficients and assuming the data represents total breakup (several stages) is 3.1×10^{-8}. For D_o = 1mm, η_o would be 3.1×10^{-11}m or 0.31 Angstrom.

(3) Classic Rayleigh-Taylor theory identifies a specific wavelength, λ^*, which is characteristic of the fastest growing disturbances. The drop should be penetrated by waves of this wavelength, λ^* however, the observed wavelengths of penetrating waves (e.g. Ref. 8) can be twenty or more times greater than λ^*.

The three arguments give above demonstrate the inappropriateness of utilizing classic Rayleigh-Taylor theory to explain catastrophic breakup.

4.3 Dominance of Rayleigh-Taylor Phenomena

Although classic small amplitude Rayleigh-Taylor instability theory cannot by itself model catastrophic breakup, arguments can and will be presented below to the effect that Rayleigh-Taylor phenomena dominate droplet breakup over the full range of Weber numbers.

Low Weber Number Range

THe Rayleigh-Taylor instability offers insight into the basic phenomena of bag breakup and bag-and-stamen breakup. Consider a drop of original diameter D_o which is deformed to the maximum diameter observed in experiments[9,10], 2.3 Do. This diameter is just large enough to allow one Rayleigh-Taylor wave at low Weber number (12 to 14) to fit on the windward surface of the drop. The initial growth of the wave and the accompanying thinning of the

drop in the crest region of the wave on the leeward surface of the drop lead to bag formation.

Similarly, at a Weber number of approximately 50, two Rayleigh-Taylor waves can fit on the drop at maximum deformation. Assuming concentric waves on the surface, the geometry of the bag-and-stamen breakup mode is suggested.

Stripping

In the Weber number range where sheet stripping and wave crest stripping are observed (100 to 3000), fragment sizes from breakup can be correlated with the fastest growing Rayleigh-Taylor wavelength, λ^*. This is demonstrated in Figures 4.2 and 4.3. The maximum observed diameter, the mass median diameter, and the number median diameter (not illustrated) are all proportional to λ^*, i.e. they are proportional to $We^{-1/2}$.

Further arguments for Rayleigh-Taylor dominance can be generated through Rayleigh-Taylor modeling of the wave crest stripping mode of breakup. Reference 1 presents such a model for calculating mass removal rates for wave crest stripping. That model assumes the surface waves are the fastest growing Rayleigh-Taylor waves. The waves are further assumed to lose mass by crest stripping at exactly the same rate that they gain mass by growing in accordance with classic Rayleigh-Taylor theory.

The calculated mass removal rate is used to determine the total dimensionless breakup time $\overline{T}$ (i.e. when residual drop mass goes to zero). The model predits $\overline{T} \propto We^{1/4}$ in agreement with experiment data for the wave crest stripping region.

Catastrophic Breakup

Several major features of catastrophic breakup can be explained as Rayleigh-Taylor phenomena; however, a two-stage model is necessary. The

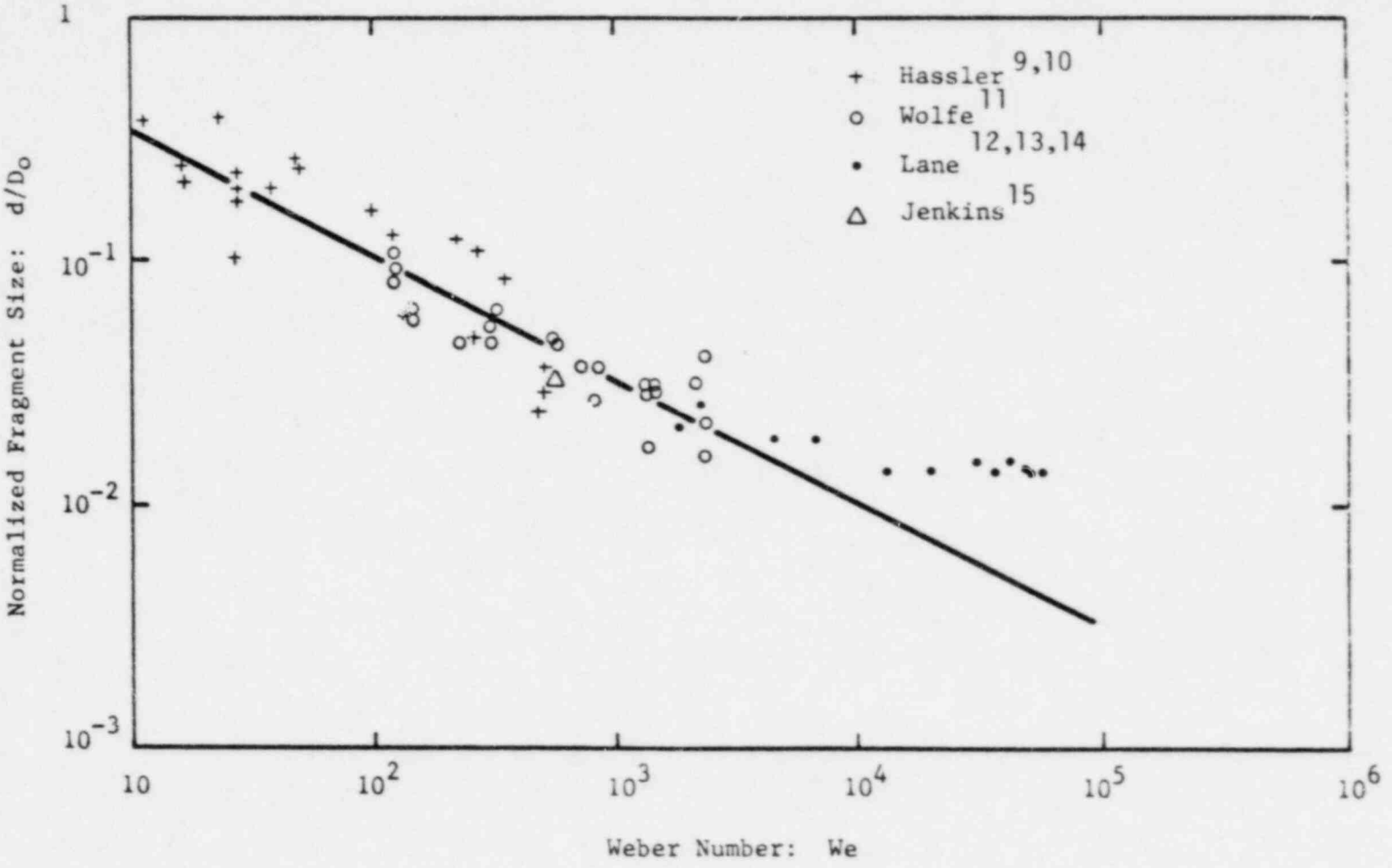

Figure 4.2 Maximum Observed Fragment Sizes.

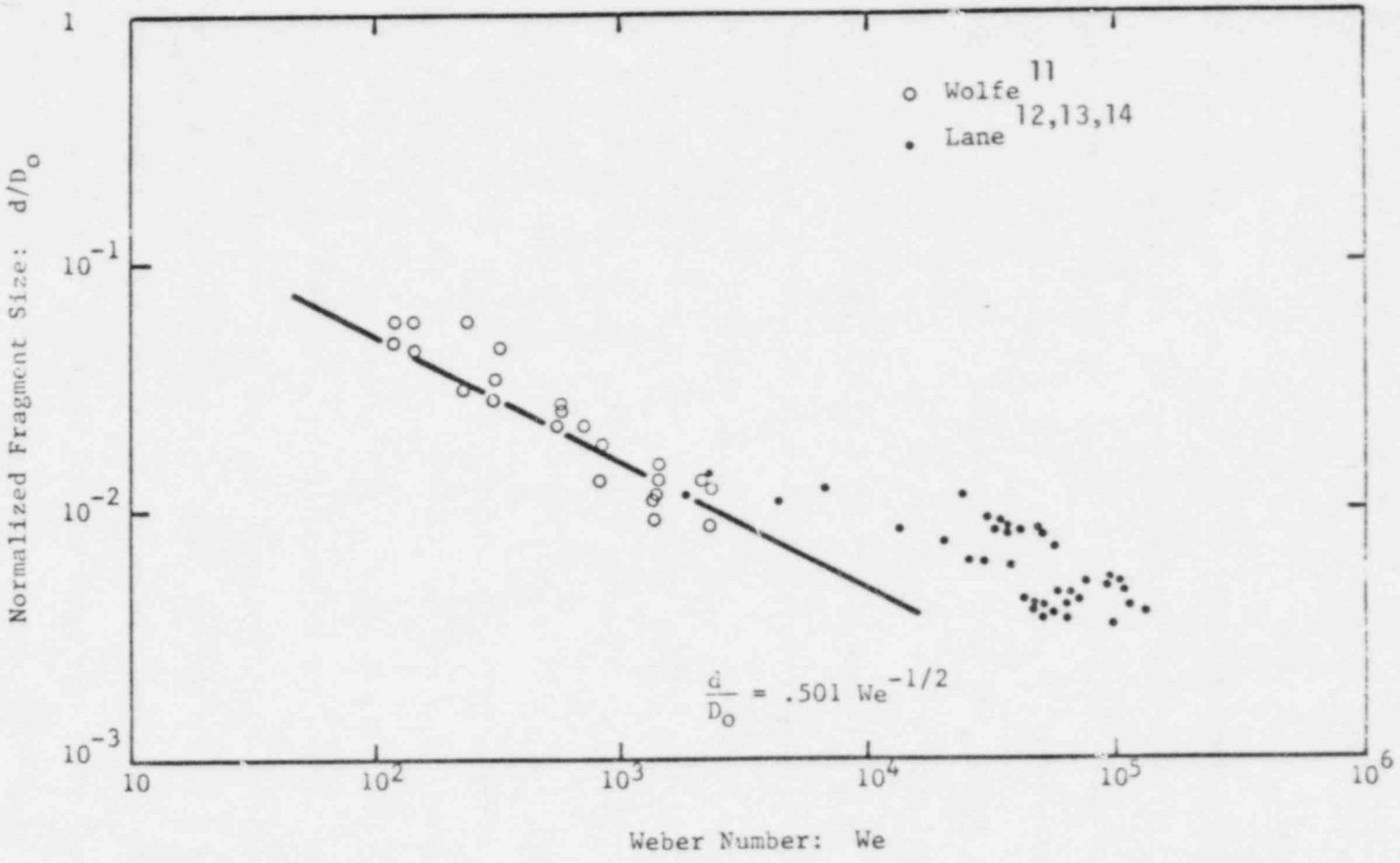

Figure 4.3 Mass Median Fragment Sizes.

first stage is adequately described by the classic Rayleigh-Taylor theory for small amplitude waves. This stage is referred to as the linear stage or phase because of the linearigation of the governing hydrodynamics equations in the small wave theory. In this linear stage waves grow exponentially in time.

The exponential growth of waves in the linear stage means that waves very rapidly enter the nonlinear stage of Rayleigh-Taylor instability. The nonlinear stage is characterized by a constant pentration velocity for a given wavelength. Transition between linear and nonlinear stages occurs when the growth rate in the linear stage attains the constant growth rate associated with the nonlinear stage.

During the linear stage, small wavelength waves grow more rapidly than long wavelength waves; the reverse is true in the nonlinear stage. For a given set of drop and flow field characteristics, there is one wavelength which has a minimum drop pentration time (sum of times spent in linear and nonlinear stages). Disturbances with that wavelength pentrate and fragment the drop.

One crucial aspect of the two stage model is the necessity to predict drop thickness as a function of time. This is done through the use of empirical correlations for drop deformation and mass loss rates.

After calibration of the model to agree with phenomena (number of primary fragments and pentration times) observed from experiments run at a Weber number of 3×10^5, the two stage Rayleigh-Taylor model was applied over the entire range of Weber numbers for which catastrophic breakup occurs. The model predicts primary breakup times and numbers of primary particles which are consistent with the available experiment data.

After independent development of this two stage model, an earlier attempt by Fishburn[16] to develope a two stage Rayleigh-Taylor model was found in the

literature. The Fishburn model, which differs in several critical aspects from the model described above, is presented and critiqued in detail in Ref. 1.

The arguments given above in this subsection constitute the primary basis for the claim that Rayleigh-Taylor phenomena dominate drop breakup over the entire Weber number range. This clain represents a departure from the previous consensus that Rayleigh-Taylor phenomena are only important in catastrophic breakup.

4.4 Maximum Stable Diameter

Drop breakup is a multistage process in which fragments from the original drop will themselves undergo breakup if their Weber number exceeds the critical Weber number. When the multistage breakup process is complete, all the particles will exhibit a diameter smaller than a critical diameter which is commonly referred to as the maximum stable diameter. A fragment for which the Weber number is just less than the critical Weber number at the time of its creation will have a diameter equal to the maximum stable diameter. Detailed knowledge about breakup processes is not required in order to estimate the maximum stable diameter.

Fragments can acquire Weber numbers less than the critical Weber number by two processes: breakup and drop acceleration. Each stage of breakup produces increasingly smaller fragments with correspondingly smaller Weber numbers. Acceleration during breakup ensures that the relative velocity between the flow field and a given fragment at the time of the fragment's creation is less than the relative velocity existing for the original drop when it is first exposed to the flow field.

Conventional Model

The conventional approach to estimating the maximum stable diameter is to neglect drop acceleration. Fragments are assumed to acquire Weber numbers less than the critical Weber number only as a result of the multistage breakup process which produces increasingly smaller fragments at each stage of breakup.

A fragment for which the Weber number is just less than the critical Weber number will have a size equal to the maximum stable diameter defined by the following equations:

$$\frac{\rho V^2 d}{\sigma} = We_c = \frac{\rho V^2 D_o}{\sigma} = \frac{\rho V^2 D_o}{\sigma} \frac{d}{D_o} \tag{4.1}$$

$$\frac{d}{D_o} = \frac{We_c}{We} \tag{4.2}$$

Where d is the size of the largest stable fragments and D_o is the initial drop size.

Equation 4.2 predicts that the maximum stable diameter is inversely proportional to the initial Weber Number; however, maximum observed fragment sizes (Figure 4.4) do not confirm this. Figure 4.4 shows that observed fragment sizes can be as much as 70 times greater than the predicted maximum stable diameter. The failure of the conventional model is due to the neglect of drop acceleration effects.

Modified Model

Drop breakup is again considered complete when the drop and all its fragments are no longer subject to further breakup. Now, however, drop acceleration during breakup is considered. A fragment whose size equals

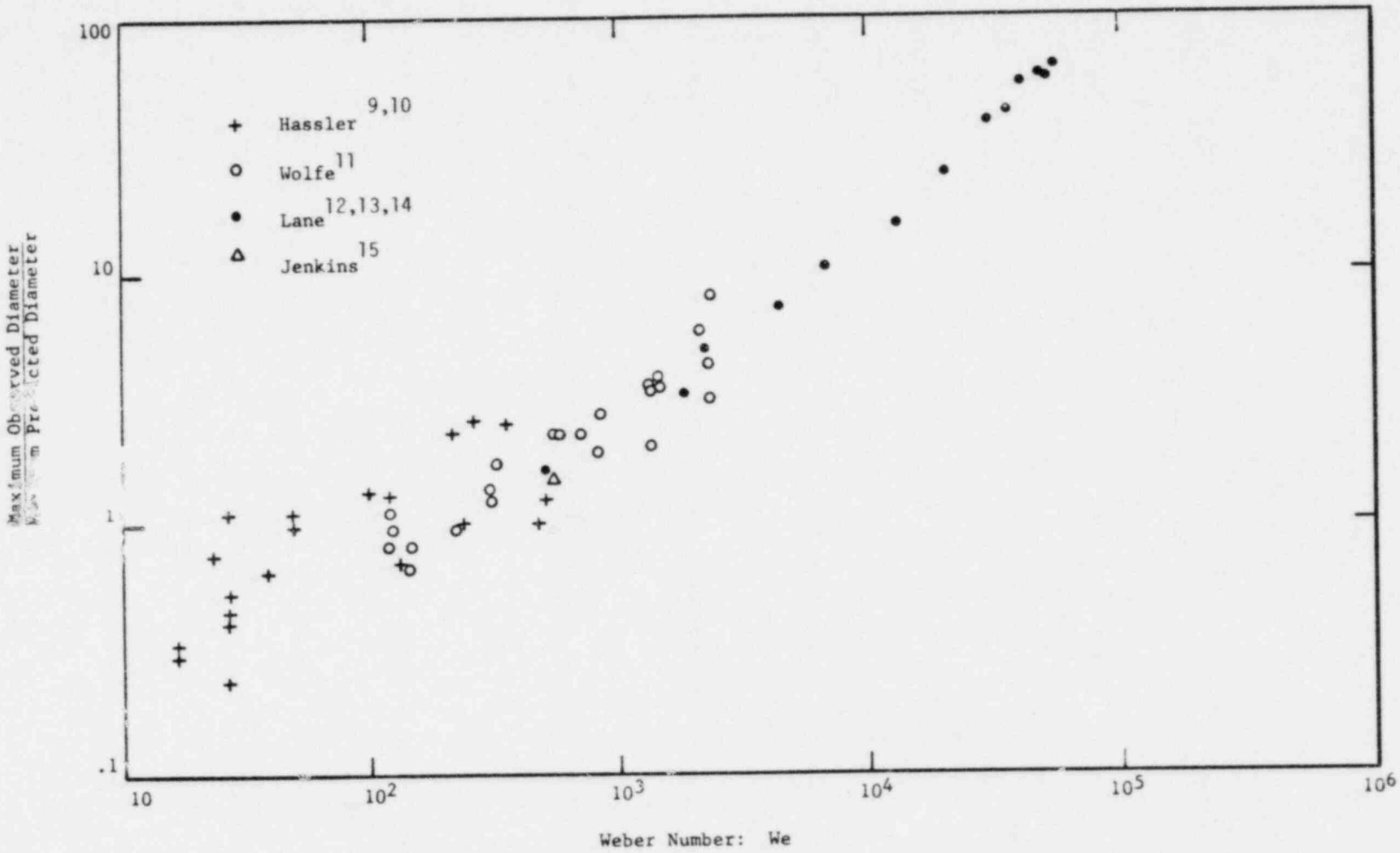

Figure 4.4. Test of conventional maximum stable diameter model.

the maximum stable diameter as defined by equations 4.3 and 4.4 below will have a Weber number just less than the critical Weber number at the time when all breakup processes cease.

$$\frac{\rho(V-V_d)^2 d}{\sigma} = We_c = \frac{\rho V^2 D_o}{\sigma}\left(1 - \frac{V_d}{V}\right)^2 \frac{d}{D_o} \tag{4.3}$$

$$\frac{d}{D_o} = \frac{We_c}{We}\left(1 - \frac{V_d}{V}\right)^{-2} \tag{4.4}$$

where V is the free steam velocity, and V_d is the drop velocity at the time that all breakup processes cease.

To complete the model, empirical correlations for total breakup time and drop velocity as a function of time were developed based on all available experiment data. Those correlations are discussed in detail in Ref. 1.

Predictions of the modified maximum stable diameter model are compared in Fig. 4.5 with experiment observed fragment sizes. The ratio of observed to predicted fragment sizes is seen to be near unity for a wide range of Weber numbers. The deviation from unity in the range $200 \leq We \leq 2000$ is likely due to uncertainties associated with the drop velocity correlation in this region. Note also that predicted fragment sizes exceed measured fragment sizes when the Weber number is less than about 300. This is not a contradiction of the theory, because the maximum stable diameter concept merely places an upper limit on the largest possible fragment size. The theory does not preclude the possibility that all primary fragments are already too small upon creation to be susceptible

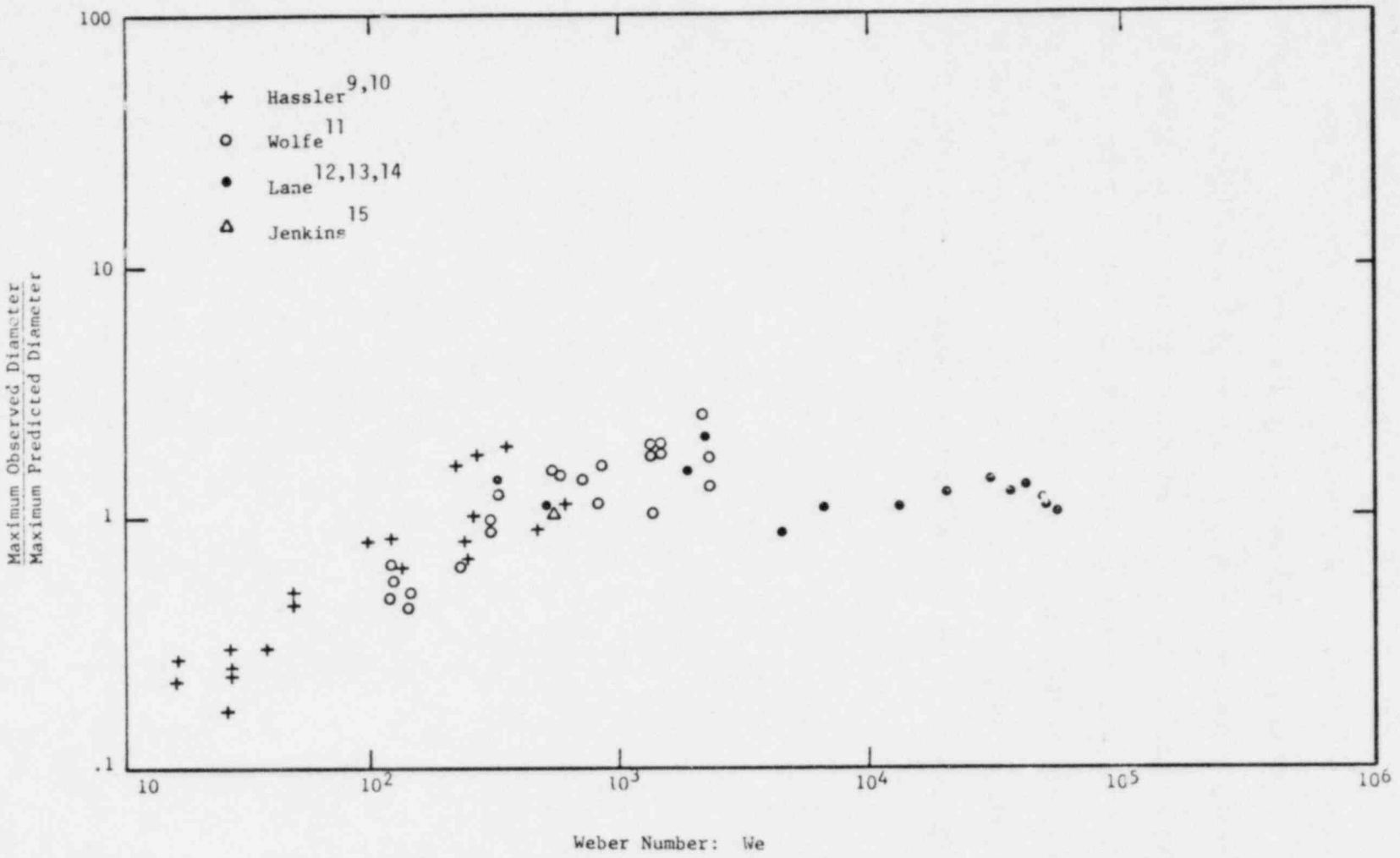

Figure 4.5. Test of modified maximum stable diameter model

to further breakup. This is consistent with the observation that secondary breakup is not usually observed for initial Weber numbers less than 300.

In summary, the maximum stable diameter concept is a useful tool for estimating the largest stable fragment sizes resulting from drop breakup, provided the initial Weber number exceeds about 300. It was pointed out in Ref. 1 that the ratio of maximum to mass median fragment sizes is 2.04 regardless of Weber number. This empirical observation, in conjunction with the maximum stable diameter concept, permits prediction of mass median fragment sizes for any Weber number exceeding 300.

REFERENCES

1. M. Pilch, Acceleration-Induced Fragmentation of Liquid Drops, Ph. D. Dissertation, University of Virginia, Charlottesville, VA (1980).

2. C. A. Erdman, A. B. Reynolds, D. R. Bradley, K. Chen, M. Pilch, "Bubble Behavior in LMFBR Core Disruptive Accidents Annual Report, October 1977-September 1978, "NUREG/CR-0504, University of Virginia (March 1979).*

3. M. Pilch and C. A. Erdman, Particle Size Distributions from Multiple Hydrodynamic Fragmentation Events, Proceeding of the International Meeting on Fast Reactor Safety Technology, Seattle, Washington, 1, 239-248, (Aug. 19-23, 1979).

4. C. A. Erdman, A. B. Reynolds, M. Pilch, M. F. Kennedy, P. L. Garner, A. E. Walter, " Bubble Behavior in LMFBR Core Disruptive Accidents, Annual Report, July 1, 1976-September 30, 1977, "NUREG/CR-0002, UVa/529106/NE77/103 (February 1978).**

5. A. A. Ranger and J. A. Nicholls, "Aerodynamic Shattering of Liquid Drops", AIAA J., 7(2), 285-290, (Feb. 1969).

6. W. G. Reinecks, and G. D. Waldman, An Investigation of Water Drop Disintegration in the Region Behing Strong Shock Waves, Third International Conference on Rain Erosion and Related Phenomena, Hampshire, England, (Aug. 11-13, 1970).

7. P. G. Simpkins and E. L. Bales "Water-Drop Response to Sudden Accelerations", J. Fluid Mech., 55(4), 629-639, (1972).

8. W. G. Reinecks and G. D. Waldman, Shock Layer Shattering of Cloud Drops in Reentry Flight, AIAA Paper 75-152, AIAA 13th Aerospace Sciences Meeting, Pasadera, Calif. (Jan. 20-22, 1975).

9. G. Hassler, Breakup of Large Water Drops Under the Influence of Aerodynamic Forces in a Steady Stream of Steam at Subsonic Velocities, Third International Conference on Rain Erosion and Related Phenomena, Hampshire, England, (Aug. 11-13, 1970).

10. G. Hassler, Untersuchungen zur Verfomung and Auflosung von Wassertropfen Durch Aerodynamische Drafte im Stationaren Luft-und Wesserstrom Bei Unterschalgeschwindigkeit, Ph.D. Dissertation, Universitat Karlsruhe, (1971).

11. H. E. Wolfe, and W. H. Anderson, Kinetics, Mechanism, and Resultant Droplet Sizes of the Aerodynamic Breakup of Liquid Drops, AGCD Rept. No. 0395-04 (18) SP, (April 1964).

12. W. R. Lane, W. C. Prewett, and J. Edwards, Some Experiments on the Shatter of Drops by Transient Blasts of Air, Porton (England) Technical Paper No. 115, Serial 15, (May 1949).

13. W. R. Lane, "Shattering of Drops in Streams of Air," Ind. Eng. Chem., 43(6) 1312-1317, (1951).

14. W. R. Lane and R. G. Dorman, Furhter Experiments on the Shatter of Drops by a Supersonic Air Blast, Porton (England) Technical Paper No. 279, (March 1952).

15. D. C. Jenkins, and J. D. booker, The Time Required for High Speed Airstremas to Disintegrate Water Drops, N66-22790, (May 1964): Also, Ministry of Aviation (GB), Aero Res. Council Current Papers, CP No. 827, UDC NO. 532.6: 533.6.011, (May 1964).

16. B. D. Fishburn, "Boundary Layer Stripping of Liquid Drops Fragmented by Taylor Instability," Acta Astronautica, 1, 1267-1284, (1974).

*Available for purchase from the NRC/GPO Sales Program, U.S. Nuclear Regulatory Commission, Washington, DC 20555, and/or the National Technical Information Service, Springfield, VA 22161.

**Available for purchase from the National Technical Information Service, Springfield, VA 22161.

5. PARTICLE SIZE DISTRIBUTION FROM CONDENSATION IN ORNL CDV TESTS IN ARGON

K. Chen and A.B. Reynolds

5.1 Introduction

The release of radioactive aerosol particles as a result of an energy excursion during a Hypothetical Core Disruptive Accident (HCDA) in a Liquid Metal Fast Breeder Reactor (LMFBR) poses a potential radiological hazard. Primary aerosol particles in the submicrometre size range are of particular concern because they can remain airborne for a long period of time after the HCDA, even after agglomerating into groups of primary particles.

Out-of-pile experiments have been developed at the Oak Ridge National Laboratory (ORNL) to study LMFBR fuel (UO_2) vaporization and transport in an HCDA-type energy excursion. In these experiments fuel is vaporized by the rapid deposition of electrical energy through the discharge of capacitors. The technique, called Capacitor Discharge Vaporization (CDV), was developed by vaporizing fuel in an argon environment. UO_2 particles were produced by both condensation of vapor and fragmentation of liquid. The distribution of the size of the primary UO_2 particles that remained airborne after several minutes was measured, and observed particle diameters varied from 0.004 to 0.1 μm.[1]

The purpose of the research reported here was to develop a model to calculate the measured particle-size distribution. The research is part of the NRC Aerosol Release and Transport Program and has been carried out in close corporation with ORNL.

This research is a continuation of work initiated at the University of Virginia by Kennedy, Erdman, and Reynolds.[2,3,4] In a model which they developed for homogeneous nucleation and condensation growth (referred to hereafter as the Kennedy model), the calculated particle sizes were in the same range as the measured values. This provided support for the theory that the particles resulted from homogeneous nucleation from the vapor followed by condensation growth.

The slope of the particle-size distribution predicted by Kennedy's model, however, did not agree with the measured distribution. This disagreement may have been due to the source of the supersaturation assumed by Kennedy, et al. In their model, two-phase UO_2 was isentropically expanded to the argon pressure, with the UO_2 liquid and vapor in equilibrium. Cold argon gas was then assumed to mix with the saturated UO_2 vapor causing homogeneous nucleation condensation growth. Mixing of gases is generally a slow process, however, relative to the expansion time of an initially high pressure vapor sphere. The high pressure gas dynamics phenomena of the CDV tests were ignored in Kennedy's model.

It is now believed that the condensation that led to the small range of particles in the CDV tests resulted from supersaturated UO_2 vapor expanding behind the shock wave as the UO_2 vapor compressed the surrounding argon gas. Therefore, the new model described here is based on homogeneous nucleation and condensation growth in the rarefaction wave generated during the UO_2 vapor expansion.

5.2 Description and Results of ORNL CDV Tests

Test Description

The CDV experiments are described in several references, e.g. Ref. 1 and 5. A brief description pertinent to the present model development is provided here.

The fuel capsule shown in Fig. 5.1 is located in a large tank containing argon at atmospheric pressure and ambient temperature. The test sample consists of a 110 mm column of UO_2 pellets of 5 mm diameter, surrounded by UO_2 microspheres (diameter from 0.35-0.50 mm). The pellet/microsphere assembly is enclosed in a quartz tube with ID about 10 mm and OD about 20 mm, which serves as a containment during sample preheat. The surrounding microspheres act as thermal insulation to maintain the quartz tube integrity during the sample preheat and to avoid bypass arcing around the pellet stack during capacitor discharge.

At the start of a test, the UO_2 pellets are preheated to near the UO_2 melting temperature. This reduces the UO_2 electrical resistance from $10^6 \Omega$ at room temperature to $\leq 0.5 \Omega$ in order to achieve the maximum energy deposition rate which characterizes the HCDA-type energy excursion in the fuel. After the preheater is disconnected from the sample, the capacitors are discharged through the pellet stack which are partially vaporized due to rapid energy deposition. Energy deposition rates between 0.4 and 1.2 MW/g have been used, and the energy deposition in the fuel pellets has been calculated to be as high as 3000 J/g.

The high pressure UO_2 vapor generated in the sample causes the rupture of the quartz tube. The fuel then expands into the argon

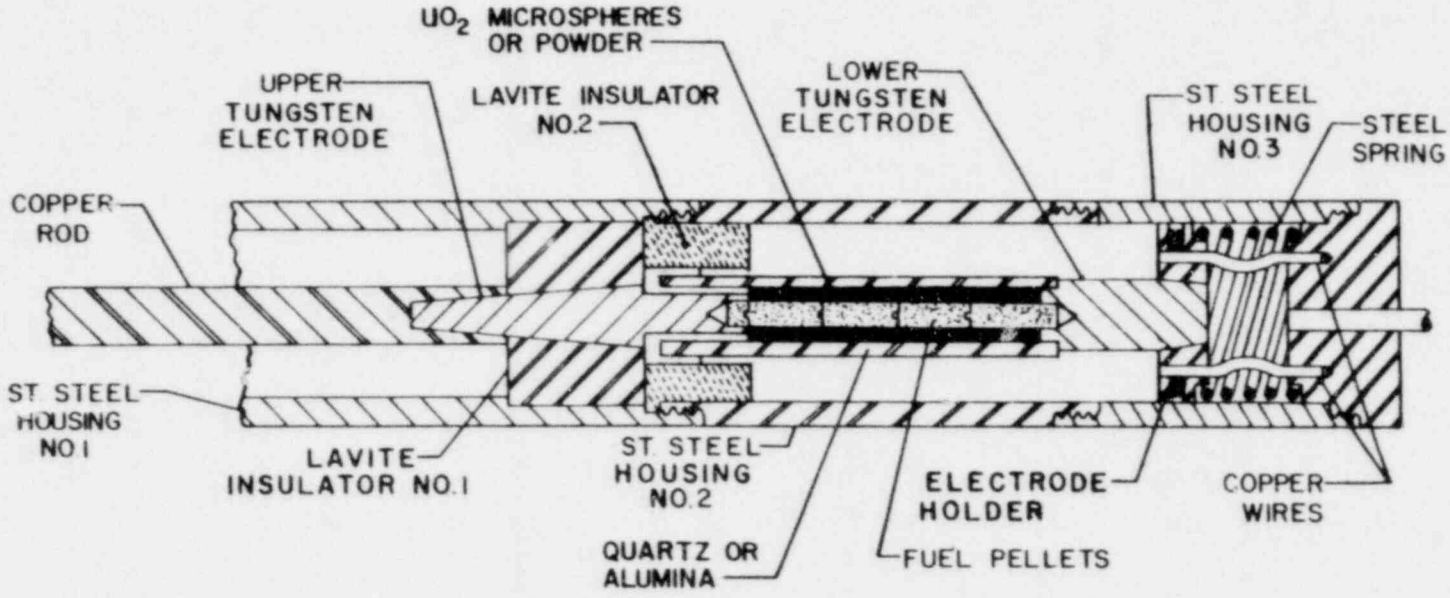

Figure 5.1. Fuel capsule design.

atmosphere, and particles from the condensing vapor and fragmenting liquid are collected. Particle sampling in the argon starts about 2 minutes after the capacitor discharge thus allowing first the precipitation of the larger particles (> 4 μm diameter) formed by fragmentation of liquid. A sequential mass sampler is employed to measure the suspended aerosol mass concentration at a given time after capacitor discharge. Plateout samplers equipped with electron microscope grid precipitators are used. The plateout samplers measure the plateout rate, and the transmission electron photomicrographs of the grid samples are analyzed directly to determine the size-distribution of parimary particles.

Test Results

Sequential frames from a CDV movie, separated in time by 0.1 ms, are shown in Fig. 5.2. It is postulated that, during the early expansion phase shown in the movies, UO_2 vapor expands past the liquid fuel, microspheres, and broken quartz tube, and compresses the surrounding low pressure argon gas. It is believed that the expanding surface observed in the movies is the UO_2 vapor-argon interface.

The size of this expanding surface as a function of time can be estimated from the movies. This has been done for five CDV tests--Numbers 17, 39, 45, 51 and 80. Table 5.1 presents the estimated size of the UO_2 vapor sphere from the CDV movies. The rate of expansion of the sphere can be compared to a gas dynamics analytical model in order to provide a check between theory and experiment; this comparison is provided in Section 5.4.

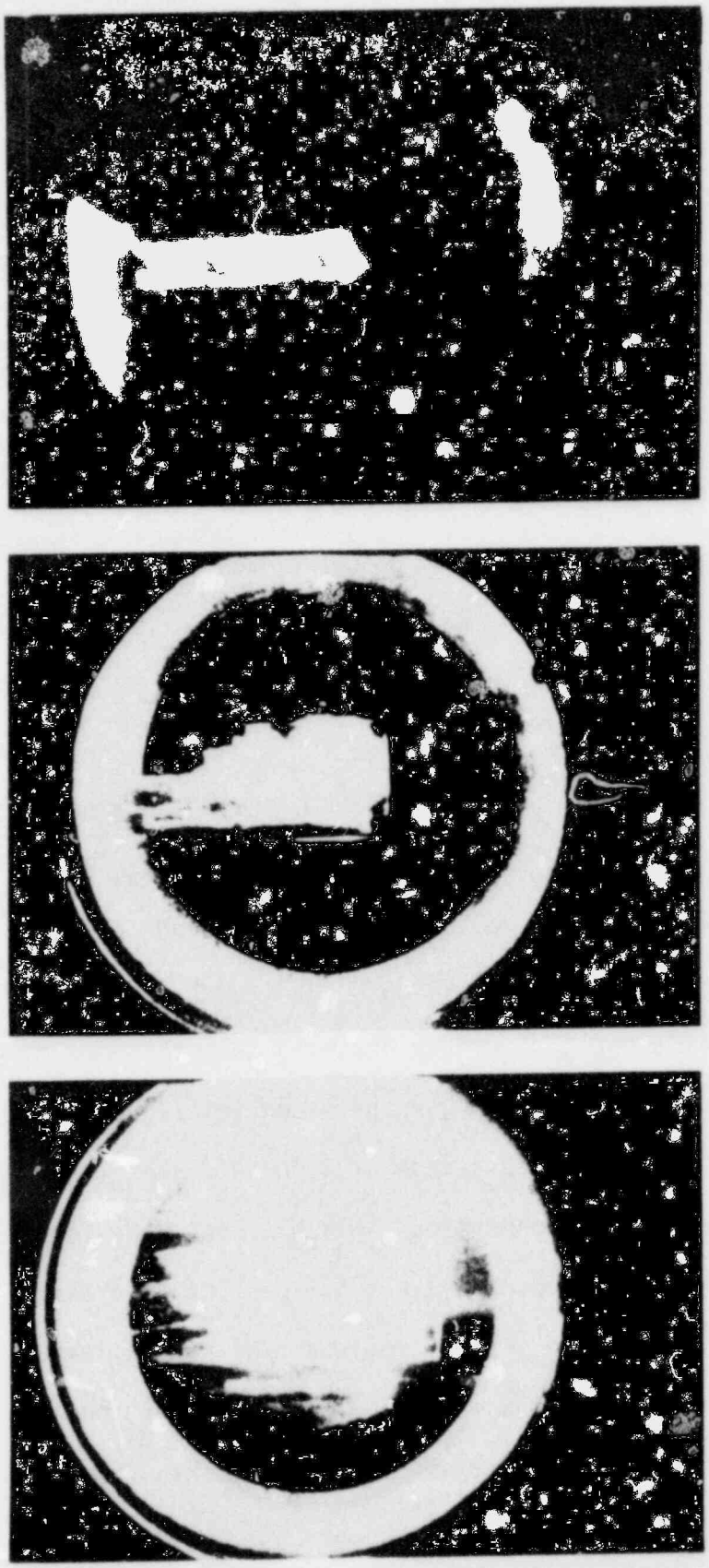

Figure 5.2. Consecutive frames from movies of UO_2 expansion in CDV Test 45. Time between frames is 0.1 ms.

TABLE 5.1

ESTIMATED UO_2 VAPOR SPHERE RADII FROM CDV TESTS

Test No.	Radius (mm) First Frame After Rupture	Second Frame After Rupture	Third Frame After Rupture
17	25.0 ± 2.5	63.0 ± 6.3	– –
39	31.5 ± 3.1	44.0 ± 4.4	52 ± 5.2
45	23.0 ± 2.3	40.0 ± 4.0	– –
51	28.0 ± 2.8	50.5 ± 5.1	– –
80	40.0 ± 4.0	>65.0	– –

Particle-size distribution curves for the five CDV tests 16, 19, 21, 24 and 29 are presented on Figure 5.3. Two samples were taken in tests 16 and 21; hence there are seven curves. The curves are shown on log-probability paper; a log-normal distribution appears as a straight line on this type of graph. Hence the particle distributions appear to be approximately log-normal. Electron photomicrographs of particles from two of the tests are shown on Fig. 5.4.

A log-normal distribution can be characterized by two parameters; the geometric mean diameter, d_g, which represents that diameter for which 50% of the particles are below d_g and 50% are above d_g, and the geometric standard deviation, σ_g, which is the slope of the curve on log-probability paper. Values for d_g and σ_g for the seven curves are listed in Table 5.2.

5.3 Condensation Model

A spherical shock tube type model with homogeneous nucleation and condensation growth was developed to model the CDV tests in an argon environment. This model is based on the nucleation of UO_2 droplets in a rarefaction wave fan behind an expanding UO_2-argon interface.

The model assumes the interpretation and approximations illustrated in Fig. 5.5. The three illustrations in Fig. 5.5(a) represent our interpretation of what is observed in the movies, corresponding to Fig. 5.2. The simulation in Fig. 5.5(b) shows the shock tube configuration assumed for each illustration. The inner sphere contains saturated UO_2 liquid at the average temperature of the fuel test sample at the end of the capacitor discharge. The inner concentric shell consists of broken quartz and UO_2 microspheres. The outer shell contains saturated UO_2 vapor

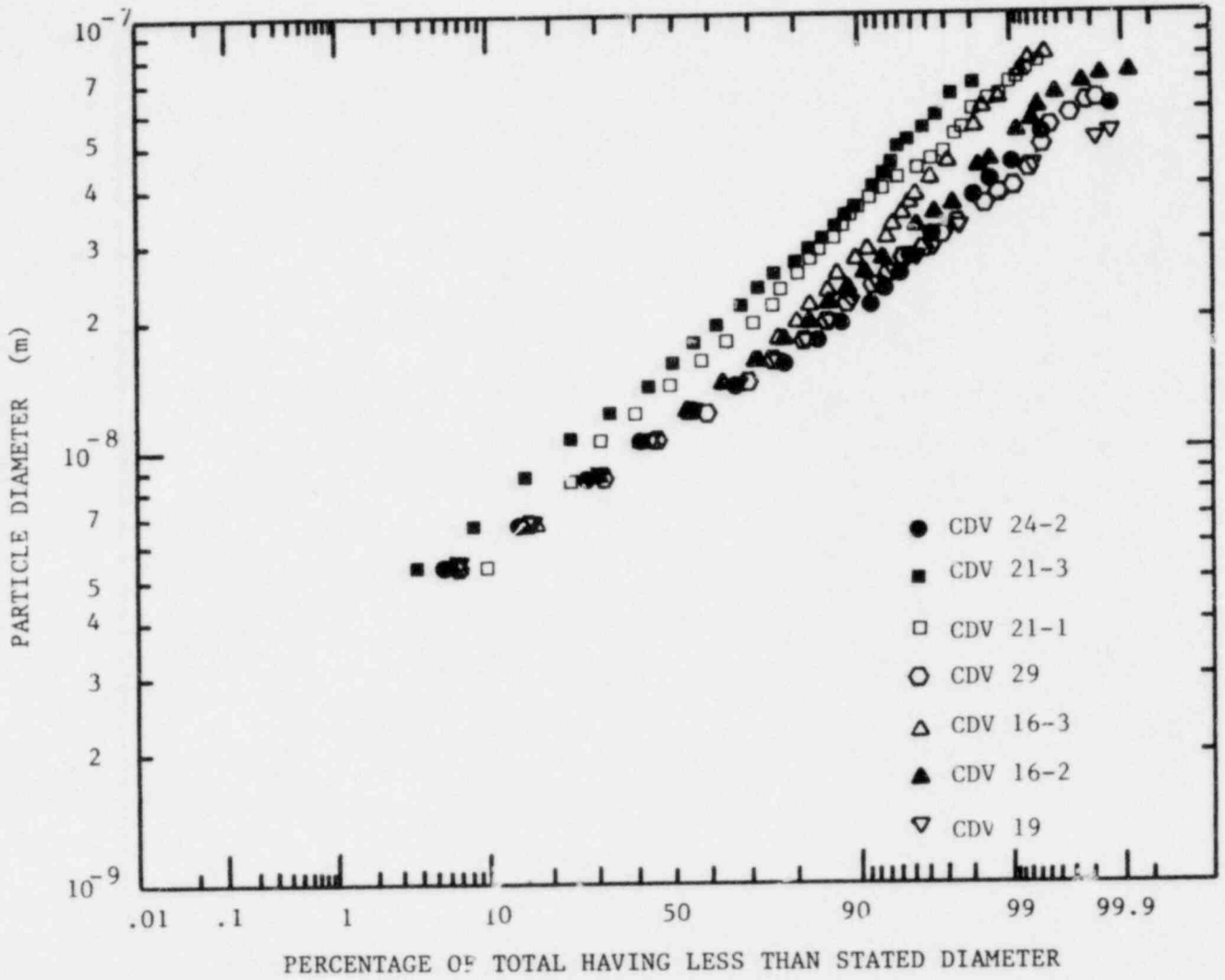

Figure 5.3. Measured particle-size distributions for 5 CDV tests. Two measured distributions are given for Tests 16 and 21.

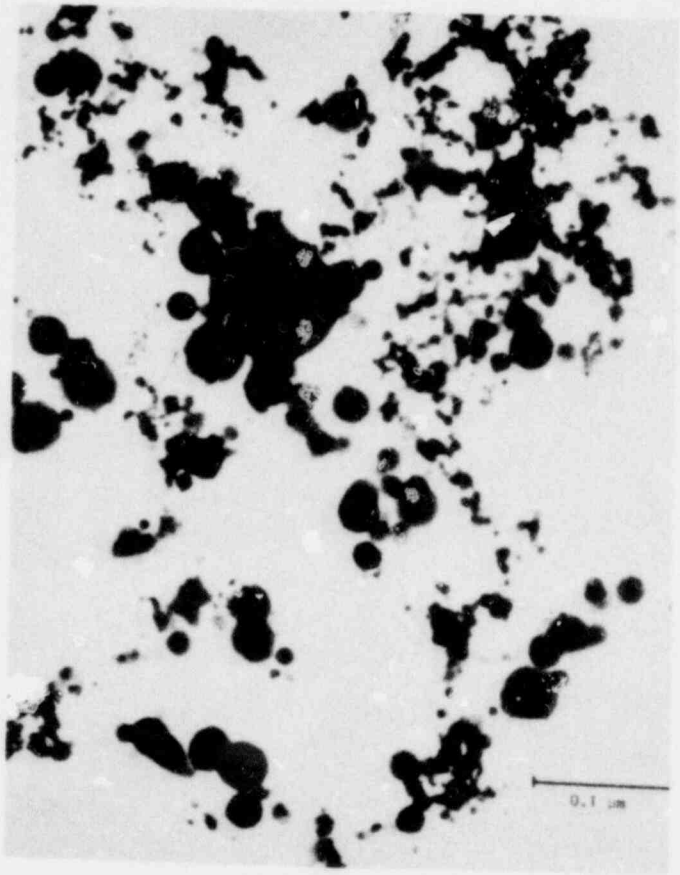

CDV Test 24-2

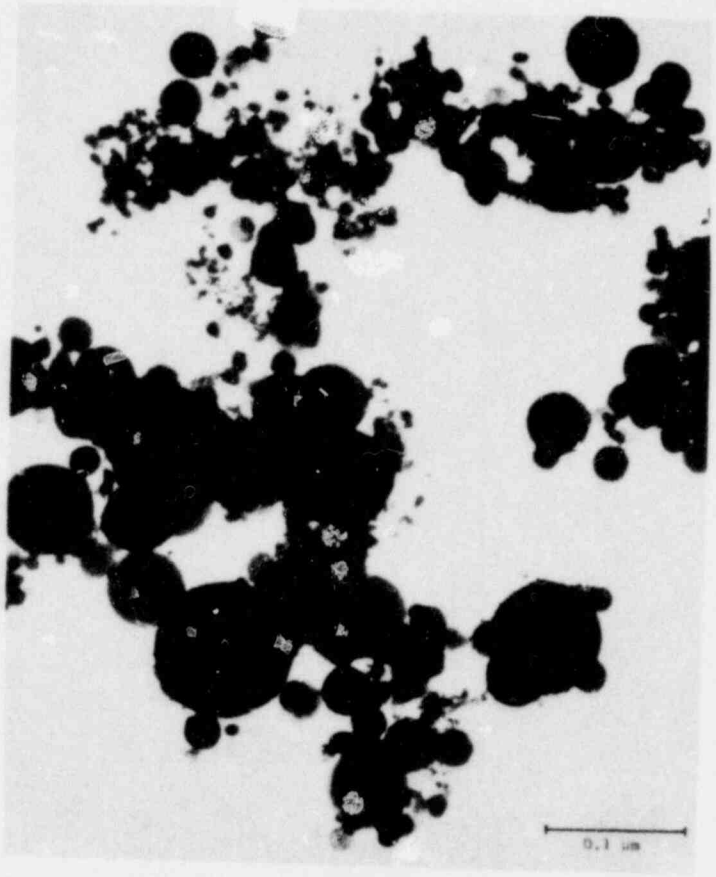

CDV Test 16-3

Figure 5.4. Aerosol collected on electron microscope grids for CDV tests 24-2 and 16-3.

TABLE 5.2

Measured Results from CDV Tests

Test Samples Designated No.	Geometric Mean Diameter, d_g, (μm)	Geometric Standard Deviation, σ_g	Mass of UO_2 Vaporized (g)
CDV-16-2	0.01288	1.675	1.53
CDV-16-3	0.01311	1.750	
CDV-21-1	0.01532	1.862	1.40
CDV-21-3	0.01712	1.764	
CDV-24-2	0.01258	1.583	1.10
CDV-19	0.01239	1.603	0.46
CDV-29-1	0.01233	1.610	0.55
Average ±standard deviation	0.01368 ± 0.00183	1.692 ± .103	

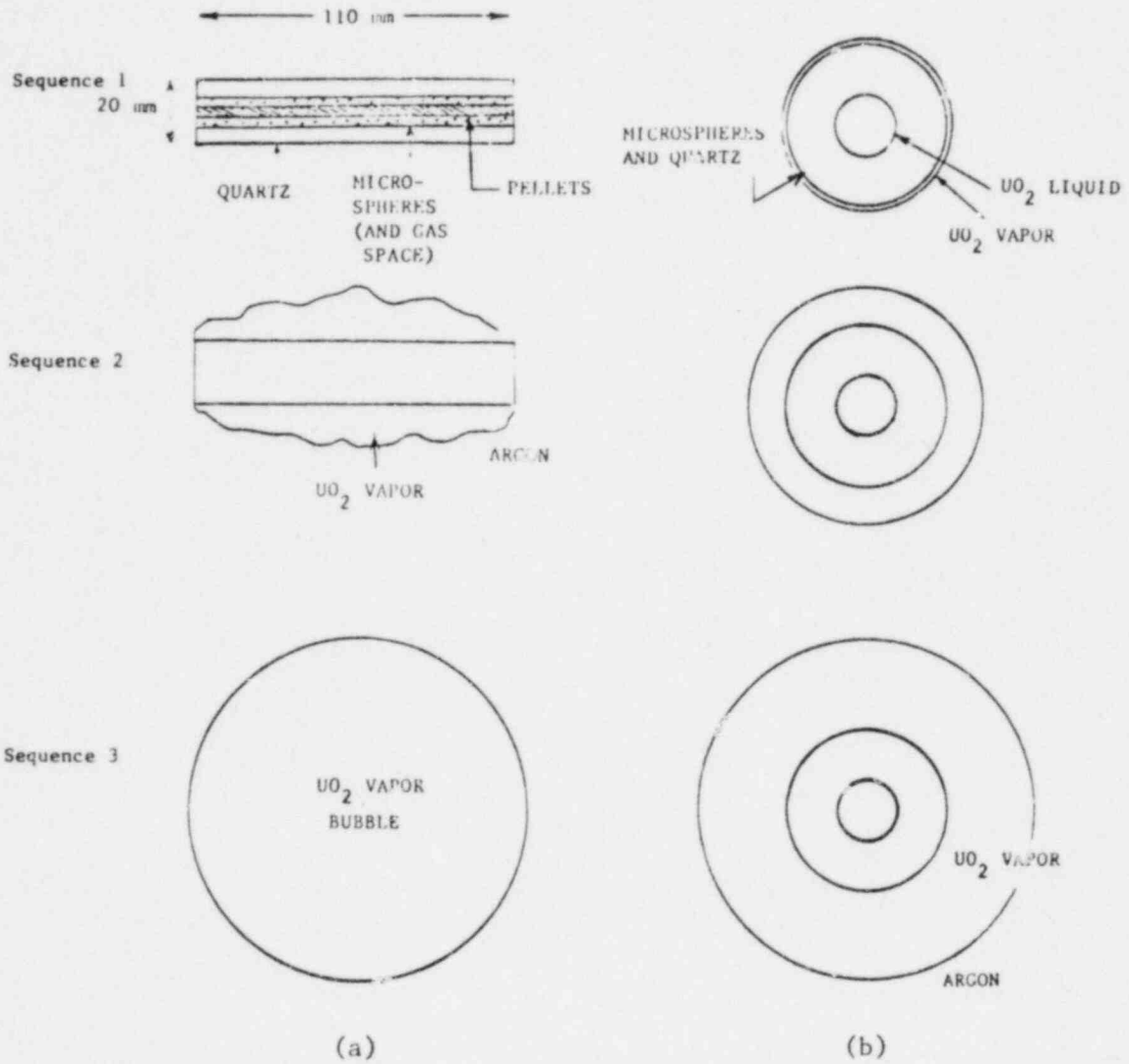

Figure 5.5. Schematic and model representions of expansion process.

which is initially in equilibrium with the hot high pressure liquid in the inner sphere. Low pressure cold argon surrounds the UO_2 vapor shell.

To obtain the model represented by Fig. 5.5(b), it has been assumed that prior to time zero, (i.e. during the capacitor discharge), some amount of saturated UO_2 vapor has escaped from the saturated liquid, has moved through the microsphere region, and is available for expansion against the argon. The amount of UO_2 vapor initially available was set equal to 1 gram since this was the estimated amount of UO_2 condensed in the CDV-argon tests (and all of the vapor in the outer shell in Fig. 5.5(b) eventually condenses in the calculation). Inherent in the model is the assumption that the vapor expansion proceeds on a much faster time scale than the later outward motion and fragmentation of the remaining liquid.*

---

*A more physical model was modelled earlier in the research project in which the UO_2 vapor initially in the outer annulus was the amount required to occupy the available space inside the quartz container (i.e. mostly the spaces between the microspheres). During the vapor expansion process, additional UO_2 mass was allowed to enter the UO_2 vapor sphere from the liquid mass. Difficulties in the required rezoning of the vapor sphere prevented completion of this calculation; although this model is still available as an option in the CIVE computer code, the model used in the present calculation was changed to allow the final condensed mass of UO_2 to be present initially as vapor. The extent to which this simpler model adequately represents the actual time dependent flashing process has not been established.

The UO_2 vapor is the driver channel for the spherical shock tube type expansion; the argon is the driven channel. After rupture of the quartz tube, a spherical shock wave propagates into the low pressure channel thereby compressing the argon. High pressure UO_2 vapor expands adiabatically into the space left by the compressed argon, and a rarefaction wave fan propagates backward toward the center of the driver channel. The rarefaction wave (and resultant adiabatic expansion) causes the pressure and temperature of the UO_2 vapor to drop.

The rate of pressure reduction in the UO_2 vapor is not as fast as the rate of reduction in the saturation vapor pressure at the UO_2 vapor temperature. The thermodynamic state of the expanding UO_2 vapor changes along the curve A-B in the schematic p-T diagram, Fig. 5.6. The ratio of the actual vapor pressure, p_v, along curve A-B in Fig. 5.6 to the saturation vapor pressure, p_{sat}, at the vapor temperature is greater than one. The ratio of these two pressures, $S = p_v/p_{sat}$, is called the supersaturation ratio. The vapor is supersaturated and is metastable. Nucleation may occur spontaneously due to random molecular collisions. Critical embryos will form when the appropriate balance is achieved between surface free energy and bulk free energy, according to classical nucleation theory.

In the present model, embryos are formed by homogeneous nucleation. The presence of foreign condensation nuclei or surfaces such as ions, dust, quartz or UO_2 microspheres, would cause heterogeneous nucleation condensation of the UO_2 vapor near the saturation condition, i.e. point

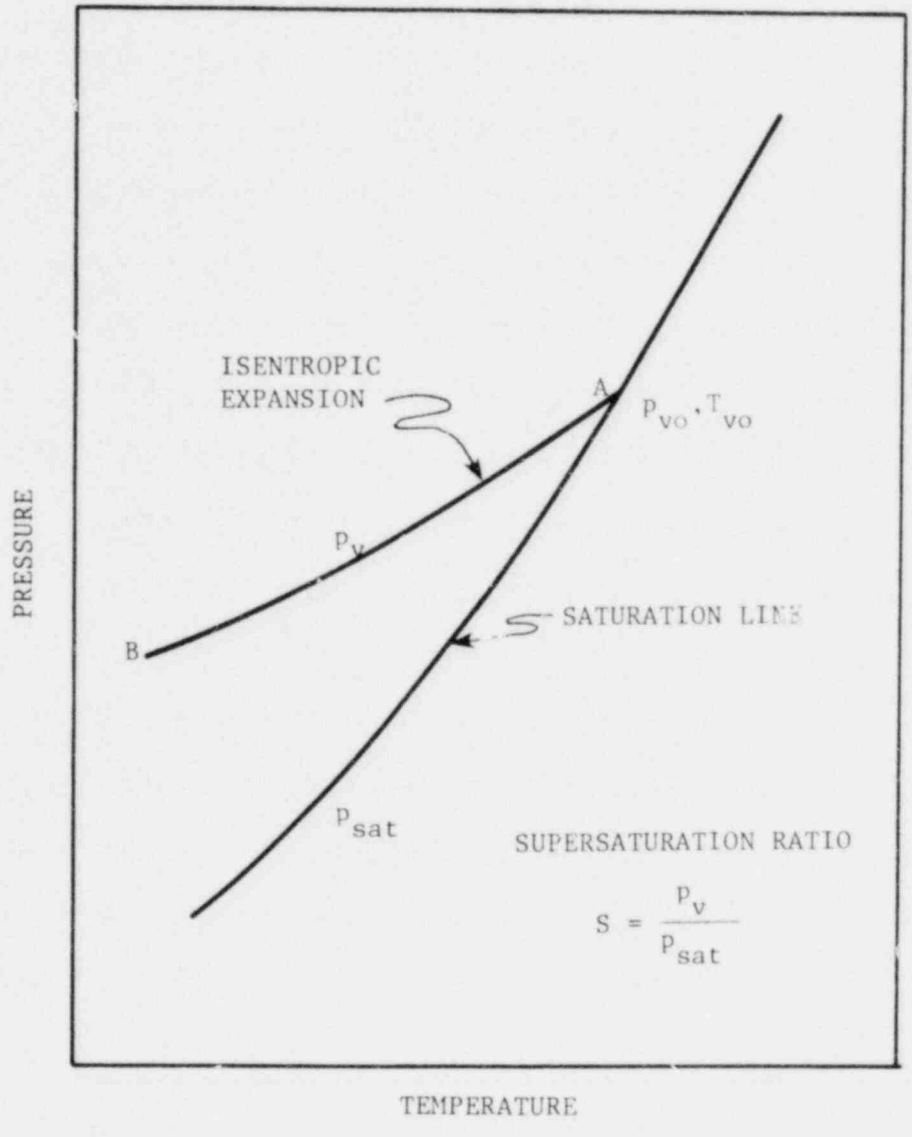

Figure 5.6. Schematic p-T diagram of isentropic expansion.

A, on Fig. 5.6. Some heterogeneous nucleation and condensation likely does occur on the UO_2 microspheres in the CDV tests; however, homogeneous nucleation is believed to produce the embryos that grow to the small particles observed in the CDV tests. In the present model, it is assumed that nuclei are not initially present in the UO_2 vapor expansion region so that only homogeneous nucleation is assumed to occur.

After nucleation, stable droplets will first grow due to condensation and then continue to grow or perhaps contract due either to further condensation or to evaporation. Both the number and size of the condensed particles are followed throughout the expansion process in order to calculate a final particle-size distribution.

Precedents for Model Phenomena

The theoretical bases for the model developed here are not new. Two fundamental and extensively investigated phenomena are combined in the model. The first involves the dynamics of the expansion process itself. Despite the much larger size of the source in the CDV experiments than in exploding wire experiments, it is believed that the expansion process is similar to that observed in exploding wire experiments. The second phenomenon involves homogeneous nucleation and condensation growth in rarefaction waves. Onset of condensation from supersaturation has been extensively documented in shock tube experiments. Some of the documentation of these phenomena is reviewed briefly below.

A series of conferences on exploding wires were reported in References 7-10. Michel-Levy and Muraour were among the first to describe the connection between a shock wave and a wire explosion.[8] Kerr cell schlieren

photography was employed by Müller[6] to study the exploding wire phenomena, in which the shock wave induced by the wire explosion and metal vapor front was observed by optical equipment. Bennett[10] used backlighting and rotating mirror camera techniques to record the light flash produced by electrically exploding a fine cylindrical wire. The streak picture (Fig. 5.7) taken by Bennett shows the vapor contact surface and the shock front trajectories. It is shown in Fig. 5.7 that the shock separates from vapor front at about 1μs. An analytical similarity solution in cylindrical symmetry for instantaneous energy deposition in a mathematical line developed by S. Lin[11] was compared by Bennett with the measured shock front data. Both the shock induced by the wire explosion and the vapor front agreed with the similarity solution. Rouse[6] also performed a theoretical analysis of the hydrodynamic flow in exploding wire experiments. In his analysis, a Lagrangian computer code was developed to solve a system of governing equations numerically. The calculated shock front curve was in approximate agreement with that measured by Bennett.

Experiments and theoretical analysis of stationary supersonic-nozzle flow with vapor condensation have been employed to investigate the validity of nucleation theory. References 12, 13 and 14 give a detailed review in this field. Wegener and Ludquist[15] were the first to use shock tubes to study the condensation of water vapor in a rarefaction wave fan. Schlieren pictures taken by Glass and Patterson[16] showed the vapor condensation zone in the expansion fan

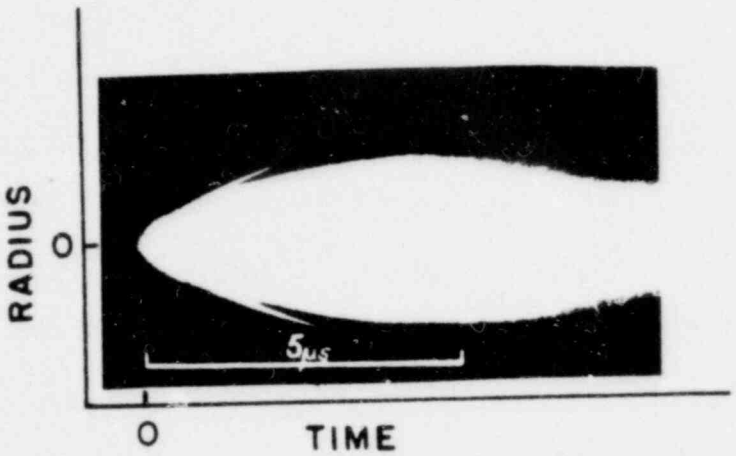

Figure 5.7. Streak picture for 0.13 mm copper wire[10].

in a shock tube. Kawada and Mori[17] studied the homogeneous nucleation condensation kinetics of several kinds of organic material vapor with shock tube techniques. Barschdorff[18] investigated the carrier gas effects on homogeneous nucleation of water vapor in a shock tube. Kalra[19] performed a series of shock tube experiments to investigate the condensation phenomena in a nonstationary, nonequilibrium expansion of water vapor and water vapor with carrier gas. Kalra's measured results were compared with the theoretical results performed by Sislian.[20] While some disagreement remains between theory and experiment, the basic nucleation and condensation growth models employed in these publications have been generally verified, and they provide the bases for the models used here to describe the CDV tests.

Components of the CIVE Computer Model

The differential equations required to obtain partial size distributions were integrated numerically with the CIVE (Condensation In Vapor Expansion) computer code.[21] The equations in the model will be published in a forthcoming NUREG report.[22] Only the basic parts of the model will be described here.

Gas Dynamics

The expansion process must be calculated by conventional methods in gas dynamics. For the present model, the WONDY-IV computer code[23] was used for these calculations, and hence was incorporated as part of the CIVE code.

WONDY-IV is one-dimensional finite difference computer program for the analysis of wave propagation developed at Sandia Laboratories,

Albuquerque. WONDY can be used in slab, cylindrical and spherical geometry; it employs a Lagrargian mesh; and it treats the discontinuity at the shock wave front by means of the VonNewmann-Richtmyer artificial viscosity.[24]

The equations governing the gas flow are the mass, momentum and energy conservation equations, together with appropriate equations of state for UO_2 vapor and argon.

Nucleation

The nucleation rate used in this calculation (derived, for example, in Reference 25) is given by

$$J = \left(\frac{p_{sat}(T_v)}{k\,T_v}\right)^2 \left(\frac{2\sigma m}{\pi}\right)^{\frac{1}{2}} \frac{S^2}{\rho_\ell} \exp\left(-\frac{4\pi}{3}\frac{\sigma r^{*2}}{k T_v}\right)$$

where

J = nucleation rate (stable nuclii created/$m^3 \cdot s$)

σ = surface tension (J/m^2)

m_1 = mass per molecule

k = Boltzmann constant

S = supersaturation ratio

ρ_ℓ = liquid density

r^* = critical radius

T_v = vapor temperature

p_{sat} = saturation pressure

Droplet Growth

Stable liquid drops formed by homogeneous nucleation will experience growth as a result of condensation. Evaporation from the droplets also occurs and the actual growth rate depends on the difference between condensation and evaporation rates. The kinetic theory of condensation and evaporation has been applied to calculate the particle growth rates following nucleation by many investigators, including Hill,[26] Kang,[27] Wegener,[13] Wegener and Wu,[14] Sizlian[20] and Kennedy, et al.[2]

The kinetic theory approach is applicable for the current problem since the droplet size (10^{-9} < diameter < 6×10^{-8} m) is smaller than the mean free path of a vapor molecule ($\lambda \sim 8 \times 10^{-8}$ m at the initial vapor conditions of 5000 K, 4.6 MPa pressure).

Mass transfer by condensation and evaporated were calculated from the following kinetic theory relation:

$$\frac{dm}{dt} = \frac{4\pi r^2 \alpha_c}{\sqrt{2\pi R_v}} \left[\frac{p_v}{\sqrt{T_v}} - \frac{p_{sat}(T_\ell)}{\sqrt{T_\ell}} \exp\left(\frac{2\sigma}{R_v T_\ell \rho_\ell r}\right) \right]$$

The use of this mass transfer equation led to an equation for the rate of change of liquid droplet radius with time.

In addition to mass tranfer, energy balances for both the vapor and liquid phases were required. This resulted in an equation for the change in liquid droplet temperature. Simultaneous solution of the droplet temperature and radius was one of the difficult computational problems which had to be solved to make the computer code work.

Particle Grouping

A large amount of computation time is consumed on the computation of radius and temperature of the particles for each gorup in each zone at each time step. It was, therefore, necessary to limit the number of groups in each zone in order to reduce the computation time. A grouping technique was employed to combine the groups when the total number of groups in a zone exceeded a pre-set maximum allowable number of groups. Grouping criteria and methods were carefully selected in order to minimize the distortion of the particle-size distribution caused by grouping.

The procedure to choose a pair of particle groups to be combined consisted of two steps. The first step was to put the groups in the order of increasing radius such that the first-group particles were the smallest size and the Nth-group particles were the largest size. The second step was to find the ith group with the least number of particles. This group was then combined with the group nearest to it in particle diameter.

When a pair of particle groups was combined, the total surface area, mass, and internal energy of the particles were conserved. The total number of particles was not conserved; this did not result in any significant distortion of the particle-size distribution since the relative number of particles lost or gained was extremely small. The total particle mass and internal energy were conserved in order not to affect the vapor condition. The total surface area of the particles was conserved to insure that the correct rates of mass transfer were calculated.

Example calculations of the particle-size distribution with and without grouping were performed for 3.12 μs after the start of the vapor expansion. The results at 3.12 μs showed no significant distortion caused by grouping.

Sequence of Calculations

The differential equations were integrated by finite difference methods with the CIVE (Condensation In Vapor Expansion) computer code. The gas dynamics equations were decoupled from the homogeneous nucleation and condensation growth equations in the sense that the two sets of equations were solved sequentially during a time step. The calculations (in the UO_2 region) at each time step involved three stages. The first stage was a calculation of an adiabatic vapor expansion in which the gas dynamics equations were integrated in WONDY and during which the condensation mass fraction, g, was held constant. The second stage was a calculation of homogeneous nucleation and condensation growth based on the vapor thermodynamic properties calculated in the first stage. Also in the second stage, the new condensation mass fraction, g, was computed. The third stage was an adjustment of parameters necessary to begin a new time step. These parameters include vapor thermodynamic properties and particle grouping.

5.4 Comparison of Calculated and Experimental Results

The principal calculated result is the particle size distribution. An auxiliary result is the rate of expansion of the UO_2- argon interface. As described in Section 5.2, this expansion rate was observed in the movies hence this calcualtion provides an "intermediate" point of comparison for

the integral experiment. The comparison of the calculated and measured UO_2-argon interface is presented in the present section.

In this section the calculated particle size distribution for the "reference case" is compared with measured particle size distributions. In Section 5.5 are presented the results of a parametric study which was performed to investigate the sensitivity of the calculated results to variations in selected model parameters.

In this section calculated particle-size distributions are ususally plotted in the manner used in Fig. 5.3 for the experimental results. Calculated values of d_g and σ_g are also reported for comparison with the experimental values from Table 5.2.

Motion of the UO_2-Argon Interface

The radius of the expanding UO_2 vapor bubble was calculated for values of initial saturated UO_2 vapor of 5000 K, 5500 K and 6000 K. The calculated curves of radius versus time are plotted as solid lines in Fig. 5.8.

The experimental data from Table 5.1 are also plotted on Fig. 5.8 for comparison. To understand the experimental points on the figure, consider test 51. In the first frame in which the expanding sphere is observed in the movies, the radius is estimated to be 28 mm. This point (28 mm) is located on the calculated curve for 5500 K. This corresponds to 8.5×10^{-6}s on the time scale for this test. One frame later, at time 1.085×10^{-4}s, the measured sphere radius is ~51 mm. For most tests, there are two successive frames in which the sphere can be

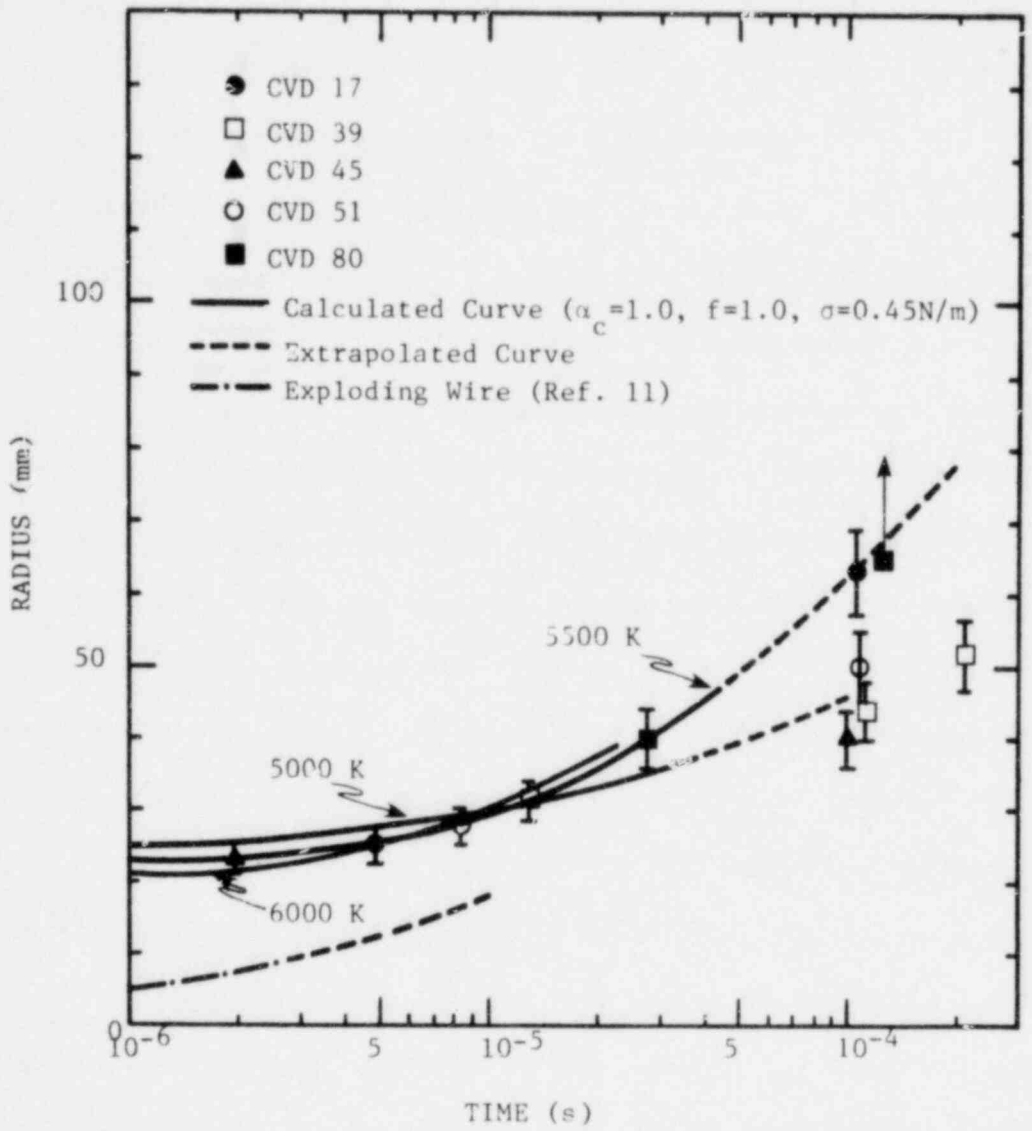

Figure 5.8. Vapor front as a function of time.

observed. In the next frame, the sphere is larger than the opening through which the movies were being taken. Test 39 differs from the others; in this test three consecutive frames can be observed. This test appears to be less energetic than the others.

It is indicated on Fig. 5.8 that the calculated UO_2-argon interface trafectory is in the same range as that measured in the CDV tests. This provides evidence that the vapor sphere viewed in the CDV movies is being interpreted correctly and gives an "intermediate" point of comparison for the integral experiment.

One further point of comparison is available to support the validity of the gas dynamics phenomena being postulated for the CDV tests. This comparison is with the exploding wire tests of Bennett discussed briefly in Section 5.3. The trajectory of the vapor front reported by Bennett is also plotted on Fig. 5.8, where the radius for the exploding wire case is for a cylindrical expansion rather than the spherical expansions of the CDV tests. The exploding wire expansion has a characteristic similar to the CDV vapor expansion, although the time scale is a factor of 1 to 10 faster. Agreement in shape and time scale to this extent for experiments as different as CDV and exploding wires lends support to the argument that similar gas dynamics phenomena are controlling the expansion in both cases.

Reference Case Results

Particle-size distributions were calculated for a reference case. Values for parameters later to be varied, such as initial fuel temperature

T_{fo}, condensation coefficient σ, fuel surface tension γ, and initial mass of fuel vapor M_o, were selected for the reference case. These values were:

T_{fo} = 5000 K

σ = 0.1

γ = 0.45 N/m

M_o = 1 gram

Also the initial argon pressure used for most of the experiments, 1 atmosphere (101 kPa), was used; and all of the heat of vaporization, h_{fg}, from condensing vapor was assumed to be deposited in the liquid drops.

Results of the calculated particle size distributions for the reference case and also for an initial fuel temperature of 5500 K are plotted in Fig. 5.9. Also plotted in the figure are the two extremes of the seven measured distributions plotted earlier in Fig. 5.3.

The comparison shows good agreement throughout most of the distribution curve except at the large size particle tail. The small variation of 500 K initial fuel temperature causes a variation in the circulated particle-size distribution almost as high as the variation in experimental distribution between tests; and it is acknowledged that the uncertainty in fuel temperature after vaporization discharge if fairly high. The experimental curves appear to be log normal (i.e. linear on log normal probability paper) throughout the particle size range. The calculated distributions tend to deviate from log normal above the 90 percentile range.

Assuming a log normal distribution for the calculated particle-size distribution, calculated values for d_g and σ_g are given in Table 5.3. These are compared with the measured values presented earlier in Table 5.2.

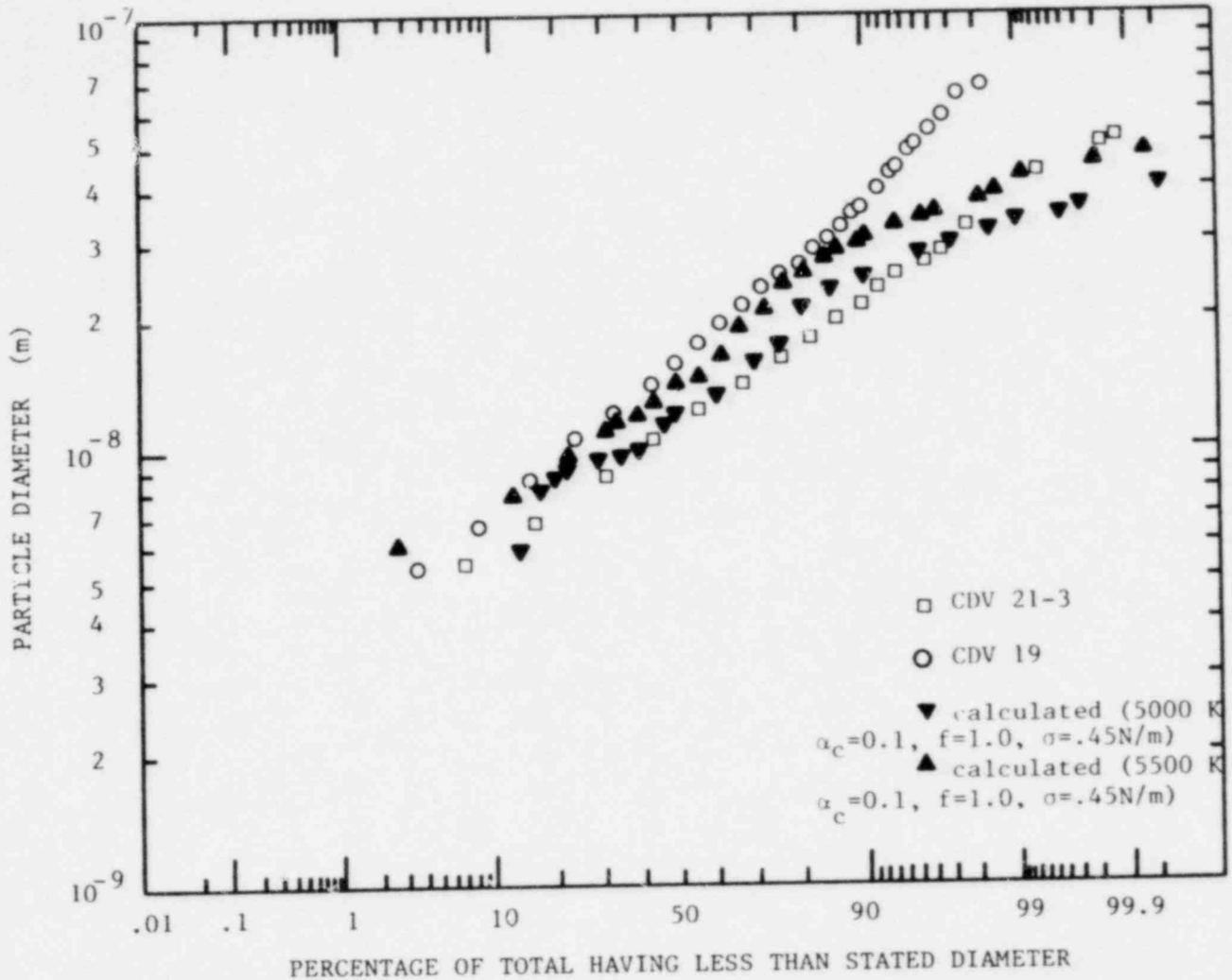

Figure 5.9. Comparison between measured and calculated particle-size distributions.

TABLE 5.3

Comparison of Measured and Calculated Values of d_g and σ_g

	Calculated Distribution		Measured Distributions (Table 5.2)
	T_{fo}=5000 K	T_{fo}=5500 K	
Geometric mean diameter, d_g (m)	0.01271	0.01547	0.01368 ± 0.00183
Geometric standard deviation, σ_g	1.620	1.624	1.692 ± 0.103

Details of the reference calculation are also of interest to understand the pheonomena that occur during the transient. Following bursting of the quartz container, the vapor-argon interface expands outward; it sends a shock wave, which is smeared into several zones resulting from the pseudo-viscous pressure, into the argon region, leading to an increase in the argon pressure. At the same time a rarefaction wave fan (resulting from vapor expansion) propagates toward the center, which reduces the pressure of the UO_2 vapor. These phenomena are illustrated in Fig.5.10 which shows the system pressure profile at several stages during the expansion. Each step in the histogram pressure profile represents one of the fifteen mesh spaces in the finite difference calculation. Figure 5.11 shows the supersaturation ratio of zones 1, 7 and 15 as a function of time. Zone 15 is the outer zone of the expanding UO_2 region. The time lag for the start of supersaturation in the inner zones corresponds to the finite time needed for the rarefaction wave to reach these zones.

Figure 5.12 represents the supersaturation ratio, S, nucleation rate, J, and the critical radius, r^*, in the 15th zone. Vapor is initially saturated (S=1); the degree of supersaturation then rises as the combined results of vapor expansion and a time lag before homogeneous nucleation begins. The supersaturation ratio reaches the highest point, S=3.44, at 1.94 μs; then it returns nearly to the saturated condition. The nucleation rate follows the same pattern. It rises and drops dramatically because of the strong exponential

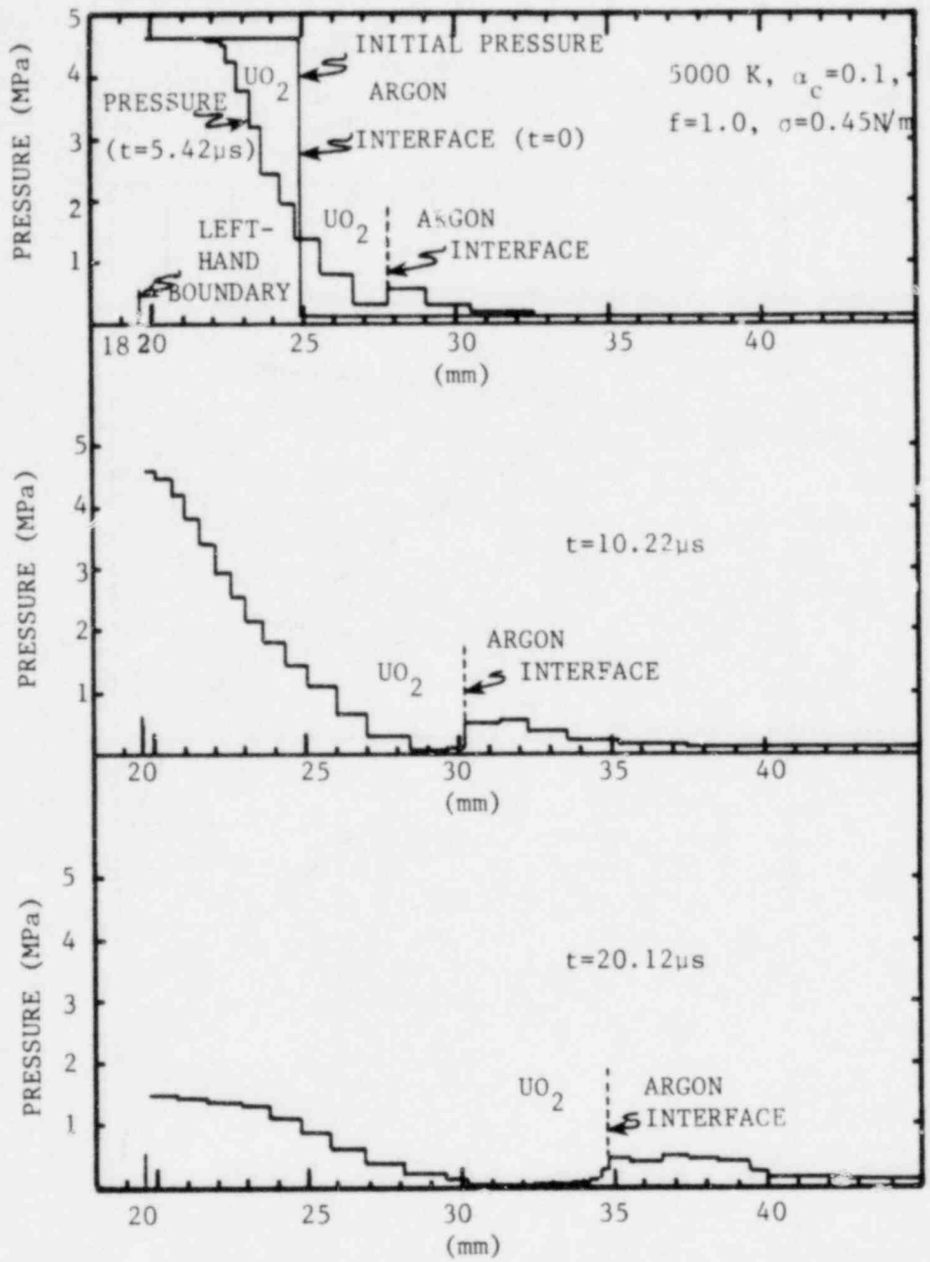

Figure 5.10. System pressure profile and position of the UO_2-argon interface at different times.

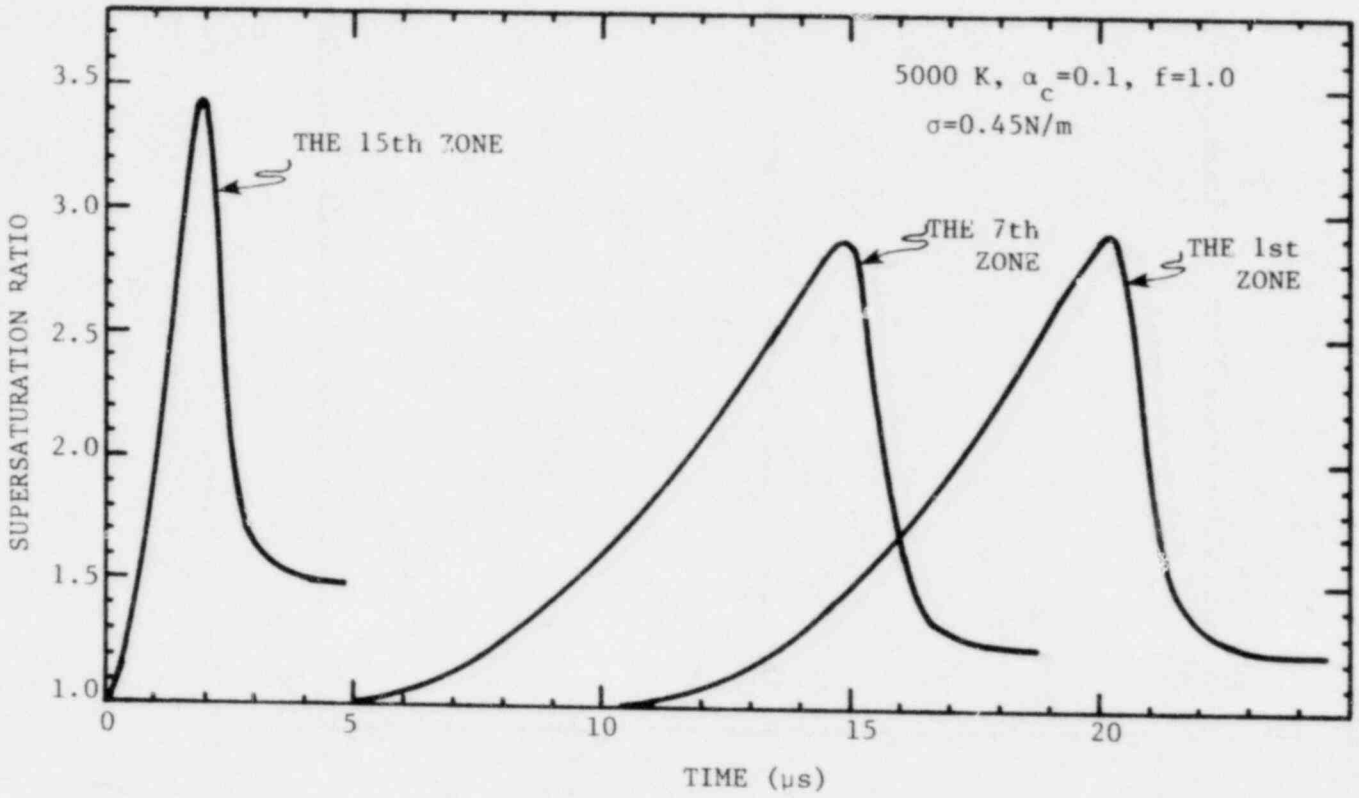

Figure 5.11. Supersaturation ratio vs. time for the 1st zone, the 7th zone and the 15th zone.

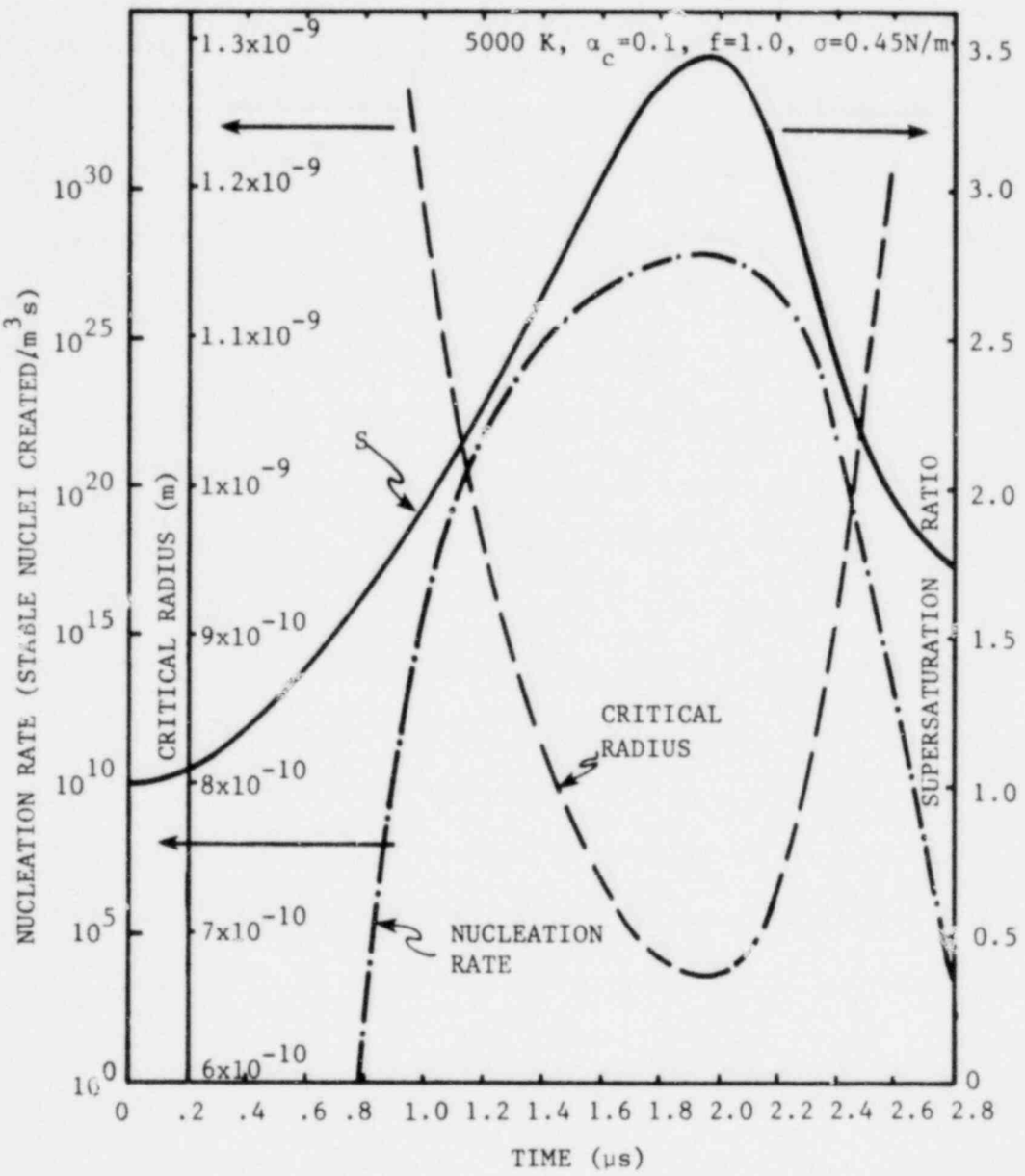

Figure 5.12. The supersaturation ratio, S, nucleation rate, J, and the critical radius, r*, in the 15th zone, as a function of time.

dependence of the nucleation rate on the supersaturation ratio. The sizes of the nucleated particles are in the opposite direction as indicated in Fig. 5.12.

After 1.94 μs, the vapor is still expanding outward against the argon; however, the supersaturation ratio is now decreasing while the vapor is still expanding, which is contrary to the behavior before 1.94 μs. This physical pheonomenon is the result of the competition between homogeneous nucleation and heterogeneous condensation (vapor condensing on existing particles). At the early part of the vapor expansion, vapor condensation is dominated by the homogeneous nucleation process since there is a lack of heterogeneous condensation sites existing in the system. Gradually the heterogeneous condensation process becomes significant because the number of particles nucleated rises rapidly and the vapor tends to condense on those particles. After 1.94 μs this zone contains such a hugh number of particles that the heterogeneous condensation process dominates the vapor condensation. Thus the vapor state approaches the saturated condition and no new particles are nucleated (after 2.8 μs) in spite of continued vapor expansion. The rest of the vapor zones exhibit the same behavior though at different times.

Figure 5.13 shows the transient behavior of the particle-size distribution during the condensation process. The small size particles in the distribution curve at 5.42 μs are contributed by newly nucleated particles. The particles at this time have not yet experienced much heterogeneous condensation, and the geometric mean diameter is low at

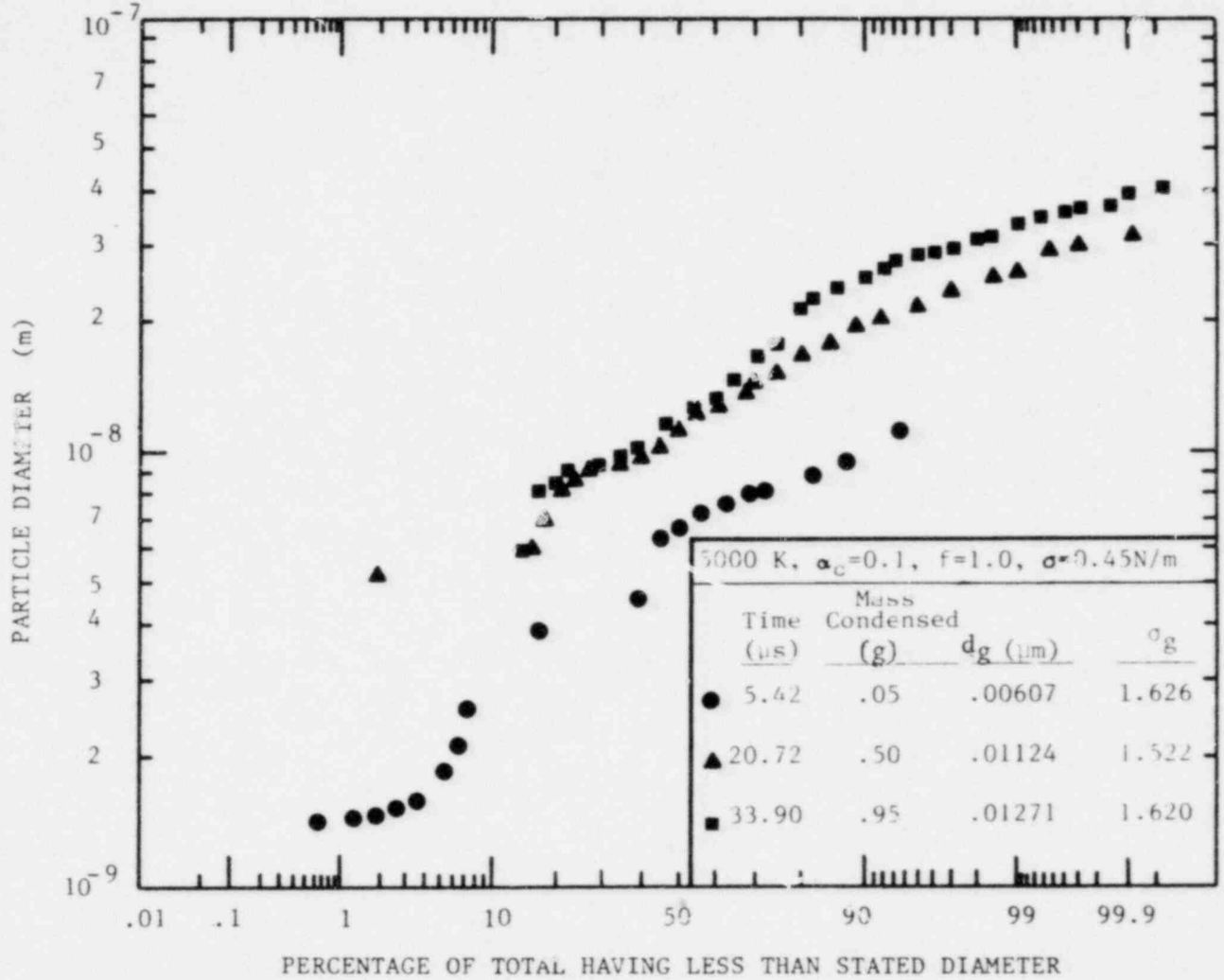

Figure 5.13. Calculated particle-size distribution as a function of time.

.0061 μm. At time 20.72 μs, the homogeneous nucleation process has been terminated because at this time the system contains a hugh number of particles on which the vapor tends to condense through the heterogeneous condensation process. Most of the particles in the system have by this time experienced condensation growth, and the geometric mean diameter has grown to be .0112 μm. At 33.90 μs, 95% of the vapor has been depleted and the computation is terminated.

5.5 Parameter Study

A parameter study was performed to investigate the sensitivity of the particle-size distribution to various selected parameters. The results are presented in this section.

The following parameters were varied: initial fuel temperature, condensation coefficient, surface tension, distribution of heat of vaporization, initial mass of fuel vapor, and argon pressure. A summary of the results of the parameter study is given in Table 5.4.

Initial Fuel Temperature

Computations with constant surface tension (σ=0.45 N/m), condensation coefficient of 1.0, f (fraction of heat of vaporization deposited onto the drop as vapor condenses) of 1.0, and 1 gram of initial saturated UO_2 vapor at 6000 K, 5500 K and 5000 K respectively in the driver channel were performed. The results are presented in Fig. 5.14 and Table 5.4. The geometric standard deviation increases with increase of the initial vapor temperature, and the geometric mean diameter increases about 19% with every 500 K increment of the initial vapor temperature.

TABLE 5.4

A Summary of the Parametric Study

Case No.	Initial UO_2 Vapor Condition: Vapor @ $T_{sat.}$ (K)	Vapor Mass(g)	Parameters: α_c	f	σ	Mass(g) Condensed	d_g (μm)	σ_g
1	6000	1.0	1.0	1.0	const.	.859		
2	5500	1.0	1.0	1.0	const.	.920	.02182	1.628
3	5500	1.0	0.1	1.0	const.	.923	.01547	1.624
4	5500	1.0	0.05	1.0	const.	.928	.01273	1.573
5	5500	1.0	0.1	1.0	$\sigma(T)$	.921	.01288	1.519
6	5000	1.0	1.0	1.0	const.	.921	.01827	1.615
7	5000	1.0	0.1	1.0	const.	.950	.01271	1.620
8	5000	1.0	0.1	0.9	const.	.919	.01858	1.549
9	5000	0.5	0.1	1.0	const.	.472	.01123	1.556

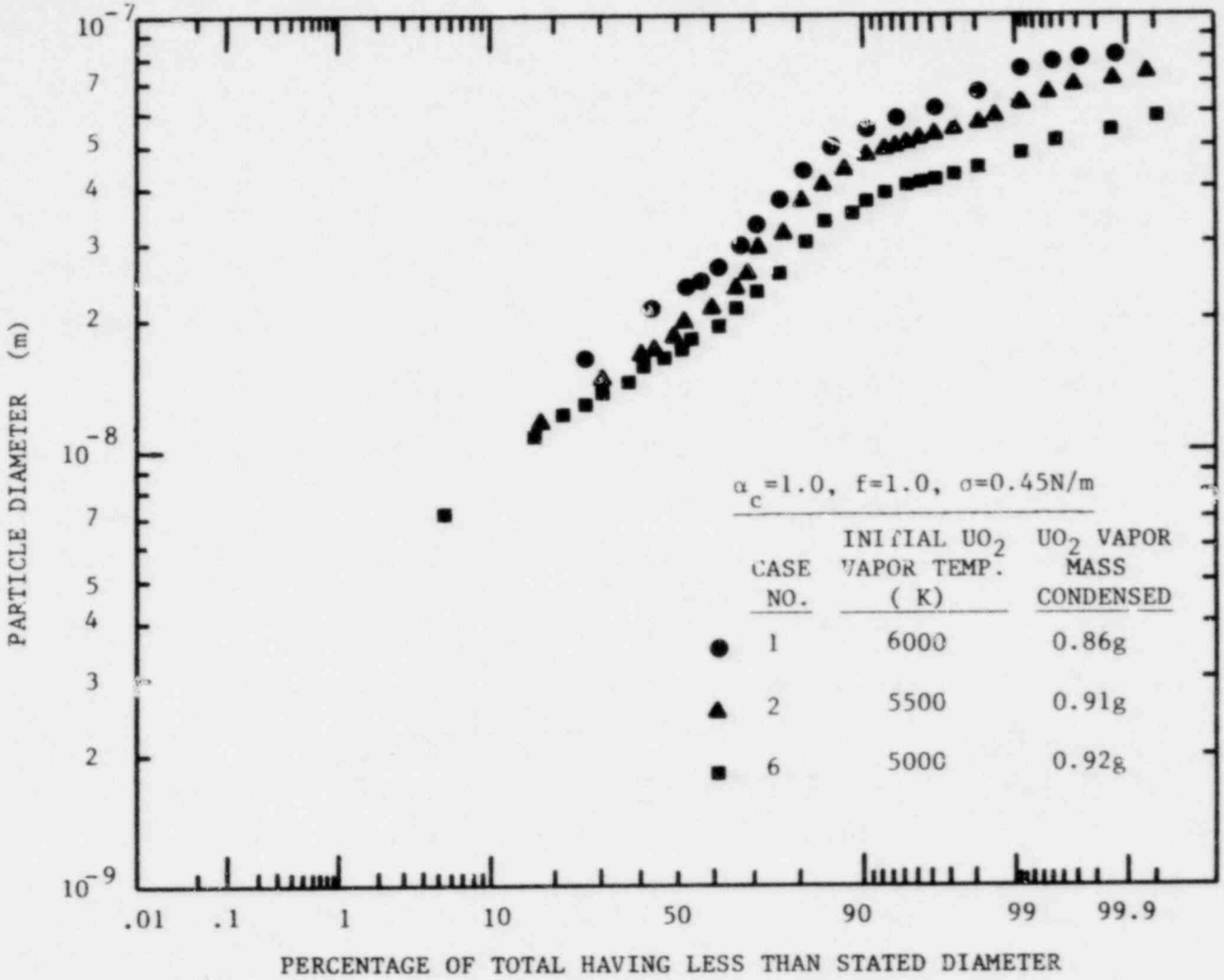

Figure 5.14. Calculated particle-size distribution as a function of initial vapor temperature.

Condensation Coefficient

Values of condensation coefficient, α_c, are reported from unity to about 0.01 for materials. Reducing the condensation coefficient below unity lowers the particle size, as shown in Fig. 5.15 and Table 5.4.

Surface Tension

In the reference case calculation, a constant UO_2 liquid surface tension, σ=0.45 N/m, corresponding to the value at the UO_2 melting point (3138 K) was used. In addition a calculation was made for a temperature dependent surface tension which limits to 0.45 N/m at the UO_2 melting point. The following semi-empirical formula for the temperature dependence of surface tension discussed by Guggenheim[28] was used:

$$\sigma \propto \left(\frac{1}{v_\ell} - \frac{1}{v_v}\right)^{2/3} \left(1 - \frac{T}{T_{crit}}\right)$$

where v_ℓ and v_v are the specific volumes of UO_2 liquid and vapor at temperature T, and T_{crit} is the critical temperature of UO_2, for which 8000 K was used. The surface tension as a function of temperature in N/m that limits to the correct value at the melting point is

$$\sigma = 1.69 \times 10^{-3} \left(\frac{1}{v_\ell} - \frac{1}{v_v}\right)^{2/3} \left(1 - \frac{T}{8000}\right)$$

The particle-size distribution with a temperature dependent surface tension is presented in Fig. 5.16 and Table 5.4. The geometric mean diameter is reduced by 17% below the value with a constant surface tension at 0.45 N/m.

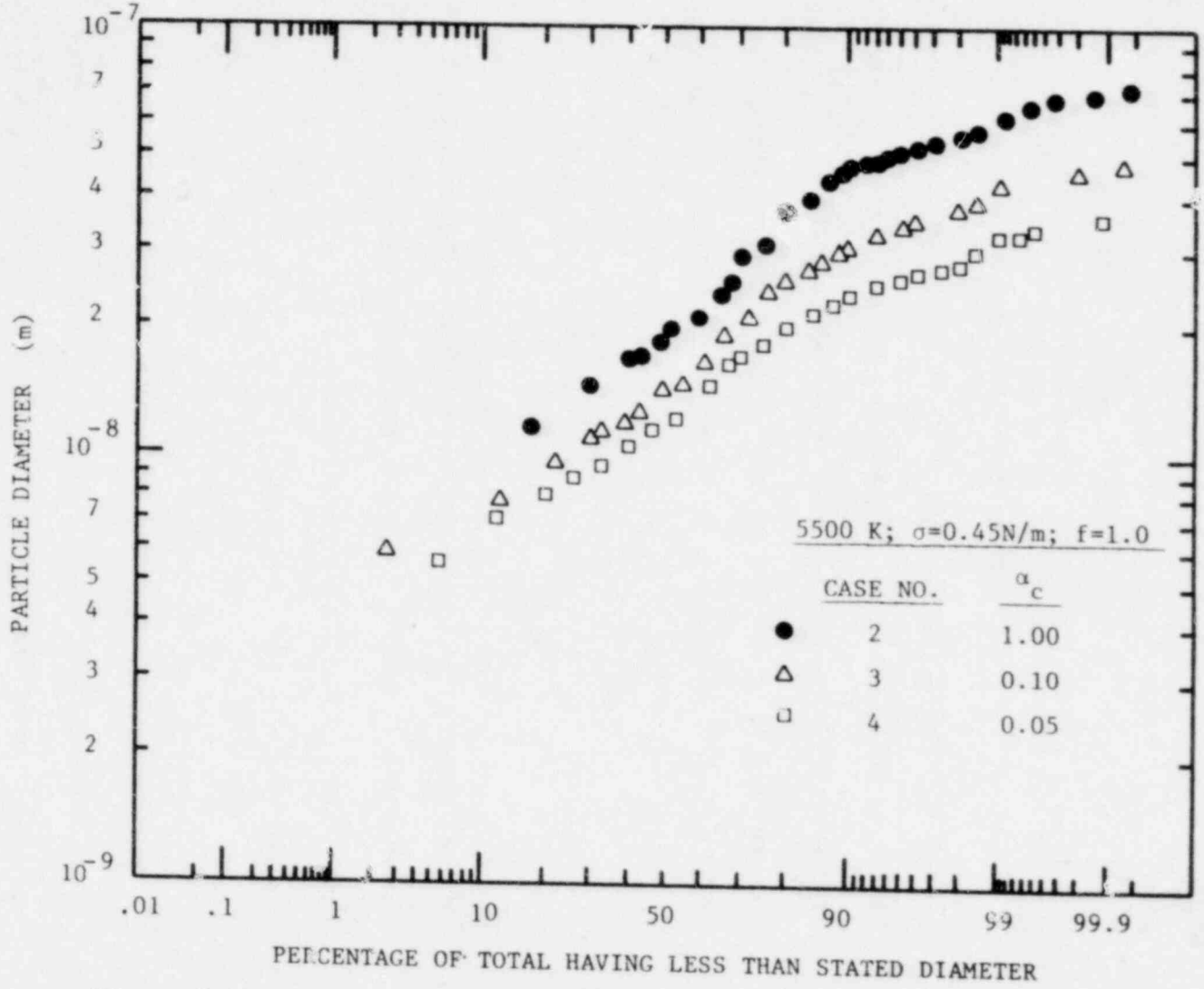

Figure 5.15. Calculated particle-size distribution as a function of condensation coefficient.

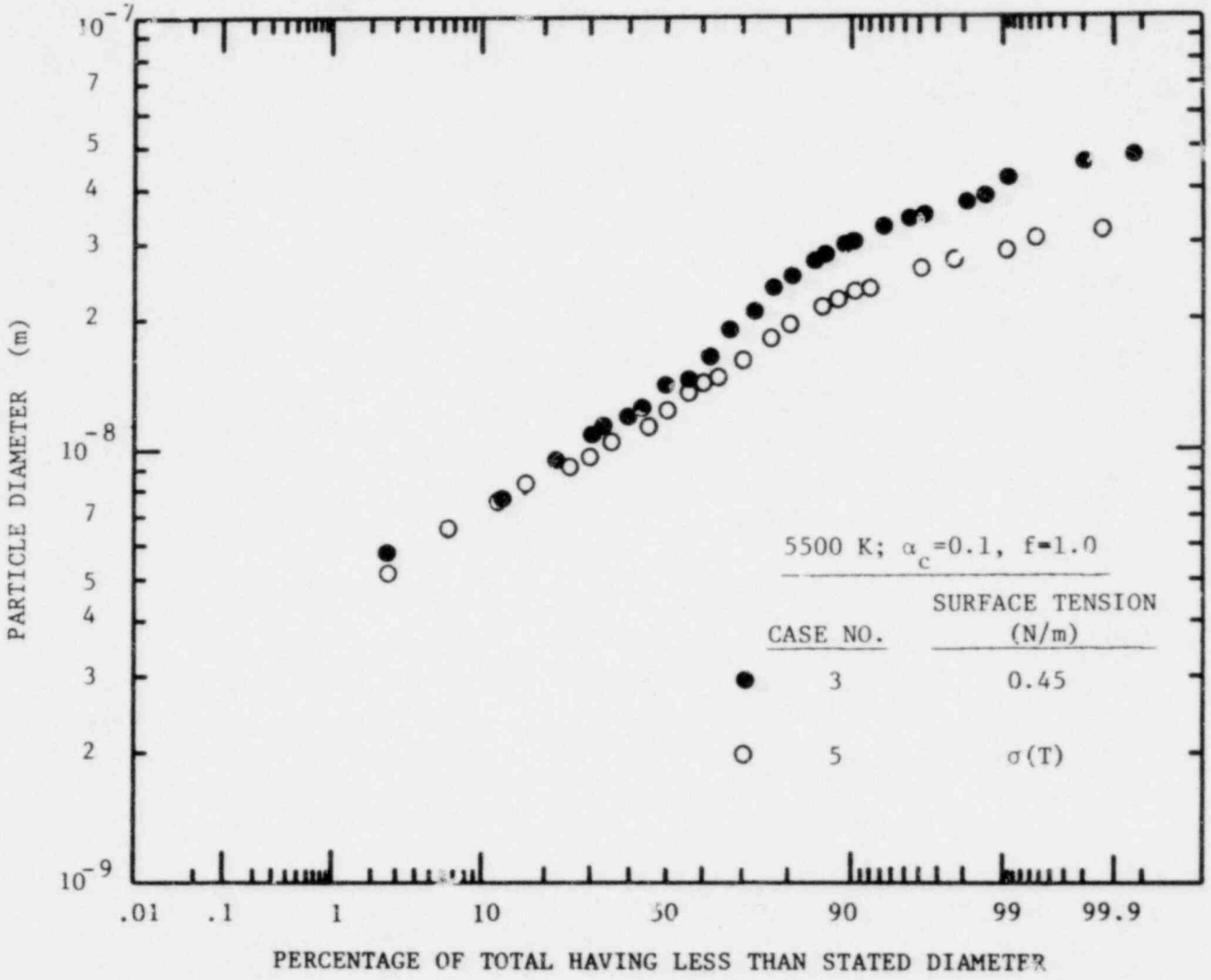

Figure 5.16. Calculated particle-size distribution as a function of UO_2 liquid surface tension.

Distribution of Heat of Vaporization

The value f=1.0 corresponds to the deposition of all of the heat of vaporization into the liquid droplet as vapor condenses. This assumption was made in the reference case calculation. Analyses with f other than unity were performed and the results are presented in this section.

A value of f lower than unity implies that part of the heat of vaporization remains in the vapor environment as vapor condenses; this results in an increase in the temperature of the vapor and a corresponding decrease in the supersaturation ratio, thus reducing the total number of particles nucleated. Therefore the final geometric mean diameter should be larger.

The calculated results are presented in Fig. 5.17 and Table 5.4 (cases 7 and 8). With 10% of the heat of vaporization remaining in the vapor (f=0.9), the geometric mean diameter is increased by 46%.

Initial Mass of Fuel Vapor

The amount of fuel vapor yield from the CDV tests were measured from 0.46 to 1.55 gram as indicated in Table 2-2. Therefore, an analysis was made with 0.5 gram mass of saturated UO_2 vapor at 5000 K in the driver channel. Figure 5.18 and Table 5.4 show the comparison between two cases (1.0 g and 0.5 g initial vapor mass). The results indicate that there is no significant discrepancy in the particle-size distribution in the small particle size range. However, significant deviation exists in the large particle size range.

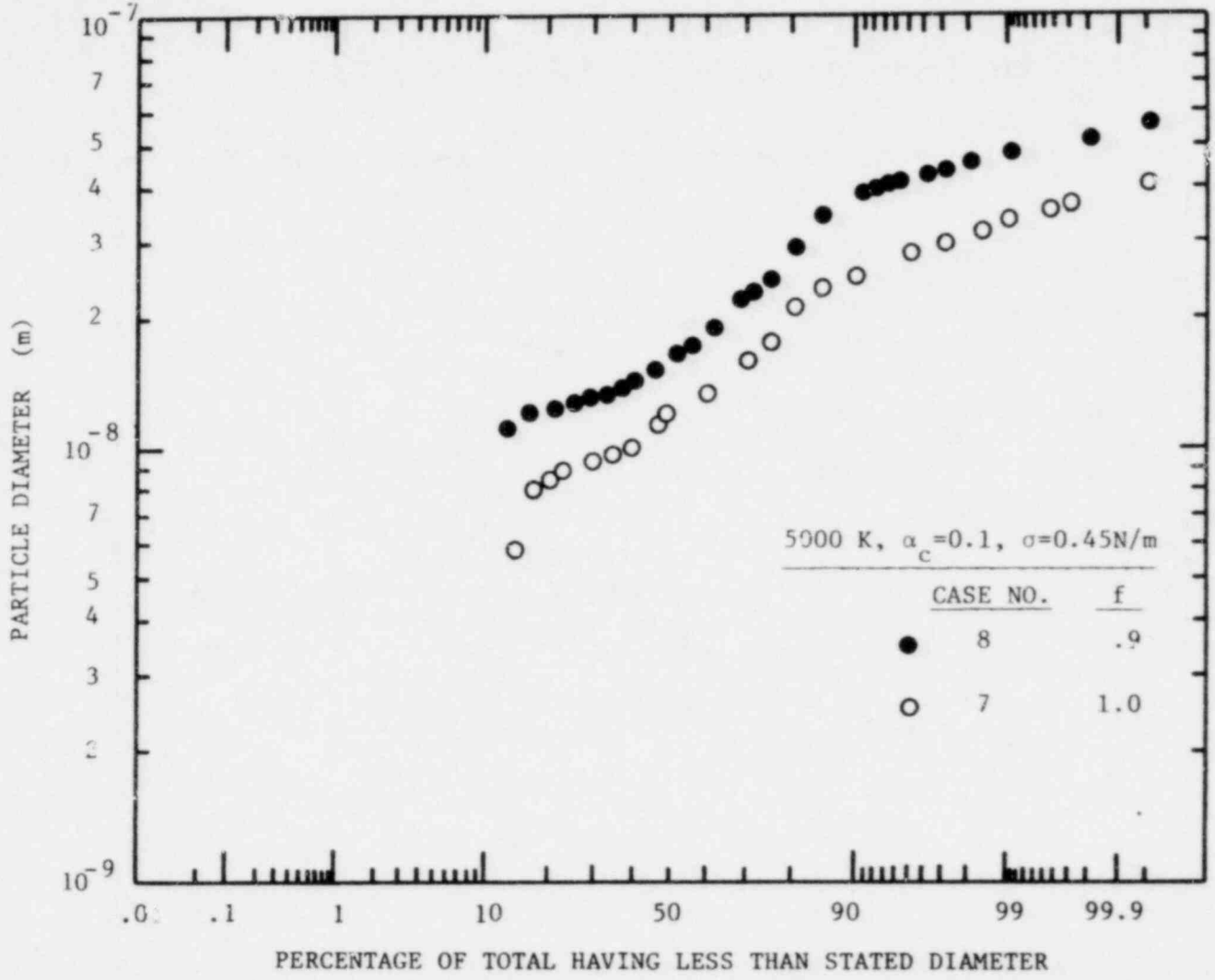

Figure 5.17. Calculated particle-size distribution as a function of the partition of the heat of vaporization between the droplet and the vapor as the vapor condenses.

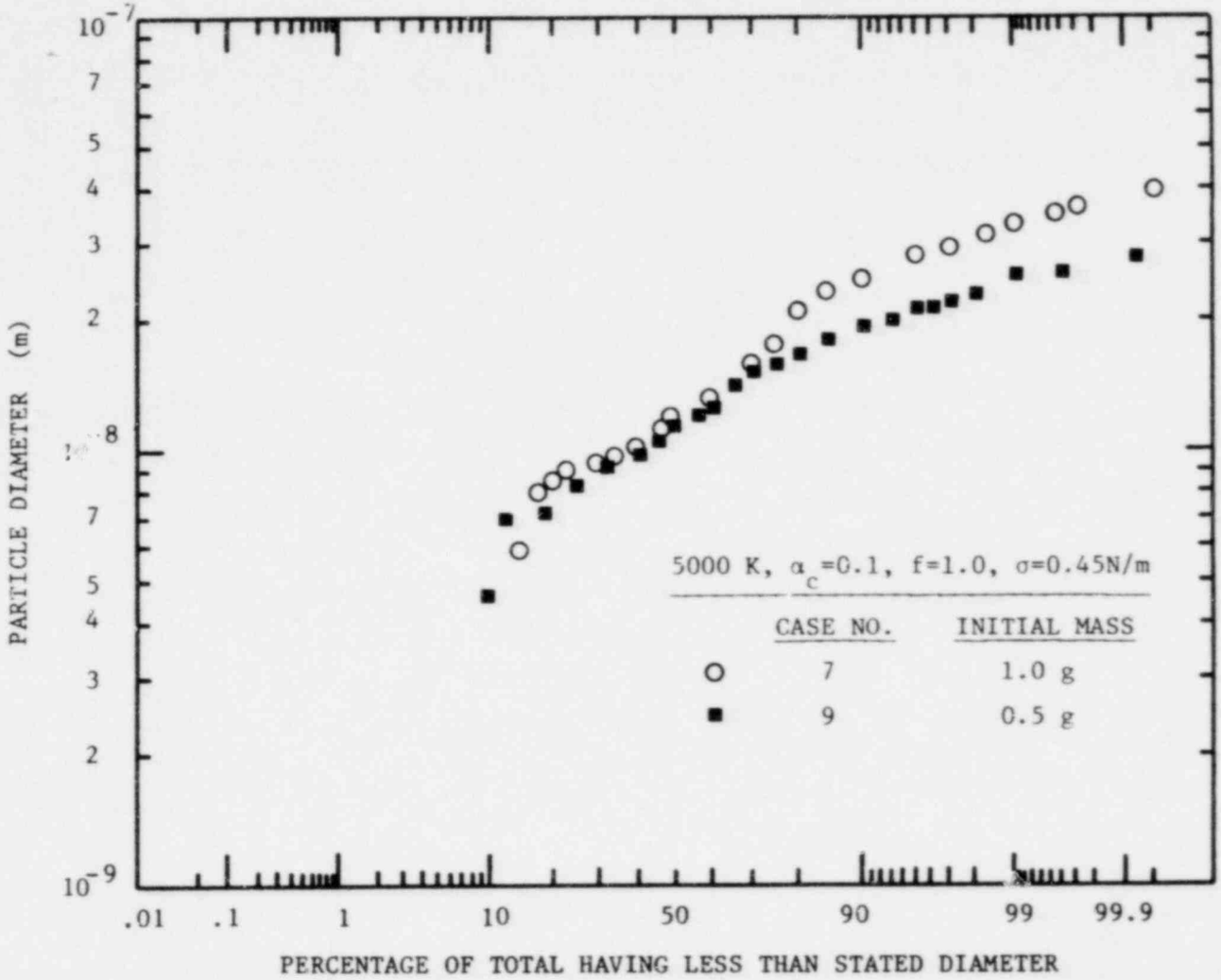

Figure 5.18. Calculated particle-size distribution as a function of initial vapor mass.

There is some indication in the measured results that tests with higher vapor yield generally have higher geometric mean diameter as shown in Table 5.2. There are some small differences between the tests which might be caused, however, by uncertainties other than vapor mass yield.

Argon Pressure

A few CDV tests have been run at ORNL with the argon at 2.02 MPa (20 atmospheres) instead of 0.1 MPa. Therefore, a calculation was made with the surrounding argon at 300 K and 2.02 MPa, although the calculation was only partially completed.

Condensation phenomena in this case are somewhat different from the cases discussed earlier. In this case the vapor pressure is only twice as much as that of the surrounding argon. Thus the expansion rate of the vapor is much smaller than that of the cases discussed earlier. A comparison of the calculated UO_2 vapor-argon interface trajectory is shown in Fig. 5.19. Expansion of the vapor sphere actually observed in the CDV tests was much slower with argon pressure at 2.02 MPa which is qualitatively in agreement with the calculation. (The actual experimental expansion rate at 2.02 MPa has not yet been measured).

The calculation indicates that the increase in supersaturation during this very slow expansion is insufficient to cause the onset of homogeneous nucleation as the rarefaction fan moves initially through the vapor. The vapor reflected rarefaction wave is needed before the degree of supersaturation is raised to the extent required to cause homogeneous nucleation. Thus, unlike the cases at 0.1 MPa argon pressure, in the 2.02 MPa

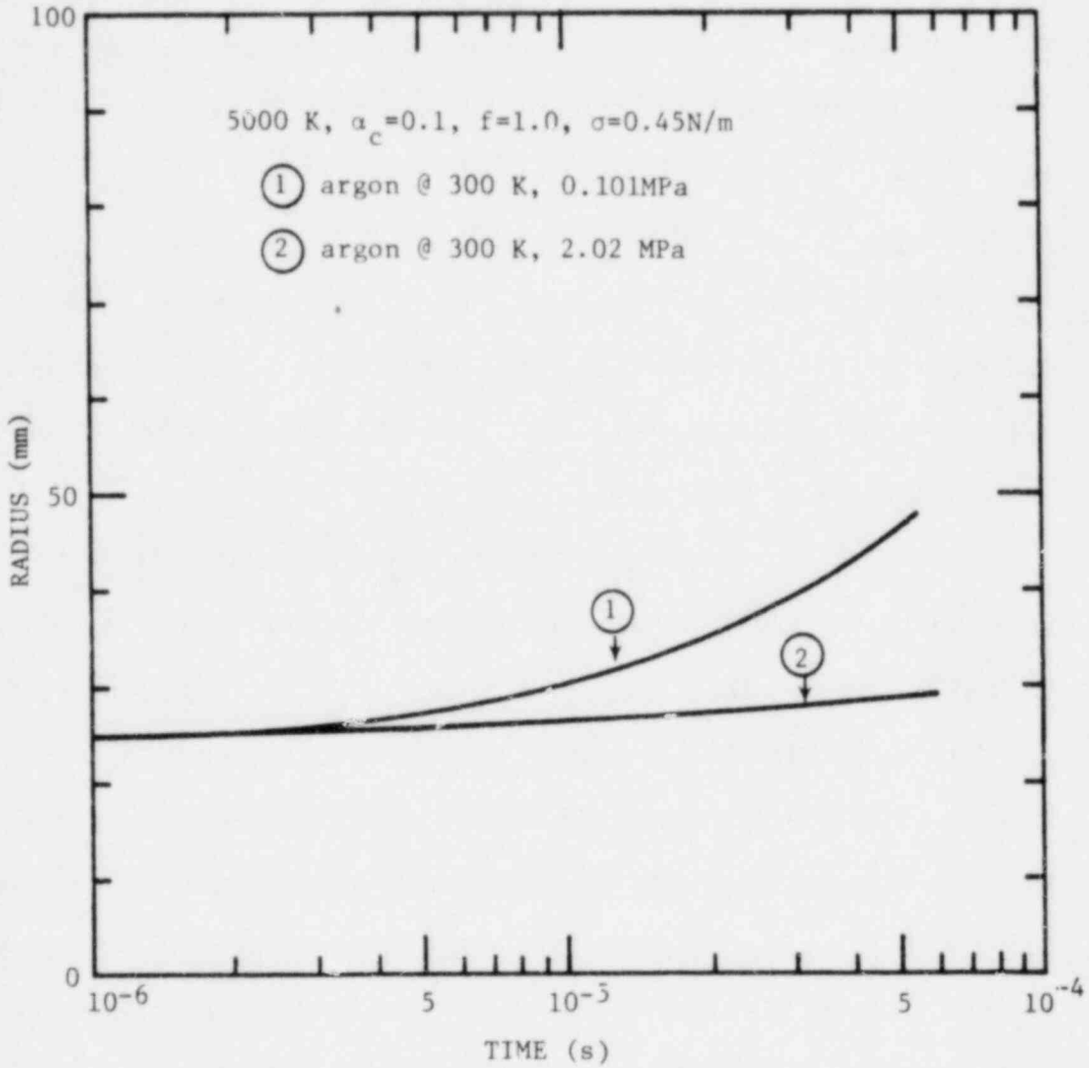

Figure 5.19. The trajectory of the UO_2-argon interface as a function of initial argon pressure.

case the homogeneous nucleation starts at the zone next to the left-hand boundary instead of starting at the zone next to the interface. The supersaturation ratios in this case are very low relative to the previous cases. The number of particles nucleated in this case is low and the particle sizes are large. Thus the geometric mean diameter of the final particle-size distribution for this case should be large relative to the previous cases. Figures 5.20 shows the particle-size distribution for this case at an early time in the calculation and indicates the generally large particle sizes. (Note that the diameter scale is a factor of 10 higher in Fig. 5.20 than in the previous cases). The calculation was terminated at this time due to the large amount of computing time which would have been required to complete it.

5.6 Conclusions

Several conclusions were drawn from the comparison of the analytical results with the experimental data.

The agreement between the rate of expansion of the UO_2 vapor-argon interface, as shown in Fig. 5.8, indicates that the governing gas dynamics phenomena in the CDV tests are interpreted correctly.

The calculated particle-size distribution agrees with the measured particle-size distribution except at the large size particle tail, as in Fig. 5.9. This agreement indicates that the small primary particles from the CDV tests resulted from homogeneous nucleation and condensation growth, as assumed in the analytical model. The deviation at the large particle end of the particle-size distribution prevents the conclusion that all particles resulted from condensation; some of the larger particles might resulted from fragmentation.

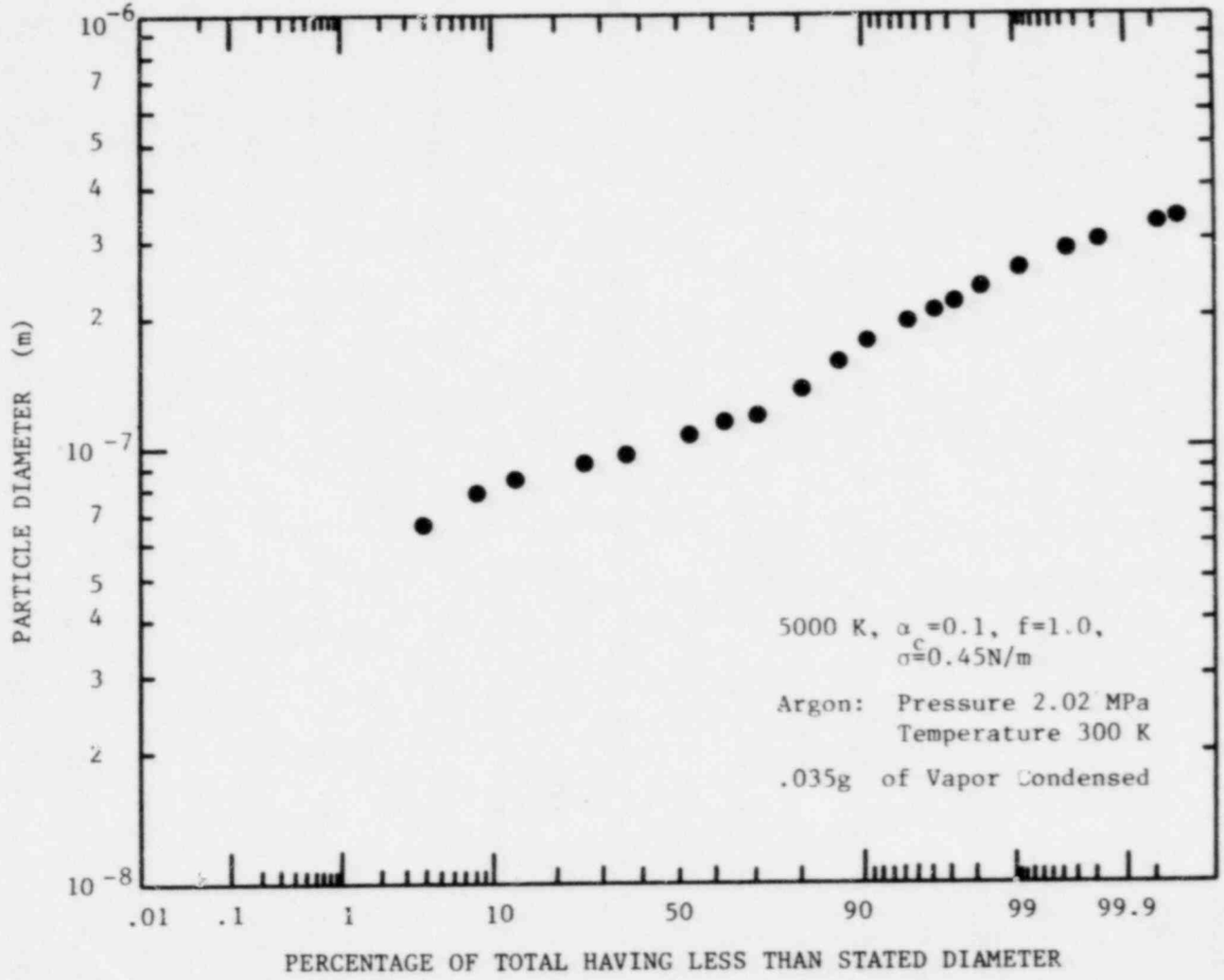

Figure 5.20. Calculated particle-size distribution with initial argon pressure at 2.02 MPa. (Note factor of 10 increase in particle diameter scale relative to other figures.)

The deviation between experiments and theory at the upper end of the particle-size distribution could result from deficiencies in the modeling of the gas dynamics or it could indicate that some of the larger particles are caused by fragmentation of the liquid UO_2 instead of condensation.

REFERENCES

1. Wright, A.L., N.W. Bertini, T.S. Kress, M.L. Tobias, M.J. Kelly, L.F. Parsly, J.S. White. Effect of Energy Density on Aerosol Yield and Primary Particle Sizes Produced by the Capacitor Discharge Vaporizations (CDV) of UO_2, NUREG/CR-0120(ORNL/NUREG/TM-163), Oak Ridge National Laboratory (October 1978).*

2. Kennedy, M.F., C.A. Erdman, P.L. Garner, A.B. Reynolds, and A.E. Waltar. "A First-Generation Model to Predict Particle-Size Distributions for Condensed UO_2 Vapor." Trans. Am. Nucl. Soc., Vol. 26 (June 1977), p. 339.

3. Kennedy, M.F., C.A. Erdman, and A.B. Reynolds. Primary Aerosol Particle-Size Distribution from Homogeneous Nucleation Condensation and Particle Growth, NUREG-0391 (UVA/529106/NEEP 77/102). University of Virginia (December 1977).*

4. Kennedy, M.F. Primary Aerosol Particle-Size Distribution from Homogeneous Nucleation Condensation and Particle Growth, Ph.D. Dissertation, University of Virginia (May 1978).

5. Kelly, M.J., et.al. Development of a Capacitor Discharge Vaporization (CDV) Technique to Produce Aerosols Fromed under HCDA Postulated Condition, ORNL/NUREG/TM-160, NUREG/CR-0226, June 1978.*

6. Chace, William G. and Howard K. Moore. Exploding Wires, Vol. 1, Plenum Press, Inc., New York, 1959.

7. Chace, William G. and Howard K. Moore. Exploding Wires, Vol. 2, Plenum Press, Inc., New York, (1961).

8. Chace, William G. and Howard K. Moore. Exploding Wires, Vol. 3, Plenum Press, Inc., New York (1964).

9. Chace, William G. and Howard K. Moore. Exploding Wires, Vol. 4, Plenum Press, Inc., New York (1968).

10. Bennett, F.D. "Cylindrical Shock Waves from Exploding Wires, The Physics of Fluid, Vol. 1, No. 4, 347 (July-August 1958).

11. Lin, Shas-Chi. "Cylindrical Shock Waves Produced by Instantaneous Energy Release," J. of Applied Physics, Vol. 25, No. 1 (January 1954).

12. Wegener, P.P. "Gasdynamics of Expansion Flows with Condensation, and Homogeneous Nucleation of Water Vapor," Chapter 4 of Non-equilibrium Flows Part I edited by Peter P. Wegener, Marcel Dekker, New York and London (1969).

13. Wegener, P.P. "Nonequilibrium Flow with Condensation," Acta Mechanica, 21, 65-91, (1975).

14. Wegener, P.P., B.J.C. Wu. "Gasdynamics and Homogeneous Nucleation," Chapter 7 of Nucleation Phenomena edited by A.C. Zettlemover, Elseriver Scientific Publishing Company (1977).

15. Wegener, P.P., G. Ludguist. "Condensation of Water Vapor in the Shock Tube Below 150 K," J. of Applied Physics, Vol. 22, No. 2 February 1951).

16. Glass, I.I., G.N. Patterson. "A Theoretical and Experimental Study of Shock-Tube Flows," J. of the Aeronautical Sciences, Vol. 22, No. 2 (February 1955).

17. Kawada, Harno, Yasuo Mari. "A Shock Tube Study on Condensation Kinetics," Bulletin of the JSME, Vol. 16, No. 97 (July 1973).

18. Barschdorff, D. "Carrier Gas Effects on Homogeneous Nucleation on Water Vapor in a Shock Tube," The Physics of Fluids, Vol. 18, No. 5 (May 1975).

19. Kalra, S.P. Experiments on Nonequilibrium, Nonstationary Expansion of Water Vapor/Carrier Gas Mixtures in a Shock Tube, Institute for Aerospace Studies, U. of Toronto, Toronto, Canada, UTIAS Rept. No. 195 (April 1975).

20. Sislian, J.P. Condensation of Water Vapor with or without a Carrier Gas in a Shock Tube, Institute of Aerospace Studies, U. of Toronto, Toronto, Candad, UTIAS Rept. No. 201 (November 1975).

21. K. Chen, "UO_2 Vapor Condensation by Rarefaction Waves in the ORNL Capacitor Discharge Vaporization Tests," Ph.D. Dissertation, University of Virginia (January 1981).

22. K. Chen and A.B. Reynolds, "Particle Size Distribution from Condensation in ORNL CDV Tests in Argon," NUREG report, to be issued.

23. Lawrence, R.J., D.S. Mason. WONDY IV: A Computer Program for 1-D Wave Propagation with Rezoning, SC-RR-710284, Sandia Laboratories, Albuquerque (August 1971).

24. VonNeumann, J.R. R.D. Richtmyer. "A Method for the Numerical Calculation of Hydrodynamic Shocks," J. of Applied Phys., Vol. 21 (March 1950).

25. Abraham, F.F. Homogeneous Nucleation Theory, Academic Press, New York (1974).

26. Hill, P.G., H. Witting, and E.P. Demetri. "Condensation of Metal Vapors During Rapid Expansion," J. Heat Transfer, 85, 303-314 (1963).

27. Kang, S.W. "Analysis of Condensation Droplet Growth in Rarefied and Continuum Environments," AIAA J., 5, No. 7, 1288-1295 (1967).

28. Guggenheim, E.A. Thermodynamics, North-Holland Publishing Co., (1967).

*Available for purchase from the National Technical Information Service, Springfield, VA 22161.

NRC FORM 335 (7.77)

U.S. NUCLEAR REGULATORY COMMISSION

BIBLIOGRAPHIC DATA SHEET

1. REPORT NUMBER (Assigned by DDC)
NUREG/CR-2111

4. TITLE AND SUBTITLE (Add Volume No., if appropriate)
Bubble Behavior in LMFBR Core Disruptive Accidents

2. (Leave blank)

3. RECIPIENT'S ACCESSION NO.

7. AUTHOR(S) A. B. Reynolds, C. A. Erdman, R. C. Anderson, D. R. Bradley, K. Chen, M. R. Gold, R. R. Humphris, M. Pilch

5. DATE REPORT COMPLETED
MONTH: December YEAR: 1980

9. PERFORMING ORGANIZATION NAME AND MAILING ADDRESS (Include Zip Code)
Department of Nuclear Engineering and Engineering Physics
University of Virginia
Charlottesville, VA 22901

DATE REPORT ISSUED
MONTH: July YEAR: 1981

6. (Leave blank)

8. (Leave blank)

12. SPONSORING ORGANIZATION NAME AND MAILING ADDRESS (Include Zip Code)
U. S. Nuclear Regulatory Commission
Division of Accident Evaluation
Office of Nuclear Regulatory Research
Washington, DC 20555

10. PROJECT/TASK/WORK UNIT NO.

11. CONTRACT NO.
FIN B5616

13. TYPE OF REPORT

PERIOD COVERED (Inclusive dates)
October 1979 - September 1980

15. SUPPLEMENTARY NOTES

14. (Leave blank)

16. ABSTRACT (200 words or less)

Research is part of the Aerosol Release and Transport Program. Four principal areas were investigated: (1) bubble dynamics and heat transfer, (2) measurement of particle sizes and flashing (3) acceleration-induced fragmentation of liquid drops, and (4) particle-size distributions from condensation. In the first area, the UVABUBL computer model for the analysis of bubble expansion in ORNL FAST tests is described. In the second, development of an experiment to flash high temperature water and measure droplet sizes from flashing is described. In the third area, results of an extensive literature analysis of acceleration-induced fragmentation of liquid drops, together with model improvements over the entire range from bag to catastrophic breakup, are summarized. In the last area, computer analysis of the measured particle-size distributions from ORNL CDV tests in argon indicates that the particles were formed by homogeneous nucleation and condensation growth.

17. KEY WORDS AND DOCUMENT ANALYSIS

17a. DESCRIPTORS

17b. IDENTIFIERS/OPEN-ENDED TERMS

18. AVAILABILITY STATEMENT
Unlimited

19. SECURITY CLASS (This report)
Unclassified

21. NO. OF PAGES

20. SECURITY CLASS (This page)
Unclassified

22. PRICE
$

NRC FORM 335 (7.77)

* U.S. GOVERNMENT PRINTING OFFICE: 1981—341-742:1171